2015

Developing Recognition Criteria for Current-Wave-Enhanced Sediment Gravity Flows

Kathryn Christine Denommee
Louisiana State University and Agricultural and Mechanical College

DEVELOPING RECOGNITION CRITERIA FOR CURRENT-WAVE-ENHANCED SEDIMENT GRAVITY FLOWS

A Dissertation

Submitted to the Graduate Faculty of the
Louisiana State University and
Agricultural and Mechanical College
in partial fulfilment of the
requirements for the degree of
Doctor of Philosophy

in

The Department of Geology and Geophysics

by
Kathryn Christine Denommee
B.Sc., University of Waterloo, 2008
M.Sc., Memorial University of Newfoundland, 2011
December 2015

ACKNOWLEDGEMENTS

The completion of this dissertation would not have been possible without the help of many people. Firstly I would like to thank my major advisor, Dr. Samuel Bentley, for his support and guidance throughout my PhD program. I am grateful to Dr. Peter Clift for serving on my supervisory committee. I would also like to thank Dr. Joe Macquaker for not only serving on my supervisory committee, but for his mentorship and constant support; as well as Anna and Duncan Macquaker for always welcoming me into their home.

I am grateful to the many people who contributed to my field and laboratory programs. The LSU Coastal Studies Field Support Unit, Nicolas Decker, Matthew Smith, Laura Sorey, Dr. Jillian Maloney, and Jeff Obelcz provided assistance with sample collection on the SW Louisiana inner shelf. Dario Harazim, Stefanie Lode, and Babatunde Olanipekun collected the materials presented in Chapter 4. Melissa Ausburn and Brandon Thibodeaux are thanked for their assistance with radioisotope sample preparation. I am sincerely grateful to Rick Young and Wanda Leblanc for all the help they have given me throughout my PhD program. I would also like to thank Joe Kington for his assistance with Matlab® and Angelina Freeman for her help with SonarWiz®.

This project was sponsored in part by student research grants from the American Association of Petroleum Geologists, the Geological Society of America, the Society for Sedimentary Geology, and the Gulf Coast Association of Geological Societies, as well as by funds provided through the Billy and Anne Harrison endowment to Dr. Sam Bentley.

I will be forever indebted to my mom, my Aunt Nicole and Uncle Mike who have always supported and encouraged me. Above all I am deeply grateful to my husband Dario, who has not only supported and encouraged me but who fearlessly scaled the cliffs at Ochre Cove for this dissertation.

PREFACE

This dissertation is presented in manuscript format; chapters 2, 3, and 4 are intended for submission and publication in peer-reviewed academic journals. Each of these chapters, while contributing to our understanding of both the processes responsible for transporting sediments across subaqueous clinothems and their resulting sedimentary products, is its own separate element. Chapter 1 provides an overview of the motivation for this dissertation project and Chapter 5 synthesises the results of the three independent studies.

TABLE OF CONTENTS

LIST OF TABLES

LIST OF FIGURES

ABSTRACT

Sedimentary fabrics preserved in the rock record provide some of the best evidence for interpreting paleo-depositional conditions. Muddy sediments in particular are important paleoenvironmental archives, preserving the most complete stratigraphic record of any rock type in basinal settings. However, the full range of mechanisms responsible for the deposition of muddy sediments, particularly in high-energy settings, remains poorly understood. Although frequently observed in modern settings, muddy prodeltaic deposits are rarely identified in the rock record, in part because no catalogue of easily distinguishable recognition criteria exists for this class of mudstones. In order to help overcome this deficiency, this dissertation project employs a combination of oceanographic techniques including shallow seismic surveying, radioisotope geochemistry, sedimentary fabric analyses, and a rock record study to investigate (1) the mechanisms of sediment dispersal and accumulation on the muddy Southwest Louisiana (SWLA) Chenier Plain shelf, where current-wave-enhanced sediment gravity flows (CWESGFs) are understood to play a key role in progradation; (2) the characteristics of the muddy sedimentary fabrics deposited in response to site-specific hydrodynamic conditions on the SWLA shelf; and (3) how muddy sedimentary fabrics deposited in a shallow shelf environment are preserved in the rock record, and how post-depositional changes (e.g., bioturbation, compaction, and diagenesis) alter these fabrics by examining the Ordovician Power Steps Formation, Bell Island, Newfoundland.

The results of these investigations show that (1) CWESGFs are effective mechanisms for the offshore transport of muds on the SWLA Chenier Plain shelf. In addition to simply transporting sediment, CWESGFs contribute to the development of unstable seabed conditions where mass-failures can develop, even on extremely low gradients. (2) CWESGF microstratigraphy reflects the site-specific flow development in response to the combined

effects of waves, wave period, currents, and gravity and thusly these sediments can be studied in terms of a semi-quantitative framework. (3) The Lower Ordovician Power Steps formation contains sedimentary structures that record evidence of storm-driven muddy transport in a high-energy prodeltaic setting. The high-energy setting likely inhibited bioturbation, while an abundance of highly reactive mafic minerals sourced from a Paleozoic hinterland led to early cementation that inhibited compaction, preserving diagnostic sedimentary fabrics.

CHAPTER 1: INTRODUCTION

1.1 Motivation for Dissertation Research

Fine-grained sedimentary rocks account for the majority of the sedimentary rock types at the Earth's surface (Aplin and Macquaker, 2011). Scientifically these rocks are important not only because of their ubiquity, but because they preserve the most complete stratigraphic record of any facies type observed in basinal settings (Aplin and Macquaker, 2011). Economically, fine-grained successions are important because they host ore mineral deposits, act as source and seal rocks for conventional hydrocarbon plays, and act as reservoir rocks for unconventional hydrocarbon plays. In the past it was commonly assumed that for the most part, extensive muddy successions were deposited either (1) in low-gradient, quiescent settings as fine-grained material settled out of buoyant plumes which extended out into the deep basin, depositing units with basin-scale draping geometries; (2) in the distal reaches of the shelf as the depositional products of large storms, depositing distal temptestites; or (3) through traditional auto-suspending gravity flows operating on relatively steep slopes, depositing turbidites (Macquaker et al., 2010). Such beliefs led to the development of models that assumed that muddy deposition (especially that which is associated with point source fluvial input) was associated mainly with deep, low energy environments (Plint et al., 2012).

Recently, work on both ancient and modern mud-dominated systems has shown that this paradigm is too simplistic (e.g., Rotondo and Bentley, 2003; Bhattacharya and MacEachern, 2009; Plint et al., 2014; and Harazim and McIlroy, 2015). In both modern and ancient shelf settings, mud-dominated successions frequently contain complex stratigraphic geometries of which, low-gradient clinoforms feature prominently (e.g., Friedrichs and Wright, 2004; Walsh et al., 2004; Slingerland et al., 2008; Jaramillo et al., 2009; and Laycock et al., 2011) and contain

units with significant evidence of sediment reworking, and advective dispersal. In fact, muddy clinoforms have been estimated to comprise at least one third of all modern and ancient shelf deposits (Plint et al., 2009). Despite their ubiquity and obvious importance, the full range of mechanisms responsible for mud accumulation and dispersal in such settings are not well understood.

Studies of ancient sedimentary successions (e.g., Plint et al., 2009) in which fine-grained sediments are commonly observed in transects extending away from fluvial point sources, suggest that hydrodynamic processes capable of transporting fine-grained material "across shelves in very low-gradient settings" must exist (Bentley et al., 2012). These observations however, could not be reconciled with traditional physical oceanographic observations wherein it is recognized that currents alone are not capable of transporting large volumes of material across-shelf in low-gradient settings because "regional seabed gradients are too low to facilitate transport by conventional gravity-driven processes" (Bentley et al., 2012). In 1990, Wright et al. described for the first time the existence of isobath-parallel fluid-mud layers (hyperpycnal flows) near the mouth of the Yellow River. It was concluded that these layers were maintained not as the result of the hyperpycnal river effluent entering the shelf (a purely gravity-driven sediment transport process), but rather by bottom boundary layer shear stresses produced by strong shore-parallel tidal currents (Wright et al., 2001). This revelation was important because it provided for the first time a mechanism for gravity-driven sediment transport that could produce the across-shelf sediment movement frequently observed in the rock record (e.g., Plint et al., 2009) which had until this time, yet to be reconciled with modern observations of fine-grained sediment transport processes operating on low-gradient shelves.

This was the beginning of a fundamental paradigm shift in terms of our understanding of the hydrodynamic processes operating on low-gradient shelf settings. Specifically, the discovery that even on low-gradient shelves where it was thought that the gradient was too low to initiate gravity-induced turbulence, that gravity-driven transport can rapidly move suspended sediment if current and wave-current energies are also present (Wright et al., 2001). Flows that operate under such conditions have been coined as "wave-current-sediment-enhanced gravity flows", or CWESGFs. These flows require the additional energies of near-bed currents and/or the orbital motion of surface-gravity waves in addition to the gravity-induced turbulence component (Figure 1.1) to maintain sediment (fluid mud) in suspension (Parsons et al., 2009); allowing them to operate at gradients as low as 5m/km, well below the 12m/km gradient required in the case of autosuspending turbidity currents (Friedrichs and Wright, 2004).

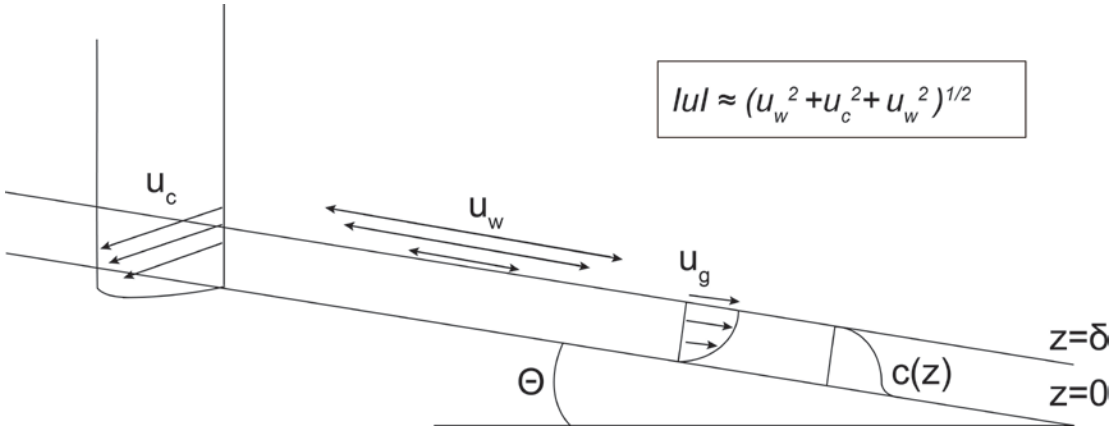

Figure 1.1 Schematic diagram of a CWESGF within a wave boundary layer of thickness δ, moving across a shelf with slope θ. |u| is the velocity scale which accounts for the contribution to quadratic friction of wave orbital velocity (u_w), current velocity (u_c), and the speed of the gravity current (u_g). Modified from Friedrichs and Scully (2007) and Macquaker et al. (2010).

Due to the difficulties associated with sampling and imaging fluxes of sediment so close to the bed, it was not until the initiation of multi-investigator studies such as the STRATAFORM projects and the S2S MARGINS project that real progress was made towards understanding how

CWESGFs operate on continental shelves (Parsons et al., 2009). Further to simply developing a better understanding of the hydrodynamics of CWESGFs, observations stemming from these large studies demonstrated that not only can CWESGFs operate in low-gradient settings, but that they actually play a key role in transporting large volumes of mud across-shelf in association with high-yield rivers (Friedrichs and Scully, 2007), and in shaping the overall morphology of the shelf clinoform over which they operate (Wright and Friedrichs, 2006). The subaqueous clinoform off the Southwest Louisiana coast which is the focus of much of this dissertation (Jaramillo et al., 2009) is a prime example of this phenomenon.

Finally, the recognition of these processes led researchers to then consider that these types of flows must also have operated in the rock record (Bhattacharya and MacEachern, 2009; Macquaker et al., 2010). The stratigraphic signatures of muddy clinoforms however, can be difficult to recognize in the rock record owing to the subtleties of their shallow gradients (Laycock et al., 2011) and the absence of any well-defined stratigraphic recognition criteria. In order to develop such criteria it will be necessary to not only understand how and where CWESGF deposits form, but how the hydrodynamics and unique bottom boundary layer conditions under which they form control the resultant sedimentary fabric. In and of itself this is a difficult question to answer, and it is made more so by our limited ability to observe conditions below the lutocline, where sediments are deposited.

It is the aim of this dissertation to help develop a greater understanding of the dispersal, accumulation and deposition of muddy sediments in high-energy, low-gradient settings, contributing to the development of criteria to aid in their recognition in ancient settings. This will help to close the gap between our understanding of modern processes and the ancient mudstone record. Not only is having a better understanding of how fine-grained sediments are

deposited and incorporated into the rock record of scientific interest, but it is of significant economic value as it will lead to a better understanding of mudstone facies variability, which will in turn enhance our ability to better develop the resources hosted within these deposits. This will be accomplished by (1) examining the mechanisms of progradation on the Southwest Louisiana Chenier Plain inner shelf, a modern low-gradient muddy clinothem system; (2) examining the sedimentary fabrics produced by CWESGFs in this setting in the context of their formative hydrodynamics; (3) developing a semi-quantitative framework by which diagnostic CWESGF fabrics can be studied in the context of their site-specific formative hydrodynamics; (4) apply learnings from modern muddy clinothem systems to the rock record.

1.2 References

Aplin, A. C., and Macquaker, J. H. S., 2011, Mudstone diversity: Origin and implications for source, seal, and reservoir properties in petroleum systems: AAPG Bulletin, v. 95, no. 12, p. 2031-2059.

Bentley, S. J., Friedrichs, C. T., and Walsh, J. P., 2012, Collaborative Research: What do They Look Like and How do They Form? Sedimentary Products of Wave-Enhanced Sediment-Gravity Flows on Continental Shelves, NSF.

Bhattacharya, J. P., and MacEachern, J. A., 2009, Hyperpycnal Rivers and Prodeltaic Shelves in the Cretaceous Seaway of North America: Journal of Sedimentary Research, v. 79, no. 3-4, p. 184-209.

Friedrichs, C. T., and Scully, M. E., 2007, Modeling deposition by wave-supported gravity flows on the Po River prodelta: From seasonal floods to prograding clinoforms: Continental Shelf Research, v. 27, no. 3-4, p. 322-337.

Friedrichs, C. T., and Wright, L. D., 2004, Gravity-driven sediment transport on the continental shelfimplications for equilibrium profiles near river mouths: Coastal Engineering, v. 51, no. 8-9, p. 795-811.

Harazim, D., and McIlroy, D., 2015, Mud-Rich Density-Driven Flows Along an Early Ordovician Storm-Dominated Shoreline: Implications for Shallow-Marine Facies Models: Journal of Sedimentary Research, v. 85, no. 5, p. 509-528.

Jaramillo, S., Sheremet, A., Allison, M. A., Reed, A. H., and Holland, K. T., 2009, Wave-mud interactions over the muddy Atchafalaya subaqueous clinoform, Louisiana, United States: Wave-supported sediment transport: Journal of Geophysical Research: Oceans, v. 114, no. C4, p. C04002.

Laycock, D. P., Pedersen, P. K., Spencer, R., Larter, S., Huang, H., and Aplin, A. C., 2011, 3-D Architecture of Muddy Clinoforms: Control on the Distribution and Lateral Variation of Sedimentary and Reservoir Facies, Upper Cretaceous, Eastern Alberta, AAPG Annual Conference and Exhibition: Houston, Texas.

Macquaker, J. H. S., Bentley, S. J., Bohacs, K. M., Lazar, R., and Jonk, R., 2010, Advective Sediment Transport on Mud-Dominated Continental Shelves: Processes and Products, AAPG Anual Convention and Exhibition: New Orleans, LA.

Parsons, J. D., Friedrichs, C. T., Traykovski, P. A., Mohrig, D., Imran, J., Syvitski, J. P. M., Parker, G., Puig, P., Buttles, J. L., and García, M. H., 2009, The Mechanics of Marine Sediment Gravity Flows, Continental Margin Sedimentation, Blackwell Publishing Ltd., p. 275-337.

Plint, A. G., 2014, Mud dispersal across a Cretaceous prodelta: Storm-generated, wave-enhanced sediment gravity flows inferred from mudstone microtexture and microfacies: Sedimentology, v. 61, no. 3, p. 609-647.

Plint, A. G., Macquaker, J. H. S., and Varban, B. L., 2012, Bedload Transport of Mud Across A Wide, Storm-Influenced Ramp: Cenomanian–Turonian Kaskapau Formation, Western Canada Foreland Basin: Journal of Sedimentary Research, v. 82, no. 11, p. 801-822.

Rotondo, K., and Bentley, S. J., 2003, Deposition and Resuspension of Fluid Mud on the Western Louisiana Inner Shelf: Gulf Coast Association of Geological Societies Transactions, v. 53, p. 722-731.

Slingerland, R., Driscoll, N. W., Milliman, J. D., Miller, S. R., and Johnstone, E. A., 2008, Anatomy and growth of a Holocene clinothem in the Gulf of Papua: Journal of Geophysical Research: Earth Surface, v. 113, no. F1.

Walsh, J. P., Nittrouer, C. A., Palinkas, C. M., Ogston, A. S., Sternberg, R. W., and Brunskill, G. J., 2004, Clinoform mechanics in the Gulf of Papua, New Guinea: Continental Shelf Research, v. 24, no. 19, p. 2487-2510.

Wright, L. D., and Friedrichs, C. T., 2006, Gravity-driven sediment transport on continental shelves: A status report: Continental Shelf Research, v. 26, no. 17-18, p. 2092-2107.

Wright, L. D., Friedrichs, C. T., Kim, S. C., and Scully, M. E., 2001, Effects of ambient currents and waves on gravity-driven sediment transport on continental shelves: Marine Geology, v. 175, no. 1–4, p. 25-45.

CHAPTER 2: ACROSS-SHELF CLINOTHEM DYNAMICS ON THE SOUTHWEST LOUISIANA CHENIER PLAIN INNER SHELF

2.1 Introduction

Clinothems, strata bounded by clinoform surfaces, comprise the majority of the stratigraphic sequences underlying continental shelves (Palinkas and Nittrouer, 2006). They are the dominant architectural component of most deltaic-to-continental slope successions and as such are important paleo-environmental archives, recording evidence of sea level change, compactional subsidence, sediment supply, and hydrodynamic conditions – information that is essential for accurately interpreting the geologic record. Increasingly, it is being recognized that subaqueous deltas, clinothems deposited subaqueously on muddy, high-energy shelves, are relatively common features. This type of delta has been identified on a number of modern shelves with high sediment discharge including the Amazon (e.g., Kuehl et al., 1986), the Fly River (GoP) (Slingerland et al., 2008), and the Ganges-Brahmaputra (Kuehl et al., 1997). Less well-developed subaqueous-deltas have also been observed seaward of smaller rivers which carry a large sediment load such as the Eel (Traykovski et al., 2000), the Po (Palinkas and Nittrouer, 2006) and the Atchafalaya (Allison et al., 2000; Draut et al., 2005b). As is the case for all delta clinothem systems, subaqueous deltas develop their diagnostic morphology in response to the transient nature of the sediment depocenter, which tends to be highly localized in both space and time (Wolinsky and Pratson, 2007).

Despite their ubiquity and their importance as paleo-environmental archives, the full, detailed range of mechanisms responsible for their formation and maintenance are not yet fully understood (e.g., Palinkas and Nittrouer, 2006; Macquaker et al., 2010). The Southwest Louisiana (SWLA) Chenier Plain inner shelf (Figure 2.1) is an ideal setting in which to study the development of modern mud-dominated subaqueous-delta clinothem systems, and as such has been the subject of numerous studies relating to fine-grained sediment transport dynamics

(Allison et al., 2000; Rotondo and Bentley, 2003; Draut et al., 2005a; Draut et al., 2005b; Kineke et al., 2006; Jaramillo et al., 2009; Sheremet et al., 2011; Denommee and Bentley, 2013; Traykovski et al., 2015). This study looks to further elucidate (1) the sediment transport mechanisms driving clinothem progradation on the SWLA Chenier Plain, and (2) their contributions to building the fine-grained stratigraphic record.

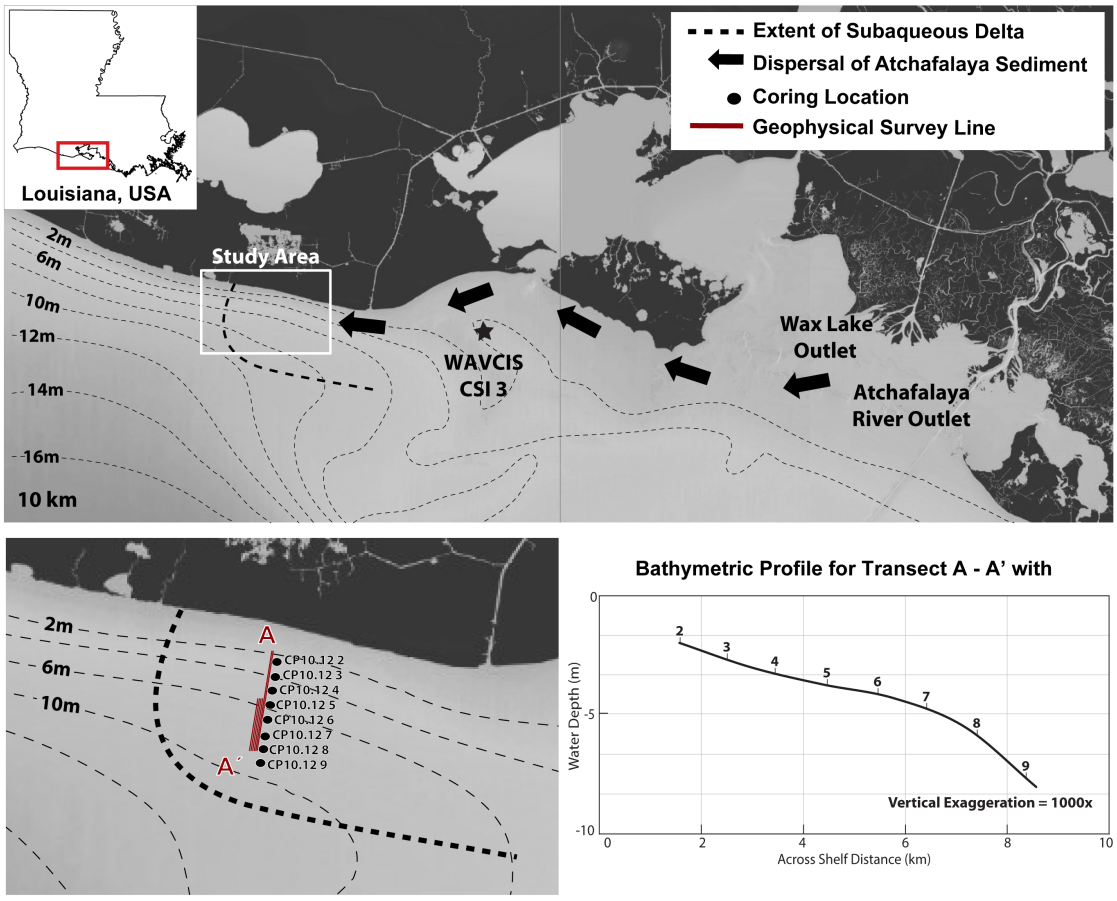

Figure 2.1 Map of the study area indicating coring locations and the location of geophysical survey lines. The approximate extent of the subaqueous delta is illustrated by the dashed line (modified from Draut et al., 2005a). Inset map illustrates the clinoform expression of the shelf and is constructed from bathymetric survey data.

2.2 Background

2.2.1 Subaqueous-Delta Clinothem Sedimentation

Most subaqueous-delta clinothems tend to be shore-parallel, laterally extensive depositional features with near-linear plan view morphologies (Patruno et al., 2015). They also tend to display nearly symmetrical, sigmoidal cross-sectional geometry comprising three

geometric elements: topsets, foresets, and bottomsets. The topset beds slope gently seaward and can exhibit concave-up morphology. Topsets are separated from the more steeply dipping foreset beds by a prominent morphological feature commonly referred to as the rollover point, which is defined as the point of highest curvature on the sigmoid (Pirmez et al., 1998). The location of the rollover is generally thought to be controlled by the lateral distribution of shear stresses within the bottom boundary layer. In an equilibrium system this point represents the water depth at which the clinothem system transitions from being dominated by erosion (landward) and sediment bypass to be dominated by deposition (seaward, i.e., where accommodation is available). Typically, sediment accumulation rates are low on the clinothem topsets, as relatively high shear stresses within the bottom boundary layer can erode the seabed and/or maintain sediment in suspension (Palinkas and Nittrouer, 2006). On the foresets, shear stresses decrease in response to increasing water depth and rapid sedimentation results in the deposition of relatively steeply dipping strata. On the bottomsets, sediment accumulation rates tend to be low as most sediment is trapped on the foresets, and there is limited sediment supplied to this seaward portion of the clinoform (Palinkas and Nittrouer, 2006).

The shape, growth patterns, and facies character of subaqueous-delta clinoforms, like other shallow marine depositional systems, are dominated by basinal processes including: (1) water depth which controls clinoform relief; (2) upstream conditions which control sediment influx and; (3) basin hydrodynamics (e.g., tides and currents) which control sediment efflux (Nittrouer et al., 1986; Karner and Driscoll, 1999). Sediment dispersal on subaqueous-delta clinothems however, is complex and does not occur simply in response to wave or current motion (Pratson et al., 2009).

Most subaqueous delta clinoforms have gradients well below the 12m/km required to support the auto-suspension of sediments in turbid, hyperpycnal flows (Wright and

Friedrichs, 2006). In spite of this, sediment flows driven in part by gravity have commonly been observed transporting large volumes of fine-grained muddy sediment across low-gradient shelves, and are understood to play an important role in controlling clinoform morphology (Sternberg et al., 1996; Traykovski et al., 2000; Wright et al., 2001; Friedrichs and Wright, 2004; Wright and Friedrichs, 2006). This is possible because the energy required to maintain sediment in suspension can be augmented by wave-orbital velocities and near-bed currents in the bottom boundary layer; rather than solely relying on gravity-induced turbulence to support the flow as is the case for a traditional auto-suspending sediment gravity flows (Friedrichs and Wright, 2004; Traykovski et al., 2007). In such cases flows are termed current-wave-enhanced sediment-gravity flows (CWESGFs) (e.g., Macquaker et al., 2010). CWESGFs are composed of fluid mud and maintain sediments in suspension because their high sediment concentrations (>10g/L) of fine particles inhibit particle settling (Kineke et al., 1996). These flows are capable of propagating downslope on gradients as low as 0.5m/km, comparable to the lowest gradients observed on modern continental shelves (Friedrichs and Wright, 2004). As CWESGFs propagate across the shelf under the influence of gravity, they may deposit sediment either in response to (1) a decrease in wave-current energy within the bottom boundary layer or (2) a decrease in bed gradient, or (3) both (Friedrichs and Wright, 2004). CWESGFs have been shown to be the dominant mechanism responsible for sediment transport and progradation on many subaqueous-delta clinothem systems (Wright and Friedrichs, 2006).

In addition to CWESGFs, gravity flows can play an important role in subaqueous-delta clinothem morphodynamics (Kineke and Sternberg, 1995; Walsh and Nittrouer, 2003; Walsh et al., 2004). On low-gradient, muddy clinothems gravity flows have been observed mostly on clinothem foresets, where the increased gradient can compensate for the loss of current and/or wave energies in the bottom boundary layer (Friedrichs and Wright, 2004).

2.2.2 The Southwest Louisiana Chenier Plain Subaqueous Delta

Unlike much of the Louisiana coastline, which is rapidly retreating under the combined influences of anthropogenic activities and the natural subsidence and compaction of deltaic sediments, the SWLA Chenier Plain coast is actively accreting (Allison et al., 2000; Draut et al., 2005a). Fine-grained sediment supply to the SWLA Chenier Plain inner shelf is primarily driven by seasonal flooding of the Mississippi and Atchafalaya rivers which creates a low-salinity, buoyant sediment plume, commonly referred to as the Atchafalaya Mud Stream, that drives coastal accretion in the study area (Wells and Kemp, 1981; Allison et al., 2000; Rotondo and Bentley, 2003; Draut et al., 2005b). Despite being relatively weak (0.1m/s within the 10m isobath), along-shore currents drive the mud plume westward along the coast (Wells and Kemp, 1981) where sediments are ultimately deposited within the vicinity of the study area in the form of an accreting coastal mudflat and a prograding subaqueous-delta clinothem (Draut et al., 2005b).

The study area (Figure 2.1) is a relatively low energy setting, with a mean wave height of 1.5 m and a mean wave period of 4-6 s (Kemp, 1986; Walker and Hammack, 2000; Kineke et al., 2006). Near-bed currents in the study area have been measured at 0.1m/s 1m above the bed (Wright, 1995). Episodically however, the SWLA Chenier Plain is subject to more energetic conditions associated with winter cold fronts that pass at 3-10 day intervals between the months of November and April, and tropical cyclones that are not uncommon from July - October. The intense wave action associated with the passage of cold fronts frequently reworks the seabed, resulting in seabed liquefaction and sediment resuspension. This can lead to the development of fluid muds that can propagate downslope as CWESGFs, transferring sediment seaward (Bentley et al., 2003; Sheremet and Stone, 2003; Jaramillo et al., 2009; Sheremet et al., 2011).

In addition to CWESGFs, shallow seismic surveys have documented evidence of erosion and mass wasting processes transporting sediment offshore in the vicinity of the study area (Bentley et al., 2003). Although this pervious work did not explicitly study the role that mass wasting plays in clinothem progradation in detail, they were able to recognize similarities between seabed mass wasting features (e.g., collapse depressions, bottleneck slides, and mudflow gullies) on the relatively small, very low gradient (<0.02º) SWLA Chenier Plain shelf, and the much larger, more steeply dipping (0.5°) Mississippi River delta front (e.g., Prior and Suhayda, 1979; Coleman et al., 1980).

2.2.3 Aim of Study

It has been well established that CWESGFs play an important role in controlling the morphodynamics of subaqueous-delta clinoforms like the SWLA Chenier Plain (Wright and Friedrichs, 2006). It is unlikely, however, that these flows are the only sediment transport mechanism influencing their morphodynamics and progradation. The purpose of this study is to further elucidate the sediment transport mechanisms driving progradation on the SWLA Chenier Plain subaqueous-delta clinothem by employing a combination of seabed imaging, CHIRP sonar, and shallow seabed investigations.

2.3 Materials and Methods

2.3.1 Seabed Imaging

Compressed high-intensity radar pulse (CHIRP) seismic, high-resolution swath sonar bathymetry, and sidescan sonar data were acquired in July and August of 2012 aboard the RV Coastal Profiler (Figure 2.2). The CHIRP seismic data were collected using a surface-towed, 4-24 kHz EdgeTech SB-424 that penetrated up to ~5 m below the seafloor. Swath sonar

bathymetric data and sidescan sonar data were collected using a hard-mounted EdgeTech 4600 sonar system operating at 540 kHz.

2.3.2 Sediment Core Collection

Sediment cores were collected by deploying an Ocean Instruments MC-400 multicorer from the R/V Coastal Profiler along a 10km-long across-shelf transect (Figure 2.2). Sediment cores collected using a multicorer are relatively short - capable of collecting material from the upper ~60 cm of the seabed. Multicores are most useful for studying the dynamic, shallow portion of the seabed which is subject to resuspension by physical processes. The use of the multicoring technique also assures minimal sample disturbance during collection, preserving the delicate sediment-water interface as well as allowing for the collection of up to four replicate cores per deployment. Due to the high density of oil and gas infrastructure in the vicinity of the study area, the clinothem bottomsets were not sampled.

Sediment cores were subsampled on board the RV Coastal Profiler immediately following collection. For each sampling location one core was subsampled for radioisotope geochronology (^{137}Cs and $^{210}Pb_{XS}$), disaggregated grain size analysis, and water content/porosity at 1 cm intervals for the upper 10cm and at 2cm intervals thereafter. Samples were immediately placed in airtight bags and returned to Louisiana State University for analysis. Two cores per sampling location were subsampled for sedimentary fabric analyses (X-radiography and thin section petrography) using specialized Plexiglas® x-ray trays designed for insertion directly into multicore tubes, minimizing sample disruption. A detailed study of the sedimentary fabrics on the SWLA Chenier Plain shelf is presented separately in Chapter 3 of this dissertation.

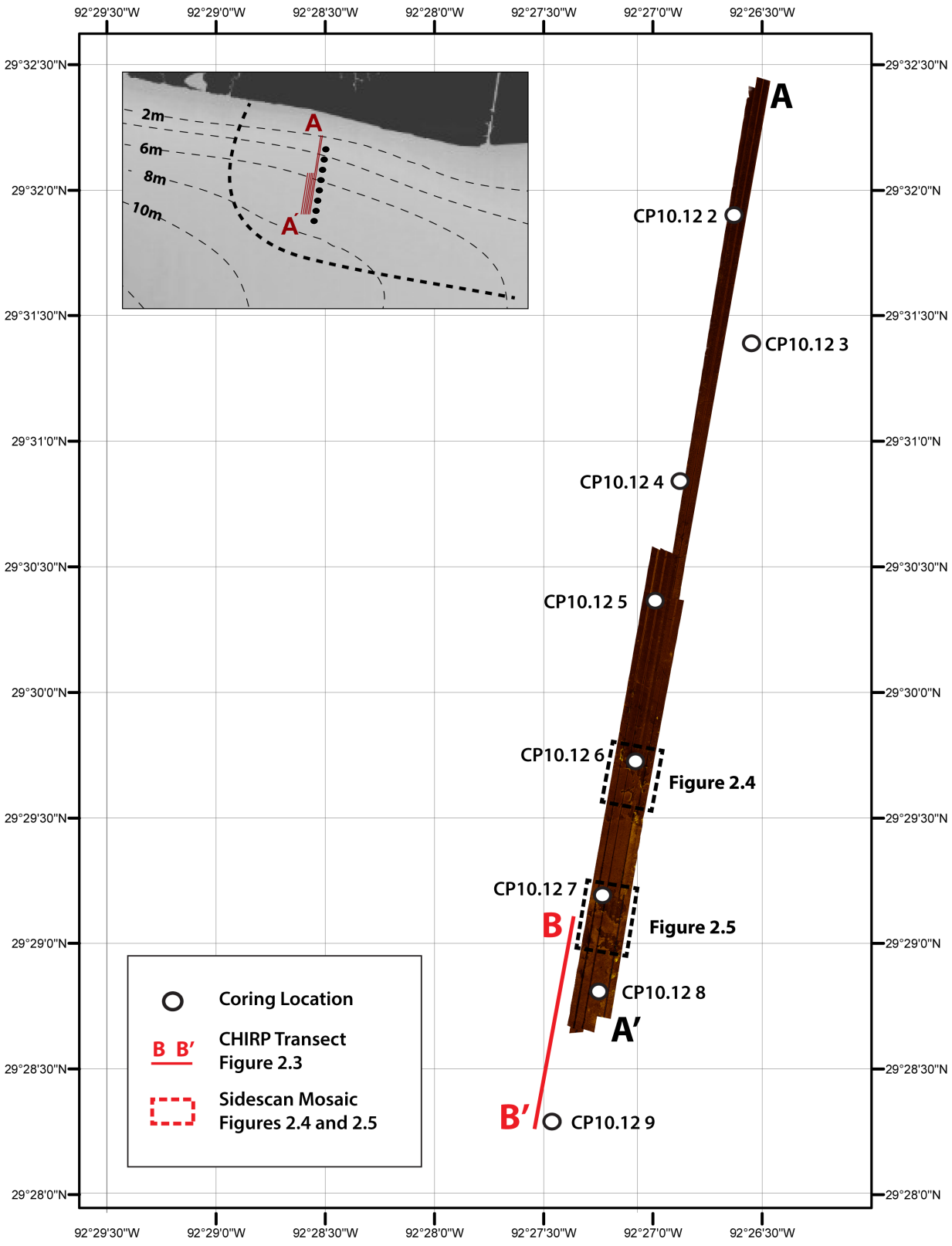

Figure 2.2 Sidescan sonar mosaic indicating the location of CHIRP and high-resolution sidescan sonar mosaics as well as the location of multicores collected from the study area.

2.3.3 Seabed Characterization

Sub-samples taken for sedimentary fabric analysis were imaged using a Kodex LTX-1717 x-ray detector panel illuminated by a Min X-ray HF-80 x-ray generator and evaluated using the image processing program ImageJ (Schneider et al., 2012). The resulting x-ray image negatives reflect variations in bulk density such that light features represent relatively high-density sediments (i.e., quartz), and dark areas represent relatively low bulk density sediments (e.g., clay minerals). This is confirmed by grain-size analyses. Disaggregated grain-size distributions were determined using a Beckman-Coulter LS13 320 laser particle-size analyzer (particle size range of 0.04-2000 μm). Water content (porosity) was determined by change in mass after oven drying for 24h at 60°C.

2.3.4 ^{210}Pb and ^{137}Cs Radioisotope Geochronology

In order to determine sedimentation rates on the clinothem, samples for ^{210}Pb and ^{137}Cs radioisotope geochronology were dried for 24 hours at 60°C, homogenized, and sealed in 50x9 mm petri dishes to allow ingrowth of the ^{210}Pb grandparent ^{222}Rn. Sample for both ^{210}Pb and ^{137}Cs activities were determined by gamma spectrometry by counting for 24 hours on Canberra low-background gamma detectors with activities being reported in decays per minute per gram (1 dpm/g=1/60 Bq). Cesium-137 activity was determined by measurement of the 661keV gamma peak. The minimum detection limit for ^{137}Cs is 0.05 dpm/g. Total ^{210}Pb activity was determined by measurement of the 46.5keV gamma peak. Supported ^{210}Pb activity, ^{210}Pb produced from the decay of ^{226}Ra within the seabed, was determined by measuring the granddaughter radioisotopes of ^{226}Ra: ^{214}PB (295.2 and 352 keV peaks) and ^{214}Bi (609 keV peak) (Cutshall et al., 1983). Excess ^{210}Pb activity was determined by subtracting the total ^{210}Pb activity from supported ^{210}Pb activity. All measurements were corrected for self-absorption following the methods of Cutshall et al. (1983). The minimum

detection limit for ^{210}Pb is 0.1dpm/g which is approximately three times the counting error for supporting activity. When possible, linear sediment accumulation rates were determined from $^{210}Pb_{XS}$ using the following advection-diffusion equation wherein bioturbation is assumed to be negligible and sedimentation is assumed to be steady-state:

$$S = \frac{\lambda z}{ln\left(\frac{Az}{A_0}\right)} \quad (1)$$

where λ is the decay constant ($0.693/t_{1/2}$), z is depth in seabed (cm), A_0 is excess activity at the surface (dpm/g), and A_z is excess activity at depth (dpm/g) (Bentley and Nittrouer, 2003).

2.4 Results

2.4.1 Clinothem Morphology and Seabed Characterization

The across-shelf, bathymetric transect constructed using high-resolution bathymetric data reveals that this portion of the SWLA inner-shelf has a sigmoidal clinoform morphology with recognizable topset, foreset, and bottom set regions (Figure 2.1). Landward of ~4m water depth, roughly corresponding to the location of the clinoform rollover point, the shelf is slightly concave upward; while seaward of this water depth, shelf geometry is convex upwards. On the clinothem topsets strata dip gently seaward with a gradient ranging from ~0.001° - 0.002° (Figure 2.1). An undulating acoustically transparent layer of fluidized mud up to 0.5 m in thickness dominates the stratigraphy, below which acoustic turbidity masks the stratigraphy (Figure 2.3).

Seabed instability and mass movement features are visible on the topsets in both CHIRP and sidescan sonar imaging. Small collapse depressions are apparent beginning at depths as shallow as ~2 to 3m water depth, at a distance of ~3 km offshore (Figures 2.2). These features are commonly observed in association with acoustic turbidity within the

seabed (Figure 2.3). Further offshore beginning in water depths of ~4 m, small bottleneck slides and mudflow gullies become apparent (Figure 2.2). These gradually increase in both size and relief as water depth increases. Collapse depressions present as predominantly rounded to elongate features with diameters ranging from ~20 m to more than 75 m (Figure 2.4). These depressions are bounded by near-circular scarps and relief ranging from 0.25 to > 1 m and are commonly observed as being filled with acoustically transparent (fluidized) muds. Bottle neck slides present as elongate features which have similar morphologies to the collapse depressions however, they have narrow openings at the downslope margin of the failure through which sediment is discharged over the surrounding seabed.

As the seafloor gradient increases, bottle neck slides become larger and more common and mudflow gullies, major elongate mass failure features with morphologies reminiscent of subaerial mud- or debris-flows (Coleman et al., 1993), become prominent features on the seabed (Figure 2.5). In CHIRP seismic, mudflow gullies have display nearly uniform floors with acoustically transparent fill (Figure 2.3). There is generally low surface relief and a lack of well-developed discrete depositional lobes at the downslope ends of these features.

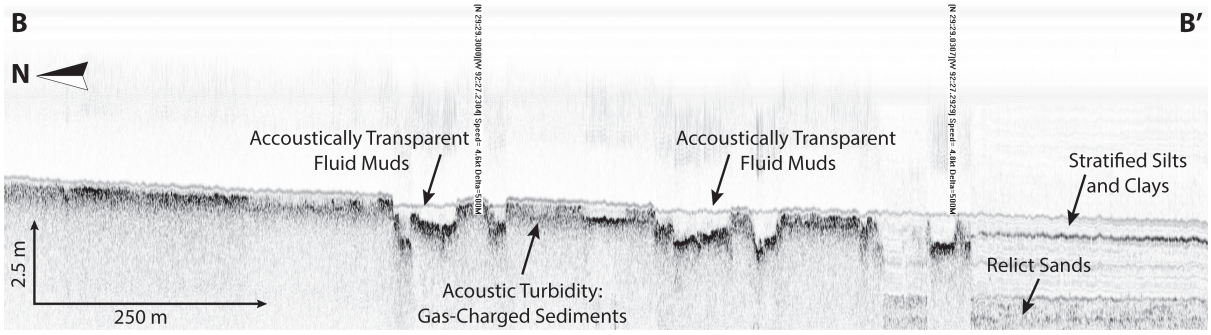

Figure 2.3 (A) CHIRP seismic transect B – B' (Figure 2.2) showing several seabed features including acoustic turbulence, acoustically transparent fluid muds, seabed instability features including collapse depressions, bottleneck slides, and mudflow gullies. Stratified silts and clays overlying relict sands are visible where acoustic turbidity does not mask the underlying seabed stratigraphy.

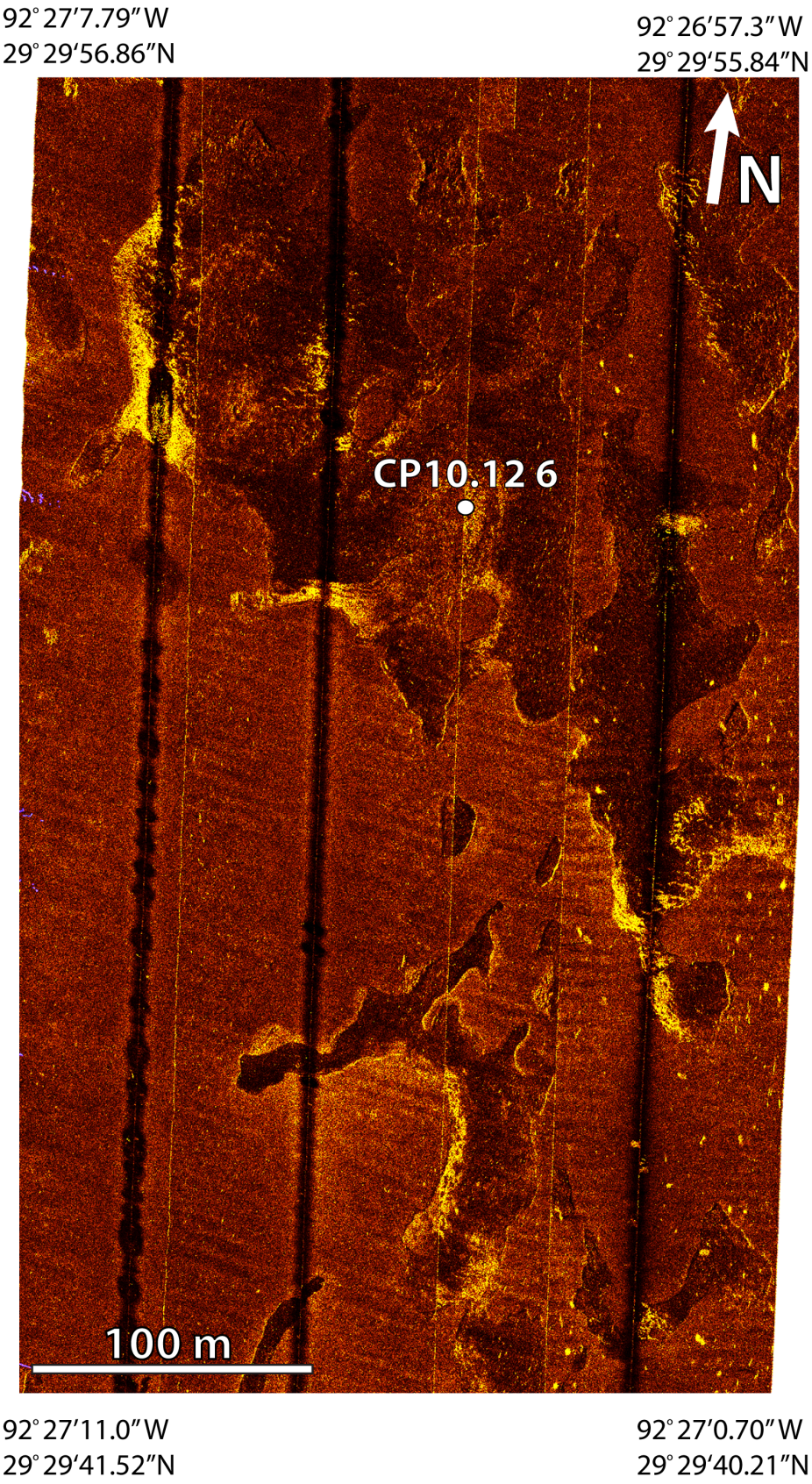

Figure 2.4 Sidescan sonar mosaic showing collapse depressions and bottleneck slides in the vicinity of sampling location CP10.12 6 (Figure 2.2), located on the clinothem rollover. Navigation data errors result in a slight mismatch of survey line overlays in the SE corner of the mosaic.

Figure 2.5 Sidescan sonar mosaic showing collapse depressions, bottleneck slides, and mudflows in the vicinity of sampling location CP10.12 7 (Figure 2.2), located on the clinothem foresets. Navigation data errors result in a slight mismatch of survey line overlays in the SE corner of the mosaic.

2.4.2 Facies Associations

Muddy sediments in the study area are composed primarily of clay-minerals, detrital lithogenic grains, and organic debris (Denommee et al., submitted). Denommee et al. (submitted) show that a significant portion of the silt-sized material within the study area is packaged into aggregate grains ranging in size from fine-silt to fine-sand. Clinothem sediments on the SWLA subaqueous delta exhibit several across-shelf trends. Grain-size analyses reveal that, although most of the coarser-grained sediments have been winnowed out prior to being suspended in the Atchafalaya mudstream, there is a general decrease in silt-sized detrital lithogenic fraction across the shelf (Figure 2.6). It is also observed that, in general, the physical reworking of sediments decreases across shelf while biological reworking increases.

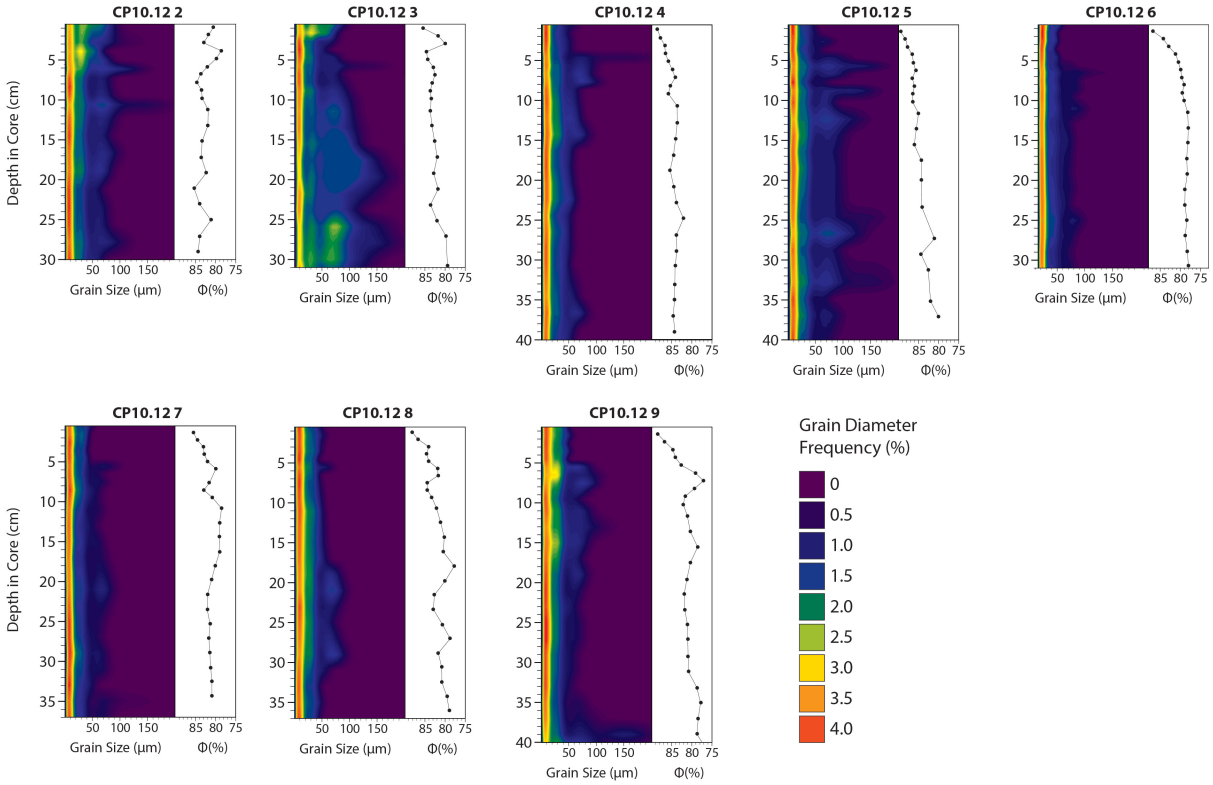

Figure 2.6 Depth profiles of grain diameter percent frequency and porosity trends for sediment cores collected across the clinothem (Figure 2.2).

2.4.2.1 Inner Topsets

Fine-grained sediments on the inner topsets (coring locations CP10.12 2 and 3) are comprised of silt-sized clay-rich aggregate grains, detrital silt-sized lithogenic components, and organic debris (Denommee et al., submitted). X-radiographs (Figure 2.7) reveal sedimentary fabrics that are organized into an irregular succession of mm-thick, discontinuous, wavy, parallel and non-parallel, detrital, silt-rich laminae (white brackets), intercalated with cm- to dm-thick, clay-dominated beds. Some cm-scale migrating ripples with low-angle concave foresets (cf. Schieber and Yawar, 2009) and frequent cm-scale, mm-deep silt-filled gutters are also observed (Figure 2.7). Reworked beds and erosive surfaces are commonly observed on this part of the clinothem. The inner topsets are sparsely bioturbated, with mm- to cm- long vertical polychaete burrows displaying simple cross-cutting relationships being the most frequently observed trace. Infrequent, non-identifiable biodeformational structures are observed, distorting dm-thick intervals (Figure 2.7, blue arrows).

2.4.2.2 Outer Topsets

In terms of grain-size and composition, sediments on the outer topsets (coring locations CP10.12 4 and 5) are similar to those observed on the inner topsets however, the fraction of detrital silt-sized lithogenic components is smaller than what is observed on the inner topsets (Denommee et al., submitted). Outer topset strata are composed of cm- to dm-thick, silt-bearing, clay-dominated event beds, often with wavy, eroded tops (Figure 2.8, white brackets). The bases of these beds contain mm-thick, continuous and discontinuous, wavy, nonparallel silt layers. Single beds can display a tripartite subdivision consistent with the sedimentary fabric produced by CWESGFs (Macquaker et al., 2010; Denommee et al., submitted; yellow arrow). Like the inner topsets, the outer topsets are sparsely bioturbated,

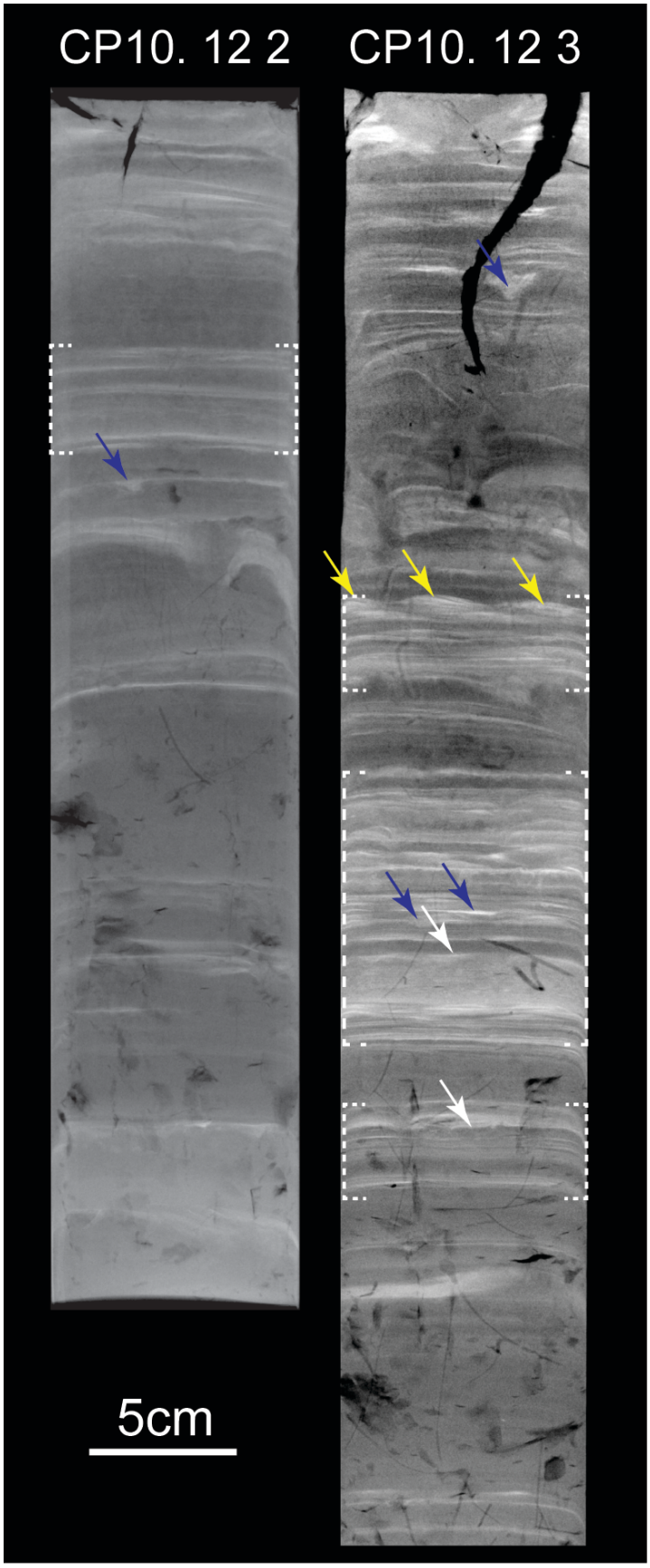

Figure 2.7 X-radiographs of the clinothem inner topsets (sampling locations CP10.12 2 and CP10.12 3).

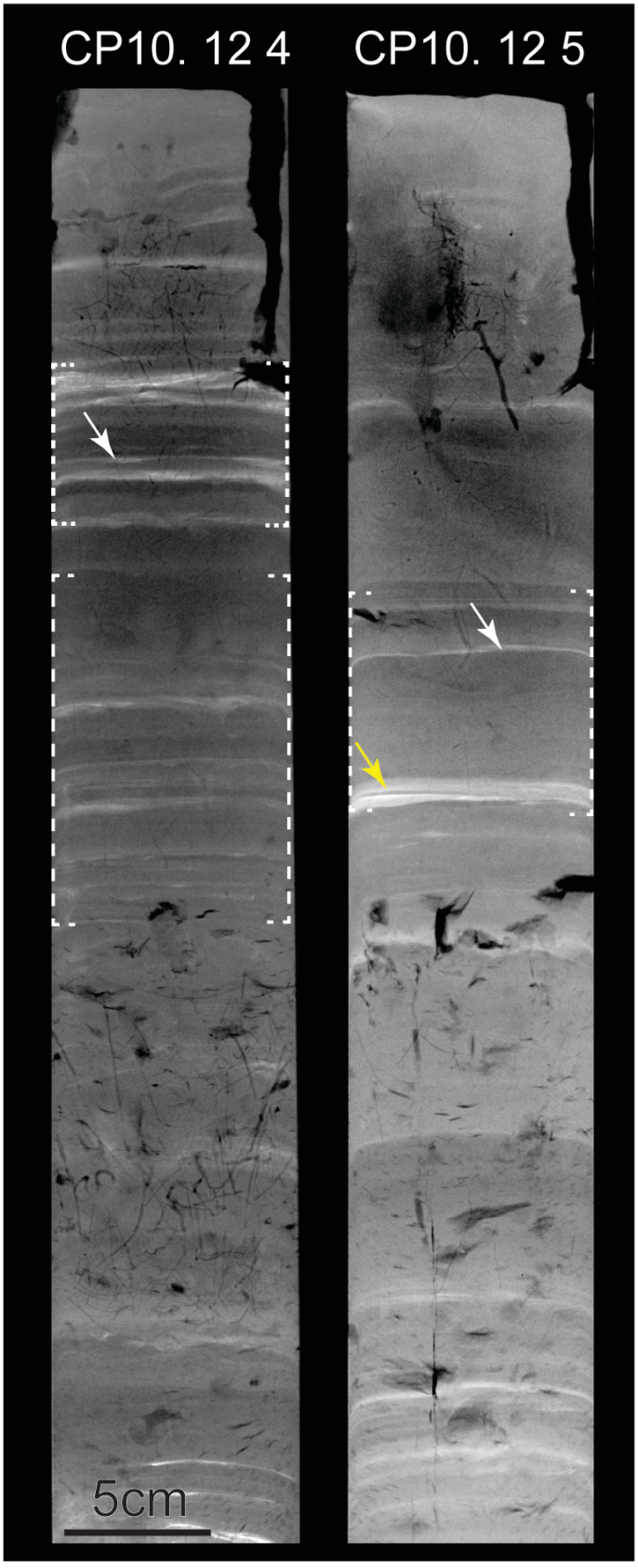

Figure 2.8 X-radiographs of the clinothem outer topsets (sampling locations CP10.12 4 and CP10.12 5).

with mm- to cm- long, vertical polychaete burrows displaying simple cross-cutting relationships. On this part of the clinoform we observe that beds are primarily being colonized from erosional surfaces and that bedding-parallel bioturbation is rare (Figure 2.8).

2.4.2.3 Clinothem Rollover

Sediments collected landward of the clinothem rollover at site CP10.12 6 retain very few primary sedimentary structures due to overprinting by biogenic gas. Isolated, silt-filled gutters however, can be observed near the sediment-water interface (Figure 2.9 blue arrow). Grain-size analysis shows a nearly uniform grain-size distribution at this location (Figure 2.9). X-radiography reveals single gastropod shells near the sediment-water interface; however, no bioturbation is recorded at this site (Figure 2.9). Seaward of the clinothem rollover at site CP10.12 7, muds are organized in homogenous cm- to dm-thick event beds with wavy, erosive bases (white brackets). The event beds composed of either silt- or clay-sized particles. The coarse silt fraction, which comprises an important portion of sediments on the topsets is mostly absent on the seaward portion of the clinothem rollover (Figure 2.9). Only isolated wavy-discontinuous lags composed of silt-sized components and sand-sized bivalve shells (white arrow) are observed at the base of clay-rich layers. The bioturbation intensity at this location is moderate to high, and many event beds exhibit top-down colonization (green brackets) by mostly mm-scale, cm- to dm-long vertical and inclined polychaete burrows (green arrow). Close to the sediment-water interface, mm-thick chondrites-like burrows are observed within a nearly homogenous silt-rich surface layer (green brackets).

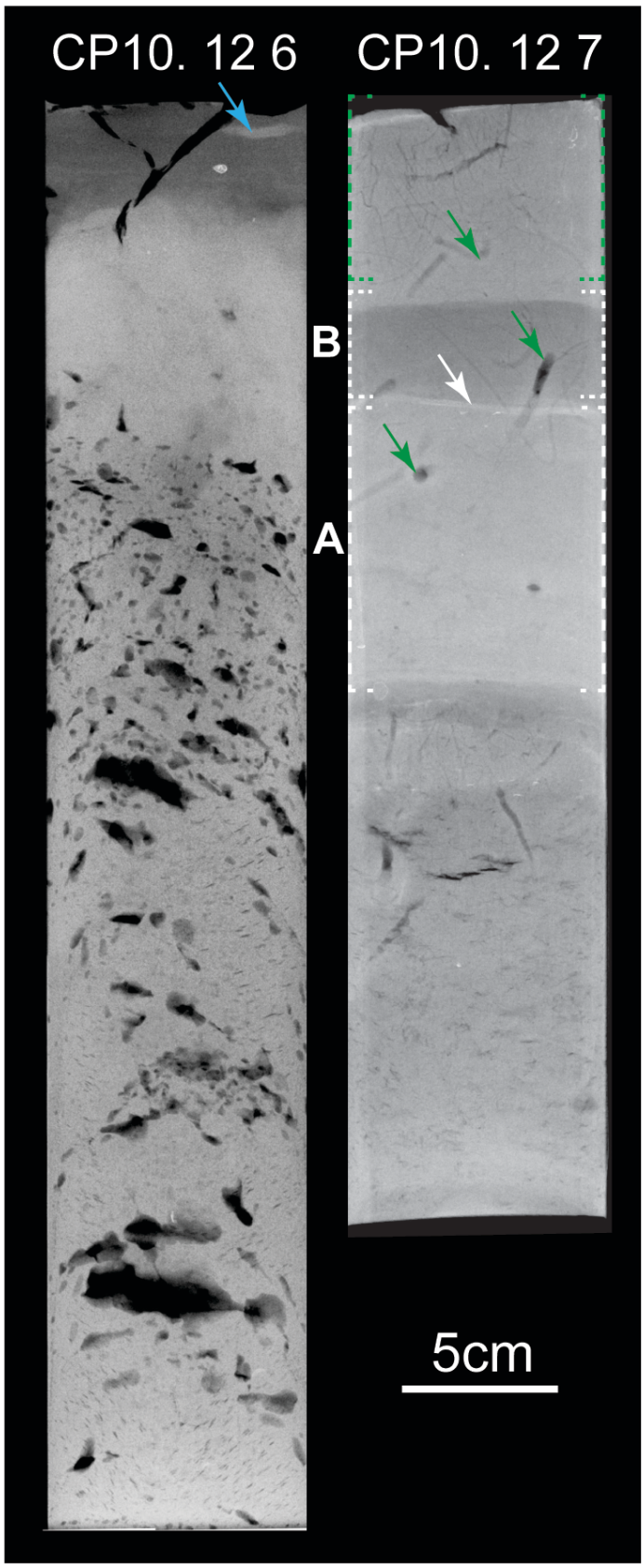

Figure 2.9 X-radiographs of the clinothem rollover (sampling locations CP10.12 6 and CP10.12 7).

2.4.2.4 Foresets

The clinothem foresets display cm- to dm-thick upward-fining event beds with eroded tops. The bases of beds contain continuous, wavy-, cross-laminated silt laminae, overlain by normally graded clay-rich muds (Figure 2.10; white brackets). Silt layers are thicker in comparison with those observed in topset sediments (Figure 2.10). Some thick event layers contain a grain-size break (Figure 2.10; blue arrow) with the overall event bed containing no discernible sedimentary structures. Bioturbation is moderate to high, with mm-scale, cm- to dm-deep vertical and oblique, open burrows (Figure 2.10; green arrows). The level of sediment homogenization by bioturbation is generally low and only muds close to the sediment-water interface are thoroughly mixed (Figure 2.10; yellow arrow). The muds close to the sediment-water interface show mm-thick, chondrites-like burrows (Figure 2.10; green brackets) that cross-cut multiple event beds.

2.4.3 ^{210}Pb and ^{137}Cs Radioisotope Geochronology

Across-shelf profiles for $^{210}Pb_{XS}$ are shown in Figure 2.11. For the most part, $^{210}Pb_{XS}$ profiles do not show the gradual exponential decay with increasing depth that is associated with steady-state sediment accumulation and bioturbation over decadal timescales (Bentley and Nittrouer, 1999). Rather, sediment cores exhibit $^{210}Pb_{XS}$ profiles with nearly uniform activities suggestive of much more rapid and episodic sedimentation. It is therefore unlikely that the conditions assumed in Eq. 1 are met for these sediment cores. It is still possible however, to roughly estimate sediment accumulation rates (SARs) for 4 of the 8 sediment cores collected from the results of the least-squares fits (Eq. 1) to $^{210}Pb_{XS}$ profiles (Figure 2.11). For the outer topsets (coring location CP.10.12 4) SARs are estimated at 4.8 cm/y. Just seaward of the clinothem rollover (coring location CP10.12 7) the SAR is estimated to be ~ 7.5 cm/y, and on the clinothem foresets (stations CP10.12 8 and 9) SARs are estimated to be

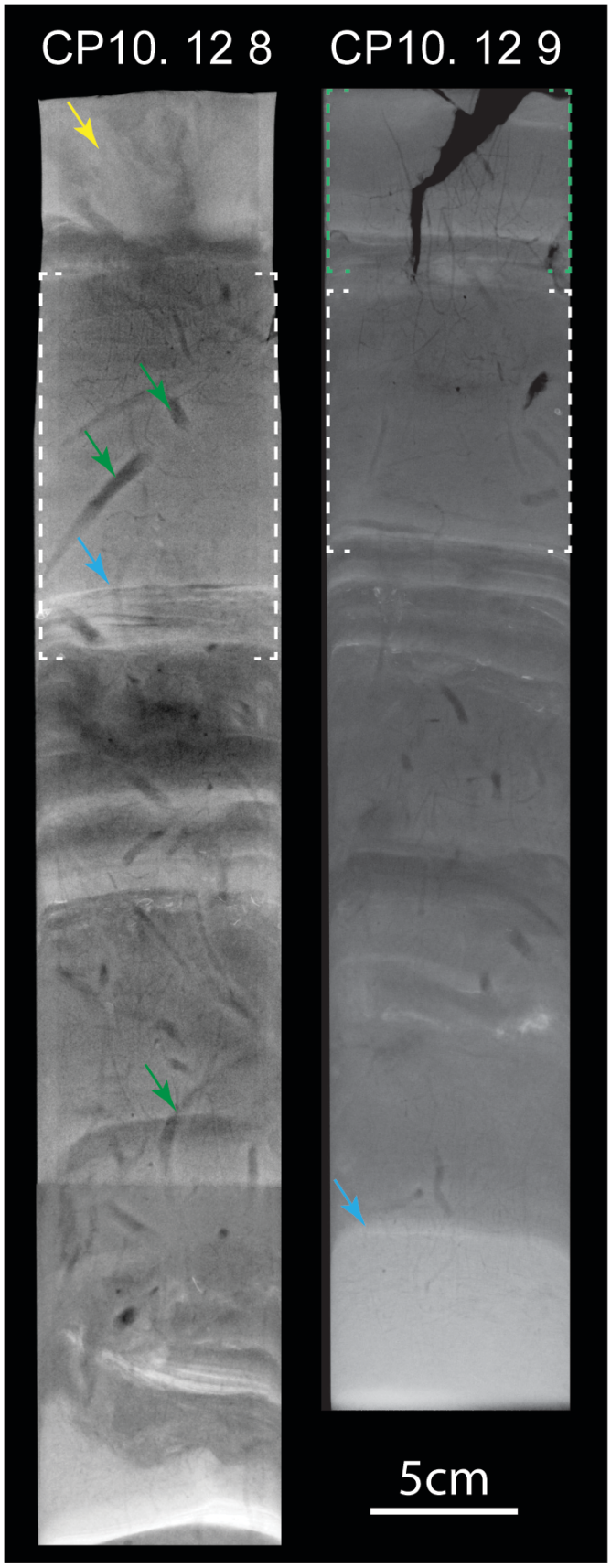

Figure 2.10 X-radiographs of the clinothem foresets (sampling locations CP10.12 8 and CP10.12 9).

between 3.3 and 2.8 cm/y. ^{137}Cs profiles show nearly uniform, low-levels of activity for all core profiles. As sampling was limited by the dense networks of oil and gas infrastructure in the study area no SARs were determined for the bottomset region of the clinothem.

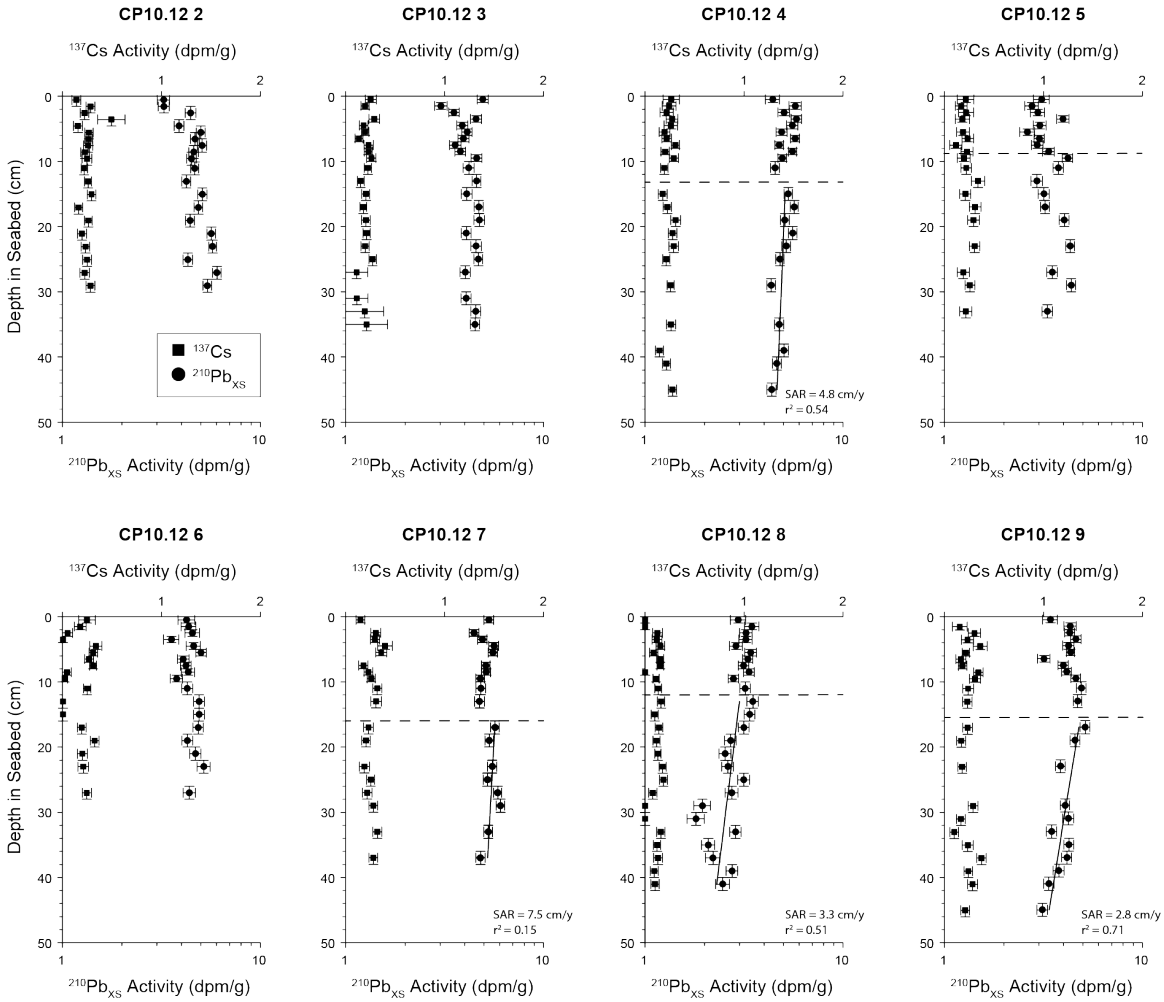

Figure 2.11 $^{210}Pb_{XS}$ and ^{137}Cs profiles for sediment cores CP10.12 2-9

2.5 Discussion

The subaqueous delta clinothem on the SWLA Chenier Plain inner shelf displays many similarities to other subaqueous delta clinothem systems including the Gulf of Papua (Walsh et al., 2004), the Amazon (Kuehl et al., 1986; Nittrouer et al., 1986) and the Ganges-Brahmaputra (Kuehl et al., 1997). Broadly speaking, we observe three trends on the SWLA inner shelf that are typical of most clinothem systems (c.f., Walsh et al., 2004): (1) SARs are

highest on the clinothem foresets; (2) physical sedimentary structures which dominate the clinothem topsets gradually give way to biologically-derived structures as we move further offshore; and (3) there is an observed fining of detritally-derived sediments as we move further offshore. The studied area exhibits many similarities to the nearby subaqueous delta-front region of the much larger Mississippi River bird-foot delta system. Despite the differences in sedimentation rates, sediment texture, seabed gradient and water depths, we observe many of the same seabed instability and mass-movement features that have been catalogued for the Mississippi subaqueous delta front (Coleman et al., 1980).

2.5.1 Mechanisms for Clinothem Progradation

2.5.1.1 Along-Shelf Sediment Transport

Although the focus of this research paper is to investigate the across-shelf processes driving clinothem progradation on the SWLA Chenier Plain subaqueous delta, along shelf processes must also be considered as they are fundamental to the initiation of clinothem progradation. Of particular interest are the processes by which fine-grained sediments derived from the Atchafalaya River are transported the ~200 km west towards the study area. A number of previous studies have investigated these processes (Wells and Kemp, 1981; Roberts, 1998; Allison et al., 2000; Huh et al., 2001; Rotondo and Bentley, 2003; Draut et al., 2005a; Kineke et al., 2006); leading to the determination that the passage of winter cold-fronts (and occasional tropical storms) play an integral role in across-shelf sediment transport. During pre-frontal conditions, the wave energy on the inner shelf increases, resuspending and mixing sediment within the water column (Roberts, 1998). As the cold front passes, the water column becomes stratified and fluid muds develop. Frontal conditions are frequently accompanied by strong along-shore currents (and some onshore transport) that

drive the fluid muds westward (and shoreward) towards the study area as hyperpycnal flows (Roberts, 1998).

2.5.1.2 Across-Shelf Sediment Transport

Current-wave-enhanced-sediment-gravity flow processes play a key role in the across-shelf clinothem mechanics. As is the case for the along-shore transport of sediment, the primary mode of across-shelf CWESGF development within the study area is related to sediment-resuspension events initiated in response to the passage of winter cold fronts and the occasional tropical storm. A detailed description of the evolution of such a flow in the vicinity of the study area is provided in Jaramillo et al. (2009). We are able to identify the sedimentary products of these flows in both X-radiograph, grain size percent frequency distribution, and $^{210}Pb_{XS}$ profiles of sediment cores collected across the clinothem.

On the clinothem topsets X-radiograph negatives show strata that record the following sequence of flow events, consistent with the bed liquefaction and the subsequent evolution of a CWESGF within the study area: (1) basal erosion; (2) turbulent traction transport (i.e., ripple crossbedding and migrating ripples); (3) limited laminar sediment gravity flow (i.e., mm-scale intercalated silts and clays); and (4) suspension settling from waning flow (i.e., subtly normally-graded beds (Figures 2.7 and 2.8 inner and outer topset cores). The sparse nature of the bioturbation on this portion of the clinothem is consistent with a relatively energetic seabed that is subject to frequent resuspension and deposition.

Towards the clinothem rollover, the sedimentary strata develop a distinct character reflective of the depositional processes on this portion of the inner shelf. While much of the primary sedimentary fabric landward of the rollover (sampling location CP10.12 6) has been overprinted by the development of biogenic gas within the seabed (Figure 2.9), the grain-size profile retains important textural information (Figure 2.6). Here we see that unlike on the

clinothem topsets, there is little variation in the grain-size profile (nearly uniform grain-size distribution with depth). It is also important to note that the percentage of relatively coarse, siliceous silt-sized grains is much lower on this portion of the clinothem than on either the topsets or on the foresets, suggesting that this size fraction is bypassing the rollover and being deposited on the clinothem foresets and/or bottomsets (Denommee et al., submitted).

Seaward of the clinothem rollover at sampling location CP10.12 7, the sedimentary strata are distinct from those observed on shallower portions of the clinothem. Here strata are composed of normally-graded event beds. Notably lacking from this portion of the clinothem are the siliceous silt-sized grains (Figure 2.6) that are observed on shallower portions of the clinothem, concentrated within sedimentary fabrics that are understood to be deposited from CWESGFs (e.g., ripple crossbedding, intercalated silts and clays). It is likely that these flows do not deposit sediment on this portion of the clinothem, and rather the sediment is carried further offshore to the clinothem bottomsets where increasing water depths reduce the energy within the bottom boundary layer and bedload sediments are deposited.

On the clinothem foresets (sampling locations CP10.12 8 and 9; Figure 2.10) we see evidence of sediments being deposited by multiple mechanisms. We see evidence for both CWESGF-type deposits with their diagnostic tripartite motif (cf. Macquaker et al., 2010), as well as erosive-based, normally graded, non-laminated "tempestite-like" event beds. CWESGF-type beds contain significant proportion of silt-sized detrital grains (Denommee et al., submitted). Bioturbation on this portion of the clinothem is, as would be expected, more intense than on shallower portions of the clinothem. Colonization surfaces within the strata indicate that the nature of sediment delivery to this portion of the clinothem is episodic, consistent with both CWESGF and mass-failure-driven sediment transport. Event beds on this portion of the clinothem have two likely mechanisms of formation: (1) mass-failures (e.g., bottle-neck slides and silt flows) which are observed in both side-scan and CHIRP data

or by (2) gravity-flows (i.e., tempestites) triggered by strong storms such as the tropical cyclones that episodically pass over the region.

Detailed $^{210}Pb_{XS}$ profiles (Figure 2.11) support the interpretation of sediment transport mechanisms made based on the sedimentary textures and fabrics observed within the study area. Across the clinothem we see a well-defined ephemeral layer between 12-15cm in the seabed, below which the $^{210}Pb_{XS}$ profiles vary – with marked differences between the different geomorphic elements (e.g., topset, rollover, and foresets). The near vertical $^{210}Pb_{XS}$ profiles observed on the clinothem inner topsets (CP10.12 2 and 3; Figure 2.7) are likely the product of frequent episodes of seabed liquefaction, sediment resuspension, transport/mixing, and redeposition – processes consistent with the development of CWESGFs in shallow water. On the seaward margin of the rollover and the clinothem foresets (CP10.12 7-9; Figures 2.9 and 2.10) $^{210}Pb_{XS}$ profiles below the ephemeral layer display the type of non-steady state deposition that could be attributed to frequent, episodic sediment input.

2.5.2 Mass Movement Triggering Mechanisms

As CWESGF processes do not account for the full range of sediment transport features observed on and within the seabed, they cannot be the sole mechanism responsible for clinothem progradation. In fact, the seabed is heavily modified by mass movement processes that are likely key mechanisms for redistributing sediments seaward. The initial stability of the seabed has a strong influence on whether or not mass-movement will occur at low gradients. High sedimentation rates (Figure 2.11), clay-rich, fine-grained sediments (Figure 2.6), and an abundance of organic matter and seabed gas (Figure 2.3) all combine within the study area such that the seabed on the clinothem is highly susceptible to the initiation of instability, collapse, and flow despite of the shallow gradient and weak gravitational stresses.

2.5.2.1 The Role of Waves

In shallow water, the largest shear stresses exerted on the seabed may be induced by the passage of storm waves (Lee and Edwards, 1986). It is thus likely that the primary triggering mechanism for the mass movements observed on the SWLA inner shelf subaqueous delta is the cyclic loading of the seabed by passing storm waves (Henkel, 1970; Seed and Rahman, 1978). As waves pass, the seafloor is subject to travelling pressure waves (increased pressure under wave crests and decreased pressure under troughs) which can induce cyclic stresses within the pore systems of the seabed, leading to the progressive build-up of pore pressure.

The geometry of the problem is illustrated in Figure 2.12 and it can be hypothesized that the seabed will be at the point of failure when disturbing moment (M_d) is equal to the moment of resistance (M_r), and failure will occur when $M_d > M_r$. The solution for the condition where $M_d = M_r$ can be written as (Henkel, 1970):

$$\frac{\Delta p}{k\gamma' L} = 4\pi^2 \left(\frac{x}{L}\right)^3 \frac{1}{[A]}\left\{[B] - \frac{\beta}{3k}\right\} \quad (2)$$

with:

$$[A] = \sin\alpha - \alpha\cos\alpha \qquad [B] = \frac{\sin\theta - \theta\cos\theta}{\sin^3\theta} \qquad k = \frac{c_u}{\gamma' z}$$

where: Δp is the magnitude of the wave-induced sinusoidal pressure change, $\gamma' z$ is submerged weight of the overlying sediment (N/m^2), L is wavelength (m), x is the half-length, α defines the portion of the wave-induced loading acting on the chosen length of the slide, 2θ is the arc of sliding, β is the slope angle, and c_u is the undrained shear strength of the shallow seabed, and z is depth (m) (Figure 2.12; from Henkel, 1970).

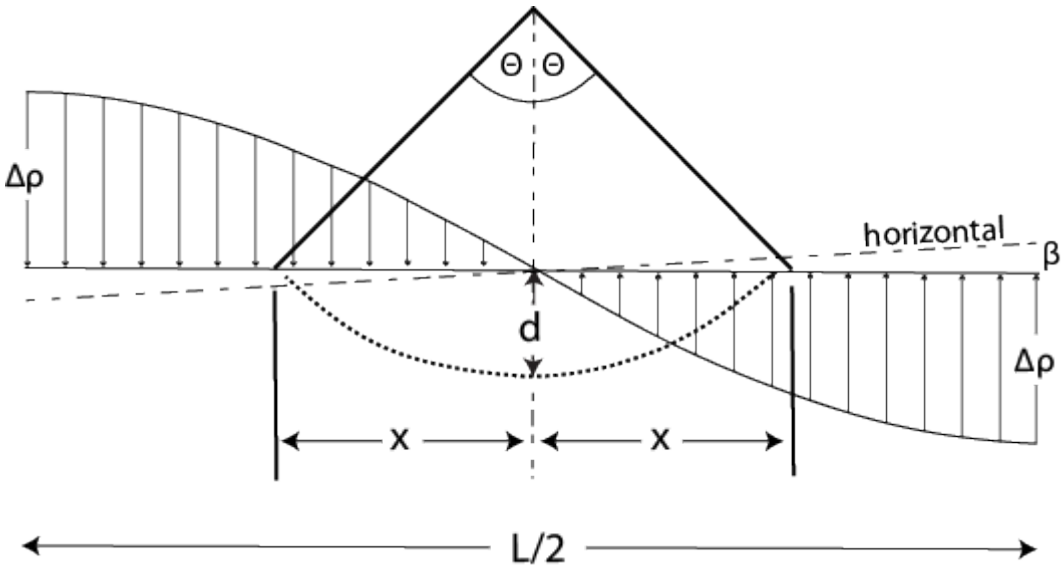

Figure 2.12 Relationship between water depth, wavelength, wave height, and wave-induced pressure change on the sea bottom (after Henkel, 1970).

To relate these calculations to the study area the following values of k= 0.5 (which accounts for excess pore pressure to some degree), were used (after Henkel, 1970). The results of these calculations for a typical range of shelf conditions are presented in Figure 2.13. Theoretically, a value of Δp greater than ~0.5 Pa is sufficient to generate shear stresses such that the disturbing is greater than the moment of resistance (i.e., initiation of slope failure). For typical shelf conditions during a cold front passage, with T = 6 sec, waves are predicted to generate slope failure in as little as ~4m water depth, corresponding to the clinothem rollover. In typical fair weather conditions (T < 6 sec), wave-induced pore-pressures appear to be insufficient to cause slope failure at any point on the shallow clinothem (Figure 2.13). Although larger wave periods are not typical for this area, if wave period were to increase (e.g., to 8 sec), wave-induced pore pressures could be sufficient to cause slope failure across the shelf. In spite of this crude approach, it can be illustrated that bottom pressure effects due to the passage of waves typical for the study area (i.e., ~ 6 s) are sufficient to trigger slope failure for certain regions of the clinothem.

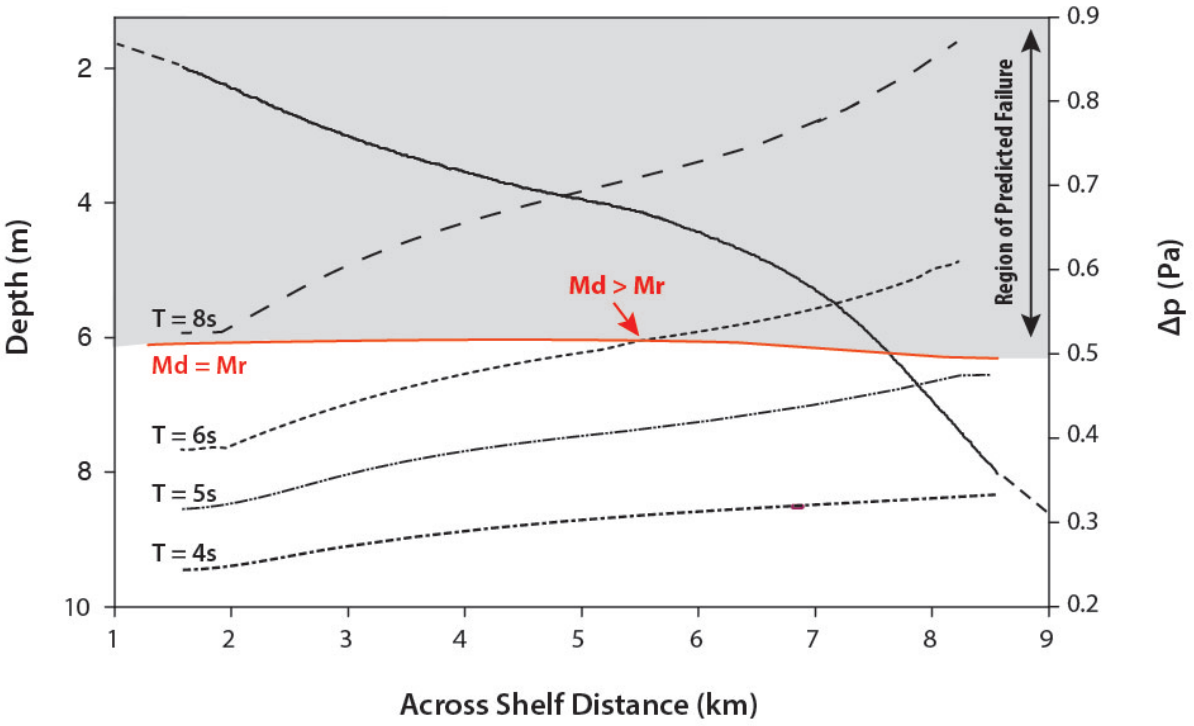

Figure 2.13 Relationship between Δp (Henkel, 1970), water depth, and wavelength (wave period) across the SWLA inner shelf. The shaded area indicates the magnitude of the wave-induced sinusoidal pressure change capable of causing slope failure. For T < 6, failure is not predicted to occur. For T = 6, failure will occur at 5.5m offshore, in ~4m water depth, while for T = 8 the pressure change is sufficient to cause failure across the shelf. Deep-water wave height = 1.5 m for all scenarios.

Seed and Rahman (1978) improved upon the Henkel method and developed the following relation which defines the conditions under which seabed liquefaction may occur:

$$\tau_c = f_z f_d 2\pi \left(\frac{\gamma_w}{\gamma'}\right)\left(\frac{H}{L}\right)\sigma_v' \quad (3)$$

with:

$$\sigma_v' = \sigma_v - u \qquad \sigma_v = hg\cos^2\theta\left(\gamma' - \gamma_w\right)\tan\phi$$

where τ_c is the peak cyclic shear stress, σ'_v is vertical effective stress, $f_z = \exp(-2\pi z/L)$, $f_d = 0.5[1/\cosh(2\pi d/L)]$, γ_w is the unit weight of water, γ' is the buoyant unit weight of sediment, H is wave height, z is depth below seabed, L is wave length, d is water depth, u is

the excess pore pressure, h is the slide thickness, θ is the slope angle (term β from Henkel (1970)), and ϕ is the internal angle of friction. For sediment instability to occur, pore water pressures generated by rapid sedimentation, wave perturbation, and/or biogenic gas must exceed vertical effective stress such that $\tau_c/\sigma_v' > 1$ (Prior and Suhayda, 1978).

Although no measurements of excess pore pressure were available from within the study area, values of excess pore pressure of 1.25Pa consistent with gas-induced excess pore pressure values determined for gas-charged sediments in Eckernfjorde Bay (Wever et al., 1998) were used. This is an area where broadly speaking the sedimentation and gas-charging processes are similar to those observed within the study area. Although the Seed and Rahman (1978) model is generally considered to be an improvement on the Henkel (1970) model, because it incorporates an effective stress term it requires information on excess pore pressures generated in response to rapid sedimentation and gas charging. This information is not available for most depositional settings.

The results of these calculations are presented in Figure 2.14. The results are compared to the critical shear stress determined experimentally by Sahin et al. (2012), where critical shear stress for Atchafalaya sediment with 20% solids was estimated at 2.74Pa. This value was chosen because at 50cm depth below the seafloor, average porosity in sediments in the study area was estimated to be 80% (Figure 2.6). This is also the depth along which we see evidence for mass wasting in CHIRP sonar (Figure 2.3). We see from the Seed and Rahman model that under typical cold front conditions with T = 6 sec and deep water wave height = 1.5, that wave-generated shear stresses exceed the critical shear stress value across the shelf. The critical shear stress value of 2.74Pa (equivalent to ~0.28 kg/m^2) determined experimentally by Sahin et al. (2012) does not account for vertical stress however, and therefore must be considered an absolute minimum value for shear failure.

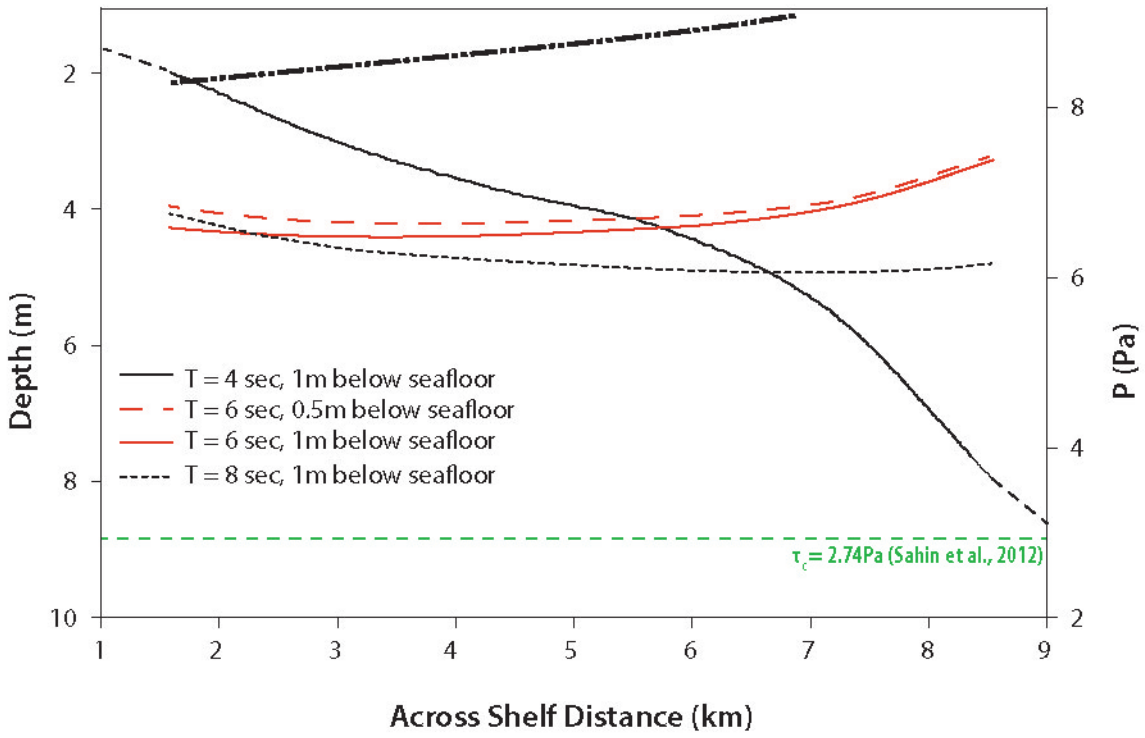

Figure 2.14 Relationship between induced peak cyclic shear stress below the seabed and wave period across the SWLA inner shelf as determined using the method proposed by Seed and Rahman (1979) compared to the value of τ_c as determined by Sahin et al. (2012). For all values wave period and deep water wave height typical for the study area, the shear stress generated by the cyclic loading of waves on the seabed exceeds the critical shear stress for sediments with 20% by volume solids of 2.74, roughly equitable to sediments 0.5m below the seabed.

In order to fully appreciate the implications of the results of the Seed and Rahman (1978) model, we must consider other consequences of wave loading on seabed stability on the clinothem beyond simple failure along a plane of weakness. Specifically we must consider that under increased stress the seabed may approach a state of liquefaction rather than simply fail along a plane of weakness (Clukey et al., 1985). This is an especially important consequence in settings like the SWLA inner shelf, where sediments are weak and under consolidated. When liquefaction occurs, the shear required to initiate downslope sediment transport by currents and wave-orbital velocities in the bottom boundary is significantly reduced. This interpretation is supported by shallow-shelf observations from this

study as well as previous investigations (e.g., Rotondo and Bentley, 2003; Jaramillo et al., 2009; Denommee and Bentley, 2013) where seabed liquefaction leading to offshore fluid mudflows has been frequently observed and where slope-failure features such as rotational slumps are absent.

2.5.3 Synthesis of Observations

Figure 2.15 presents a schematic cartoon of the processes responsible for the across-shelf progradation of the subaqueous delta clinothem. The process is controlled by seasonal variations in sediment discharge and shelf hydrodynamics, and is initiated by the delivery of fine-grained sediments sourced from the Atchafalaya River (e.g., Allison et al., 2001; Draut et al., 2005a; Jaramillo et al., 2009).

(A) When sediment supply to the study area is high (e.g., during maximum river discharge in the late spring and early summer), waves are readily attenuated on the inner shelf (Sheremet et al., 2011). The passage of a frontal system coincident with high sediment availability may initiate a CWESGF that is capable of rapidly transferring sediment seaward (Rotondo and Bentley, 2003); depositing high-porosity, organic-rich material on the clinothem rollover and foresets.

(B) When sediment flux to the clinothem is low (e.g., during the winter and early spring when cold fronts most commonly pass through the study area) wave action on the seabed cannot be attenuated and the seabed is subject in intense wave-reworking. This can lead to both the development a CWESGF (Jaramillo et al., 2009) and/or mass-failures such as bottle neck slides and mudflows. Additionally, the reduction of organic matter within the seabed leads to the development of biogenic gas. This is gas-charged sediment is highly susceptible to developing seabed instabilities such as collapse depressions, seabed liquefaction, and mass-movements including mud flows that are capable of transferring large

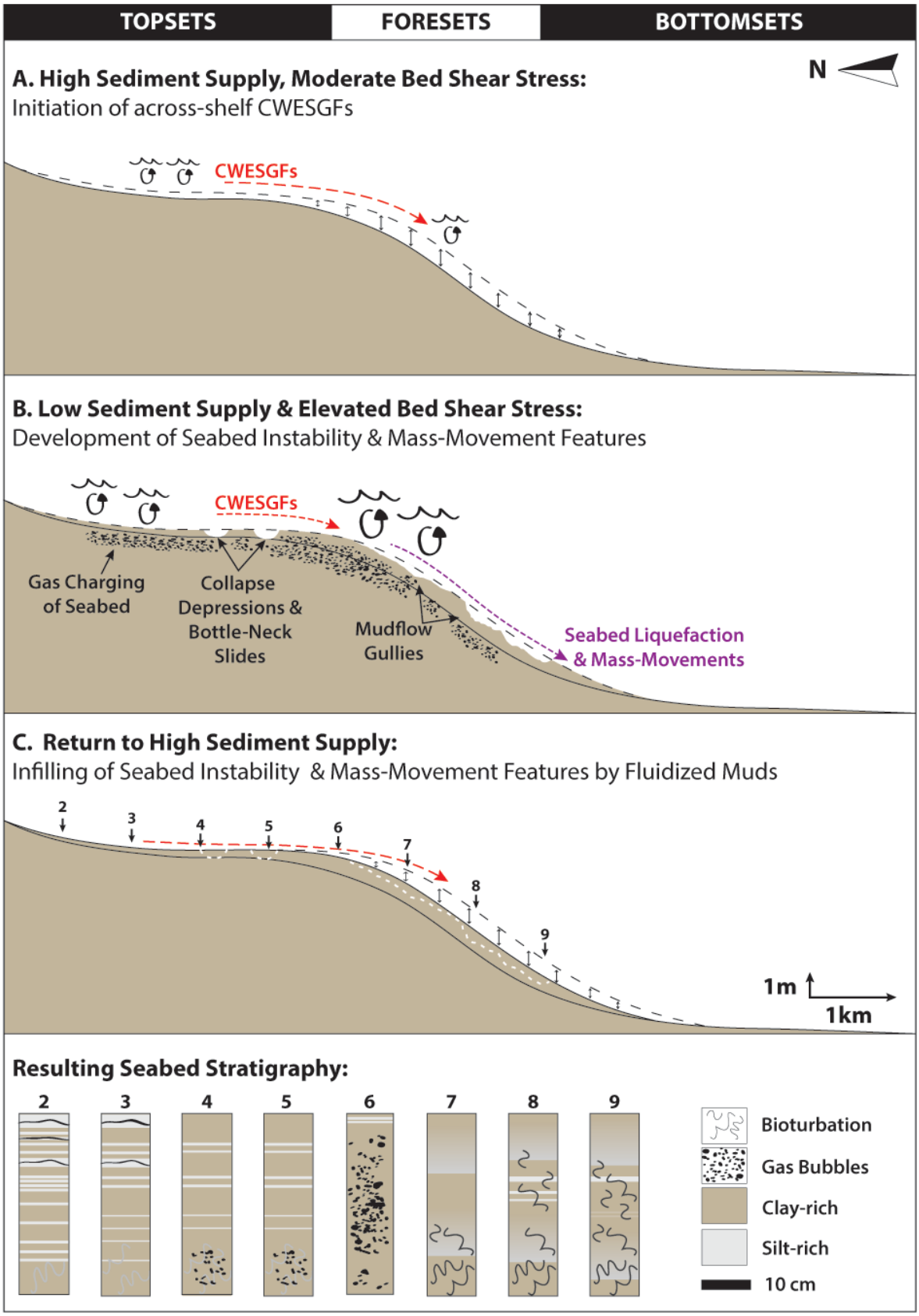

Figure 2.15 Schematic drawing of processes controlling progradation on the clinothem.

volumes of sediment seaward and leaving erosive features on the seabed. These are most likely triggered by the cyclic loading of waves on the seabed.

(C) Subsequently, CWESGFs and/or tempestites in-fill collapse depressions, bottle neck slides, and mudflow gullies with acoustically transparent, fluidized muds. Given that CHIRP sonar reveals that this acoustically transparent mud also covers the clinothem in a near uniform fashion; it is likely that the majority of this infilling occurs when sediment supply is high (i.e., during subsequent river flooding).

While it is well understood that CWESGFs play an important role in muddy, subaqueous delta clinothem mechanics – transporting sediments across low-gradient shelves the more subtle consequences of these flows remain poorly understood. These flows result in the deposition of a seabed that is inherently weak and prone to mass-movements that, for the most part, have been observed to develop in regions with both much higher sedimentation rates and gradients, such as the Mississippi subaqueous delta front. This study shows however, that when the seabed is first modified by processes capable of operating on extremely shallow gradients such as CWESGFs, mass-movements can easily initiate and become a key component of the clinothem's mechanics. These important sediment dispersal mechanisms should be considered by and integrated into muddy, low-gradient clinothem sedimentation models.

2.6 Conclusions

1. A combination of sediment transport processes including CWESGFs and mass-movements and seabed liquefaction triggered by waves associated with the passage of cold fronts and tropical storms are responsible for clinothem progradation on the SWLA Chenier Plain clinothem (Figure 2.13).

2. Despite its low gradient, the SWLA Chenier Plain inner shelf subaqueous delta environment exhibits many conditions suitable for the initiation of sediment failure, collapse and flow. This is because CWESGFs are the initial mechanism by which sediments are mobilized across-shelf. CWESGF deposits weak and are by nature (fine-grained, rapidly deposited, high porosity) susceptible to seabed instability and mass-failure.

3. Seabed morphology on the SWLA Chenier Plain subaqueous delta clinothem is strikingly similar to that of the Mississippi bird-foot subaqueous delta front. This is likely because despite the obvious differences between the two depositional settings, similar hydrodynamic processes (i.e., the cyclic loading of weak seabed material by waves) control seabed processes on both subaqueous deltas is the same.

4. When the seabed is modified by processes capable of operating on extremely shallow gradients such as CWESGFs, mass-movements can easily initiate and become a key component of the clinothem's mechanics. As should these should be considered by and integrated into muddy, low-gradient clinothem sedimentation models.

2.7 Acknowledgements

This work was supported through the Billy and Anne Harrison endowment awarded to SJB as well as student research grants (AAPG, SEPM, GSA, and GCAGS) awarded to KCD. The authors would like to thank the LSU Coastal Studies Institute field support unit, Nicholas Decker and Matthew Smith for their help with sediment core and geophysical data collection. Melissa Ausburn and Brandon Thibodeaux are thanked for their help with radioisotope sample preparation and analysis. Joe Kington is thanked for his help with Matlab® and Angelia Freeman is thanked for her help with SonarWiz®.

2.8 References

Allison, M. A., Kineke, G. C., Gordon, E. S., and Goni, M. A., 2000, Development and reworking of a seasonal flood deposit on the inner continental shelf off the atchafalaya river: Continental Shelf Research, v. 20, no. 16, p. 2267-2294.

Bentley, S. J., and Nittrouer, C. A., 1999, Physical and biological influences on the formation of sedimentary fabric in an oxygen-restricted depositional environment: Eckernforde bay, southwestern baltic sea: Palaios, v. 14, no. 6, p. 585-600.

Bentley, S. J., and Nittrouer, C. A., 2003, Emplacement, modification, and preservation of event strata on a flood-dominated continental shelf: Eel shelf, northern california: Continental Shelf Research, v. 23, no. 16, p. 1465-1493.

Bentley, S. J., Rotondo, K., Roberts, H. H., Stone, G. W., & Huh, O. K., 2003. Transport and accumulation of cohesive fluvial sediments on the inner shelf: From the Atchafalaya River downdrift to the Louisiana Chenier Plain. In Proceedings of the International Conference on Coastal Sediments.

Clukey, E., Kulhawy, F., Liu, P. F., and Tate, G., 1985, The impact of wave loads and pore-water pressure generation on initiation of sediment transport: Geo-Marine Letters, v. 5, no. 3, p. 177-183.

Coleman, D., Garrison, L., and Lee, H., 1993, Slope failures in an area of high sedimentation rate: Offshore mississippi river delta: Submarine Landslides: Selected Studies in the US Exclusive Economic Zone, p. 79.

Coleman, J. M., Prior, D. B., and Garrison, L. E., 1980, Subaqueous sediment instabilities in the offshore mississippi river delta, Open-File Rept. 8001.

Cutshall, N. H., Larsen, I. L., and Olsen, C. R., 1983, Direct analysis of Pb-210 in sediment samples - self-absorption corrections: Nuclear Instruments & Methods in Physics Research, v. 206, no. 1-2, p. 309-312.

Denommee, K.C. and Bentley, S.J., 2013, Influence of mass-transport processes on clinothem mechanics on the Southwest Louisiana Shelf: Gulf Coast Association of Geological Societies Transactions, v. 63, p. 205-212.

Denommee, K.C., Bentley, S.J., Harazim, D., and Macquaker, J.H.S., *Submitted*, Hydrodynamic controls on muddy sedimentary fabric development: Atchafalaya Chenier Plain Subaqueous Delta.

Draut, A. E., Kineke, G. C., Huh, O. K., Grymes, J. M., Westphal, K. A., and Moeller, C. C., 2005a, Coastal mudflat accretion under energetic conditions, Louisiana chenier-plain coast, USA: Marine Geology, v. 214, no. 1-3, p. 27-47.

Draut, A. E., Kineke, G. C., Velasco, D. W., Allison, M. A., and Prime, R. J., 2005b, Influence of the atchafalaya river on recent evolution of the chenier-plain inner continental shelf, northern gulf of mexico: Continental Shelf Research, v. 25, no. 1, p. 91-112.

Friedrichs, C. T., and Wright, L. D., 2004, Gravity-driven sediment transport on the continental shelfimplications for equilibrium profiles near river mouths: Coastal Engineering, v. 51, no. 8-9, p. 795-811.

Henkel, D. J., 1970, The role of waves in causing submarine landslides: Geotechnique, v. 20, no. 1, p. 75-80.

Huh, O. K., Walker, N. D., and Moeller, C., 2001, Sedimentation along the eastern chenier plain coast: Down drift impact of a delta complex shift: Journal of Coastal Research, v. 17, no. 1, p. 72-81.

Jaramillo, S., Sheremet, A., Allison, M. A., Reed, A. H., and Holland, K. T., 2009, Wave-mud interactions over the muddy Atchafalaya subaqueous clinoform, Louisiana, United States: Wave-supported sediment transport: Journal of Geophysical Research: Oceans, v. 114, no. C4, p. C04002.

Karner, G. D., and Driscoll, N. W., 1999, Tectonic and stratigraphic development of the west African and eastern Brazilian margins: Insights from quantitative basin modelling: Geological Society, London, Special Publications, v. 153, no. 1, p. 11-40.

Kemp, P. F., 1986, Deposition of organic-matter on a high-energy sand beach by a mass stranding of the cnidarian velella-velella (l): Estuarine Coastal and Shelf Science, v. 23, no. 4, p. 575-579.

Kineke, G. C., Higgins, E. E., Hart, K., and Velasco, D., 2006, Fine-sediment transport associated with cold-front passages on the shallow shelf, Gulf of Mexico: Continental Shelf Research, v. 26, no. 17-18, p. 2073-2091.

Kineke, G. C., and Sternberg, R. W., 1995, Distribution of fluid muds on the Amazon continental-shelf: Marine Geology, v. 125, no. 3-4, p. 193-233.

Kineke, G. C., Sternberg, R. W., Trowbridge, J. H., and Geyer, W. R., 1996, Fluid-mud processes on the Amazon continental shelf: Continental Shelf Research, v. 16, no. 5-6, p. 667-696.

Kuehl, S. A., DeMaster, D. J., and Nittrouer, C. A., 1986, Nature of sediment accumulation on the Amazon continental shelf: Continental Shelf Research, v. 6, no. 1–2, p. 209-225.

Kuehl, S. A., Levy, B. M., Moore, W. S., and Allison, M. A., 1997, Subaqueous delta of the Ganges-Brahmaputra river system: Marine Geology, v. 144, no. 1-3, p. 81-96.

Lee, H. J., and Edwards, B. D., 1986, Regional method to assess offshore slope stability: Journal of Geotechnical Engineering-Asce, v. 112, no. 5, p. 489-509.

Lee, H. J., Locat, J., Desgagnés, P., Parsons, J. D., McAdoo, B. G., Orange, D. L., Puig, P., Wong, F. L., Dartnell, P., and Boulanger, E., 2009, Submarine mass movements on continental margins, Continental margin sedimentation, Blackwell Publishing Ltd., p. 213-274.

Macquaker, J. H. S., Bentley, S. J., and Bohacs, K. M., 2010, Wave-enhanced sediment-gravity flows and mud dispersal across continental shelves: Reappraising sediment transport processes operating in ancient mudstone successions: Geology, v. 38, no. 10, p. 947-950.

Nittrouer, C. A., Kuehl, S. A., Demaster, D. J., and Kowsmann, R. O., 1986, The deltaic nature of Amazon shelf sedimentation: Geological Society of America Bulletin, v. 97, no. 4, p. 444-458.

Palinkas, C. M., and Nittrouer, C. A., 2006, Clinoform sedimentation along the Apennine shelf, Adriatic Sea: Marine Geology, v. 234, no. 1-4, p. 245-260.

Patruno, S., Hampson, G. J., and Jackson, C. A. L., 2015, Quantitative characterisation of deltaic and subaqueous clinoforms: Earth-Science Reviews, v. 142, no. 0, p. 79-119.

Pirmez, C., Pratson, L. F., and Steckler, M. S., 1998, Clinoform development by advection-diffusion of suspended sediment: Modeling and comparison to natural systems: Journal of Geophysical Research: Solid Earth, v. 103, no. B10, p. 24141-24157.

Pratson, L. F., Nittrouer, C. A., Wiberg, P. L., Steckler, M. S., Swenson, J. B., Cacchione, D. A., Karson, J. A., Murray, A. B., Wolinsky, M. A., Gerber, T. P., Mullenbach, B. L., Spinelli, G. A., Fulthorpe, C. S., O'Grady, D. B., Parker, G., Driscoll, N. W., Burger, R. L., Paola, C., Orange, D. L., Field, M. E., Friedrichs, C. T., and Fedele, J. J., 2009, Seascape evolution on clastic continental shelves and slopes, Continental margin sedimentation, Blackwell Publishing Ltd., p. 339-380.

Prior, D. B., and Suhayda, J. N., 1979, Application of infinite slope analysis to subaqueous sediment instability, Mississippi Delta: Engineering Geology, v. 14, no. 1, p. 1-10.

Prior, D. B., Yang, Z. S., Bornhold, B. D., Keller, G. H., Lu, N. Z., Wiseman, W. J., Jr., Wright, L. D., and Zhang, J., 1986, Active slope failure, sediment collapse, and silt flows on the modern subaqueous Huanghe (Yellow River) delta: Geo-Marine Letters, v. 6, no. 2, p. 85-95.

Roberts, H. H., 1998, Delta switching: Early responses to the Atchafalaya river diversion: Journal of Coastal Research, v. 14, no. 3, p. 882-899.

Rotondo, K., and Bentley, S. J., 2003, Deposition and resuspension of fluid mud on the western Louisiana inner shelf:: Gulf Coast Association of Geological Societies Transactions, v. 53, p. 722-731.

Sahin, C., Safak, I., Sheremet, A., and Mehta, A. J., 2012, Observations on cohesive bed reworking by waves: Atchafalaya shelf, Louisiana: Journal of Geophysical Research: Oceans, v. 117, no. C9, p. C09025.

Schieber, J., and Yawar, Z., 2009, A new twist on mud deposition—mud ripples in experiment and rock record: The Sedimentary Record, v. 7, no. 2, p. 4-8.

Schneider, C. A., Rasband, W. S., and Eliceiri, K. W., 2012, Nih image to imagej: 25 years of image analysis: Nat Meth, v. 9, no. 7, p. 671-675.

Seed, H. B., and Rahman, M. S., 1978, Wave-induced pore pressure in relation to ocean-floor stability of cohesionless soils: Marine Geotechnology, v. 3, no. 2, p. 123-150.

Sheremet, A., Jaramillo, S., Su, S. F., Allison, M. A., and Holland, K. T., 2011, Wave-mud interaction over the muddy Atchafalaya subaqueous clinoform, Louisiana, United States: Wave processes: Journal of Geophysical Research-Oceans, v. 116.

Sheremet, A., and Stone, G. W., 2003, Observations of nearshore wave dissipation over muddy sea beds: Journal of Geophysical Research-Oceans, v. 108, no. C11.

Slingerland, R., Driscoll, N. W., Milliman, J. D., Miller, S. R., and Johnstone, E. A., 2008, Anatomy and growth of a Holocene clinothem in the Gulf of Papua: Journal of Geophysical Research: Earth Surface, v. 113(F1).

Sternberg, R. W., Cacchione, D. A., Paulson, B., Kineke, G. C., and Drake, D. E., 1996, Observations of sediment transport on the Amazon subaqueous delta: Continental Shelf Research, v. 16, no. 5-6, p. 697-715.

Traykovski, P., Geyer, W. R., Irish, J. D., and Lynch, J. F., 2000, The role of wave-induced density-driven fluid mud flows for cross-shelf transport on the Eel river continental shelf: Continental Shelf Research, v. 20, no. 16, p. 2113-2140.

Traykovski, P., Trowbridge, J., and Kineke, G., 2015, Mechanisms of surface wave energy dissipation over a high-concentration sediment suspension: Journal of Geophysical Research: Oceans, 120 p. 1638-1681.

Traykovski, P., Wiberg, P. L., and Geyer, W. R., 2007, Observations and modeling of wave-supported sediment gravity flows on the Po prodelta and comparison to prior observations from the Eel shelf: Continental Shelf Research, v. 27, no. 3-4, p. 375-399.

Walker, N. D., and Hammack, A. B., 2000, Impacts of winter storms on circulation and sediment transport: Atchafalaya-vermilion bay region, Louisiana, USA: Journal of Coastal Research, v. 16, no. 4, p. 996-1010.

Walsh, J. P., and Nittrouer, C. A., 2003, Contrasting styles of off-shelf sediment accumulation in new guinea: Marine Geology, v. 196, no. 3–4, p. 105-125.

Walsh, J. P., Nittrouer, C. A., Palinkas, C. M., Ogston, A. S., Sternberg, R. W., and Brunskill, G. J., 2004, Clinoform mechanics in the Gulf of Papua, New Guinea: Continental Shelf Research, v. 24, no. 19, p. 2487-2510.

Wells, J. T., and Kemp, G. P., 1981, Atchafalaya mud stream and recent mud flat progradation - Louisiana Chenier Plain: Aapg Bulletin-American Association of Petroleum Geologists, v. 65, no. 9, p. 1689-1690.

Wever, T. F., Abegg, F., Fiedler, H. M., Fechner, G., and Stender, I. H., 1998, Shallow gas in the muddy sediments of eckernförde bay, germany: Continental Shelf Research, v. 18, no. 14–15, p. 1715-1739.

Wolinsky, M. A., and Pratson, L. F., 2007, Overpressure and slope stability in prograding clinoforms: Implications for marine morphodynamics: Journal of Geophysical Research: Earth Surface, v. 112, no. F4.

Wright, L. D., 1995, Morphodynamics of inner continental shelves, CRC Press, 241 p.

Wright, L. D., and Friedrichs, C. T., 2006, Gravity-driven sediment transport on continental shelves: A status report: Continental Shelf Research, v. 26, no. 17-18, p. 2092-2107.

Wright, L. D., Friedrichs, C. T., Kim, S. C., and Scully, M. E., 2001, Effects of ambient currents and waves on gravity-driven sediment transport on continental shelves: Marine Geology, v. 175, no. 1–4, p. 25-45.

CHAPTER 3: HYDRODYNAMIC CONTROLS ON MUDDY SEDIMENTARY FABRIC DEVELOPMENT: ATCHAFALAYA CHENIER PLAIN SUBAQUEOUS DELTA

3.1 Introduction

3.1.1 Background

Discoveries regarding the transport of mud in the marine realm over the last ~20 years have highlighted the importance of sediment-gravity flows enhanced by waves and currents as mechanisms for the offshore transport of muddy sediment on continental shelves (e.g., Traykovski et al., 2000; Wright et al., 2001; Friedrichs and Wright, 2004, and others). Appreciation of this mechanism has led to a paradigm shift in our understanding of the dominant processes responsible for the dispersal of muddy sediment and its deposition in shallow marine settings. This new paradigm acknowledges that even on low-gradient shelves (<12m/km) where the development of down-slope sediment gravity flows had been thought impossible, that gravity flows can rapidly transport sediment across-shelf if sufficient current and wave-orbital energies are present (Wright et al., 2001). Flows where the energy needed to initiate the across-shelf transport of muddy sediment are termed "current-wave-enhanced sediment gravity flows", or CWESGFs. In addition to the near-bed currents and/or the orbital motion of surface-gravity waves, CWESGFs require sufficient sediment supply (in the form fluid mud) to transport sediment across-shelf (Figure 3.1). Friedrichs and Scully (2007) described the time-averaged, depth-integrated momentum balance for a current-wave-supported sediment gravity flow as:

$$\alpha g s C \rho_s^{-1} = c_d |u| u_g \qquad (1)$$

where α is the sine of the bed slope; g is the acceleration due to gravity; s is submerged weight of sediment relative to seawater (~1.6 for most terrigenous muds); C is the depth-integrated mass concentration of sediment in suspension (kg/m^2); and ρ_s is sediment density (kg/m^3). On the right-hand side of the equation, bottom stress is governed by the

dimensionless drag coefficient, c_d, the downslope velocity of the gravity current, u_g and; $|u|$, the combined velocity contributions of waves (maximum orbital velocity, u_w, at the top of the wave boundary layer) and currents (u_c), where:

$$|u| = \sqrt{(u_w^2 + u_c^2)} \quad (2)$$

The velocity contributions of gravity, waves, and currents can be represented in dimensionless form as $u_g' = |u_g|/U_{max}$, $u_w' = |u_w|/U_{max}$, and $u_c' = |u_c|/U_{max}$, respectively where U_{max} is the total velocity scale defined as:

$$U_{max} = \sqrt{\left(u_g^2 + u_w^2 + u_c^2\right)} \quad (3)$$

These three contributing velocity terms collectively encompass the resuspension mechanisms for virtually all shelf-sediment transport.

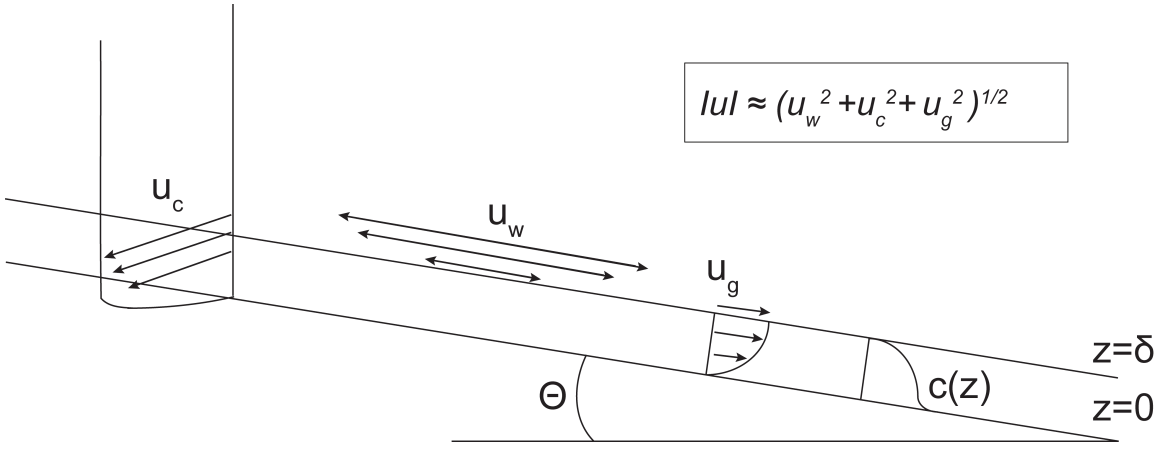

Figure 3.1 Schematic diagram of a CWESGF within a wave boundary layer of thickness δ, moving across a shelf with slope θ. $|u|$ is the velocity scale which accounts for the contribution to quadratic friction of wave orbital velocity (u_w), current velocity (u_c), and the speed of the gravity current (u_g). Modified from Friedrichs and Scully (2007).

Due to the difficulties associated with sampling and imaging fluxes of sediment within the bottom boundary layer, it was not until the initiation of large-scale studies such as the STRATAFORM, S2S MARGINS, and ONR projects that real progress was made towards understanding CWESGF hydrodynamics (Parsons et al., 2009). Observations stemming from these large-scale investigations demonstrated not only that CWESGFs operate in low-gradient settings, but that they actually play a key role in transporting large volumes of mud across-shelf, helping to shape the morphology of the shelf over which they operate (Wright and Friedrichs, 2006).

3.1.2 Identifying CWESGFs in the Rock Record

The recognition that CWESGFs are capable of dispersing muddy sediments across modern low-gradient, energetic shelf systems has important implications for how we interpret fine-grained sediments in the rock record; as it seems likely that this type of sediment gravity flow operated in the ancient past (Bhattacharya and MacEachern, 2009; Macquaker et al., 2010, Plint, 2014; Harazim and McIlroy, 2015). Recognition of the stratigraphic products of these flows within the rock record is challenging because, despite recent advances in hydrodynamic understanding, we do not fully understand how hydrodynamics and bottom boundary layer properties of CWESGFs control sedimentary fabric development.

The work of Macquaker et al. (2010) presents an initial effort towards relating WESGF hydrodynamics (waves and gravity alone) to their stratigraphic products; hypothesizing that the sedimentary product of a WESGF is likely to be normally graded with a three-part internal stratigraphy. This reflects the timing of turbulent and laminar flow developed within a WESGF where: (1) muddy sediment on the middle to inner shelf is resuspended by wave and/or current driven erosion which is followed by (2) the development of a downslope-flowing WESGF within the wave boundary layer after which, (3) the flow wanes and the

eventual collapse of sediment resuspension results in deposition (Figure 3.1). Although this model represents an important first step towards developing recognition criteria for WESGF deposits, it does not address potential fabric modification due to varying combinations of forcing by waves, unidirectional currents, and gravity and in particular it does not consider how varying wave period might affect the sedimentary products of these processes. This study seeks to shed further light on the fundamental mechanisms controlling development of sedimentary fabric in CWESGFs and specifically aims to address the problems of how wave period and local stratigraphic setting might influence the development of the depositional products of this these hybrid flows.

3.1.3 Study Aims and Objectives

The primary aim of this study is to describe additional examples of sediment deposited by CWESGFs, expanding upon the work of Macquaker et al. (2010). Here we describe sediments sampled along a transect of the SW Louisiana (SWLA) Chenier Plain inner shelf with reference to the sedimentary texture, grain origins, sedimentary fabric, and composition, at scales ranging from μm-dm. The SWLA Chenier Plain is an area where CWESGF processes have been well documented (Allison et al., 2000; Rotondo and Bentley, 2003; Draut et al., 2005a Draut et al., 2005b; Kineke et al., 2006; Jaramillo et al., 2009; Denommee and Bentley, 2013; Traykovski et al., 2015). By relating the sedimentary products observed in this study to the documented hydrodynamic processes on the SWLA inner shelf, this work aims to bridge the gap between recent advances in the hydrodynamics of mud transport and the rock record. We also seek to place the documented shelf hydrodynamics and resultant CWESGF fabrics in a semi-quantitative conceptual framework that relates observed sedimentary fabric to the relative contribution of the velocity terms u_g, u_w, and u_c.

3.2 Regional Setting

The SWLA Chenier Plain coast, located ~150km west of the Atchafalaya and Wax Lake Outlets (Figure 3.2) is an ideal locality for investigating the sedimentary products of shallow marine mud dynamics. Within the study area, sediment is sourced from the Atchafalaya River which discharges approximately 8.4 x 10^7 tons/yr of sediment through Atchafalaya Bay and onto the adjacent broad shallow shelf (Allison et al., 2000). The clay- and silt-sized particles, which remain in suspension, are driven seaward onto the inner shelf and transported alongshore by coastal currents as a buoyant plume within the 10 m isobath (Wells and Kemp, 1981). Additional muddy sediment may be delivered to the study area by near-bed fluid mud layers driven by high wave-current energies associated with the episodic passage of winter cold fronts (Kineke et al., 2006). Unlike much of the Louisiana coastline that is retreating rapidly under the influence of eustatic sea level rise, compactional subsidence, and anthropogenic activities such as the extraction of hydrocarbons, the muddy chenier-plain coast is actively accreting (Van Heerden et al., 1981; Wells and Kemp, 1981; Huh et al., 2001; Draut et al., 2005a; Draut et al., 2005b).

Despite being relatively weak (0.1 m/s within the 10 m isobaths), coastal currents play an important role in transporting sediments westward along the shelf (Figure 3.2). Waves, however, are the dominant mechanism responsible for sediment remobilization and across-shelf transport on the subaqueous delta (Allison et al., 2000; Walker and Hammack, 2000; Huh et al., 2001; Jaramillo et al., 2009; Sheremet et al., 2011). The study area is generally influenced by a relatively low wave energy climate, with a mean wave height of 1.5 m and a mean wave period of 4-6 sec (Walker and Hammack, 2000; Kineke et al., 2006).

Sediment accumulation on inner shelf is in the form of a prograding sigmoidal clinothem, with distinct topsets, foresets and bottomsets (Figure 3.2). The gradient on the clinothem increases from <0.1° in the topset region to ~0.5° on the foresets (Denommee and

Bentley, 2013). The morphology of the SLWA shelf is consistent with the "subaqueous-delta-clinoform" (SDC) system as presented by Walsh and Nittrouer (2009). On the SWLA inner shelf, energetic fluid-mud flows that develop primarily in response to increased wave action, transfer sediment seaward to the more steeply dipping foresets. As is the case for other muddy subaqueous-delta-clinothems such as those observed on the Amazon (Nittrouer et al., 1986), Ganges-Brahmaputra (Kuehl et al., 1989; Kuehl et al., 1997), Gulf of Papua (Walsh et al., 2004; Martin et al., 2008), this sediment transfer results in a maximum sediment accumulation rate on the foreset region (4-6 cm yr^{-1} compared to 1-2 cm yr^{-1} on the topsets) where wave-driven bed shear stress is less (Rotondo and Bentley, 2003; Denommee and Bentley, 2013).

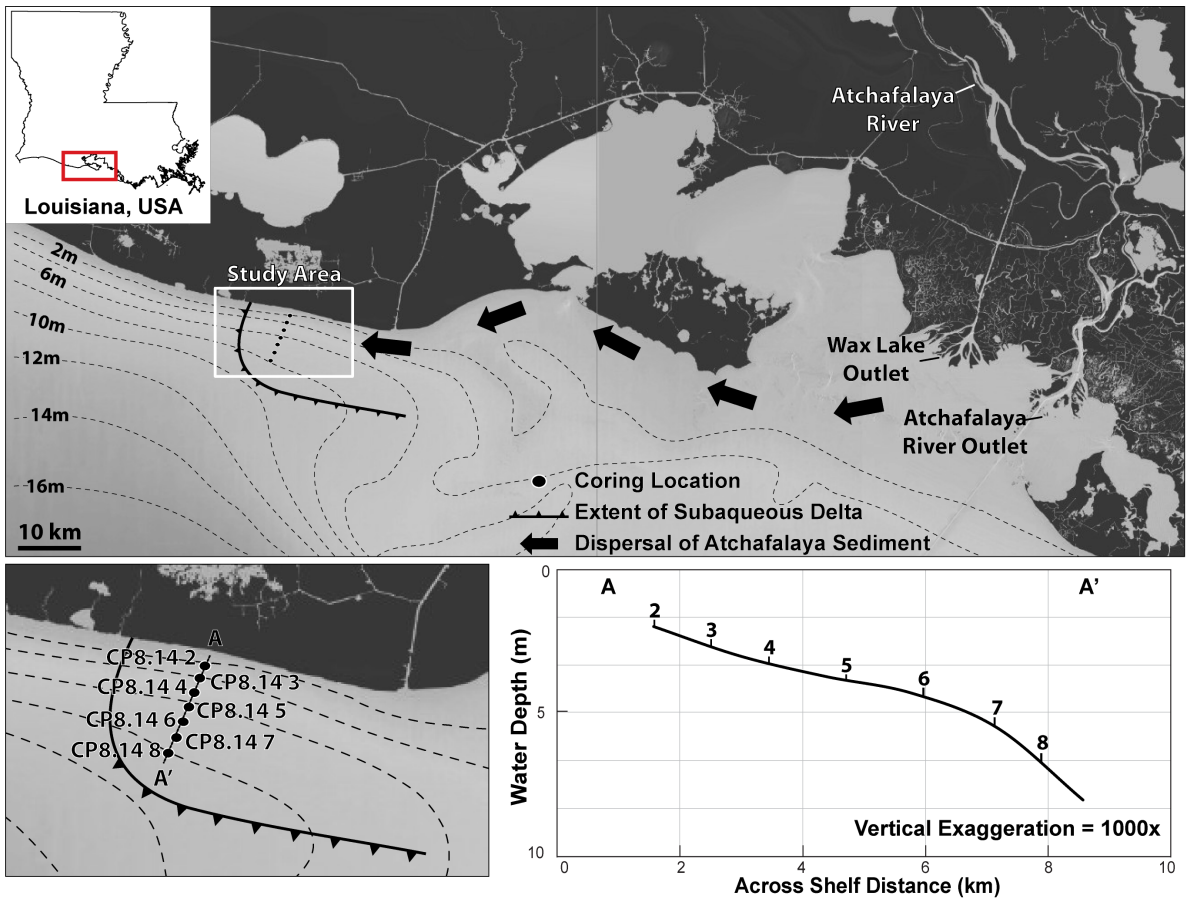

Figure 3.2 Map of the study area including coring locations. Inset at bottom right shows the bathymetric profile A-A' along which sediment cores were collected.

3.3 Materials and methods

3.3.1 Site Selection, Core Collection and Sampling

Coring locations for this study were selected in order to define the cross- shelf, down-slope sediment transport path distribution of sedimentary characteristics (sedimentary texture, grain origin, sedimentary fabric and composition) across the geomorphological elements where CWESGFs are most influential. Multicores were collected from 8 sites along an offshore transect (Figure 3.2) by deploying an Ocean Instruments MC-400 multicorer from the R/V Coastal Profiler in August of 2014. Multicores are relatively short, and collect material from the upper ~40 cm of the seabed. As such they are most useful for studying the dynamic portion of the seabed that is subject to resuspension by physical processes. The use of a multicorer assures minimal sample disturbance during collection, as this coring technique is capable of preserving the delicate sediment-water interface.

For each sampling location three core tubes were sub-sampled for sedimentary fabric analysis (x-radiography and petrography), while one core was sampled for physical property measurements (grain-size and porosity) and $^{210}Pb/^{137}Cs/^{7}Be$ geochronology (addressed separately in Chapter 2 of this dissertation). Subsamples for sedimentary fabric analysis were collected using specialized Plexiglas® X-ray trays designed for insertion directly into multicore tubes, minimizing sample disruption. Samples for physical property measurements and mineralogy were extruded onboard the R/V Coastal Profiler and subsampled at 1 cm intervals for the upper 10 cm of the cores, and at 2 cm intervals thereafter. Samples were placed in air-tight bags and returned to Louisiana State University for analysis.

3.3.2 Sedimentary Fabric Analyses

Sub-samples taken for sedimentary fabric analysis were imaged using a Kodex LTX-1717 X-ray detector panel illuminated by a Min X-ray HF-80 X-ray generator and evaluated

for sedimentary fabric and macrostructures using the image processing program ImageJ® (Schneider et al., 2012). The resulting X-ray image positives reflect variations in bulk density such that light features represent relatively high-density sediments (e.g., quartz), and dark areas represent relatively low bulk density sediments (e.g., clays). This was confirmed by grain-size analyses. Samples from selected X-ray trays were processed to produce petrographic thin sections. sub-samples, 3x5x1cm were extracted from the X-ray trays and then flash-frozen in liquid nitrogen, freeze-dried, and impregnated with low viscosity LR-white resin under partial vacuum conditions, a technique modified after Kuehl et al. (1988) and Bentley and Nittrouer (2003). The impregnated sediment samples were then thin-sectioned and polished to ~ 30μm, so that the samples could be studied under a petrographic microscope. Thin sections prepared using this technique are capable of preserving the internal structures of the sediment. It is possible however, that during the freeze-drying process microcrystals of ice can form. These crystals have a characteristic habit and tend to form an interlocking mosaic making them easy to recognize and exclude from analysis. Crucially, regions that are ice disruption free are easy to identify so lamina geometries can be described. An example of this ice disruption is provided in the results section. Detailed study of sediment composition and sedimentary fabrics was undertaken using a JEOL JSM-6330F Cold Cathode Field Emission Scanning Electron Microscope (SEM) equipped with an Oxford Instruments Aztec Energy Dispersive X-ray System equipped with a silicon drift detector. Images were obtained primarily in backscattered mode utilizing a JEOL solid-state backscatter detector. Imaging conditions were 15 kV and 15mm working distance. Thin sections were prepared for SEM imaging by cleaning lightly with methanol using low lint cloths and air dried, then coating with approximately 40nm of carbon using a Cressington 208 carbon evaporator.

3.3.3 Physical Property Analyses

Sediment porosity was determined by change in mass after oven drying for 24h at 60°C. Grain-size distributions were determined using a Beckman-Coulter LS13 320 laser particle-size analyzer (particle size range of 0.04-2000 μm) after deflocculation in a 0.05% sodium metaphosphate solution, and disaggregation with an ultrasonic probe.

3.4 Results

3.4.1 Sedimentary Texture

The sediments in the shallow seabed remain relatively unconsolidated, with porosities ranging from 80-90% at the sediment water interface and 75-85% at the base of the cores (Figure 3.3). Grain-size distributions as determined by laser particle-size analysis after disaggregation (Figure 3.3) reveal that the bulk of the sediments on the SWLA clinothem are clay- and silt-sized grains. Thin sections and back-scattered electron images from all facies show that a significant portion of the clay-sized material is packaged as intraclastic aggregate grains that range in size from medium-silt to very-fine sand. Two distinct morphologies of aggregate grains are observed. One morphology is spherical and appears to be partially compacted, while the second exhibit a subrounded and elongate “brick-like” morphology, and appear to be more compacted than the surrounding sediments (Figure 3.4). These intraclastic aggregate grains are dominated by clay minerals with some quartz and organic debris (Figure 3.4).

3.4.2 Facies Descriptions

Four dominant facies were identified on the across shelf transected of the subaqueous muddy clinothem. Sedimentary facies were described based on sedimentary texture, primary sedimentary structures and the intensity of biological reworking (using the bioturbation index

of Taylor and Goldring (1993)) as revealed by X-radiographs and thin section photomicrographs.

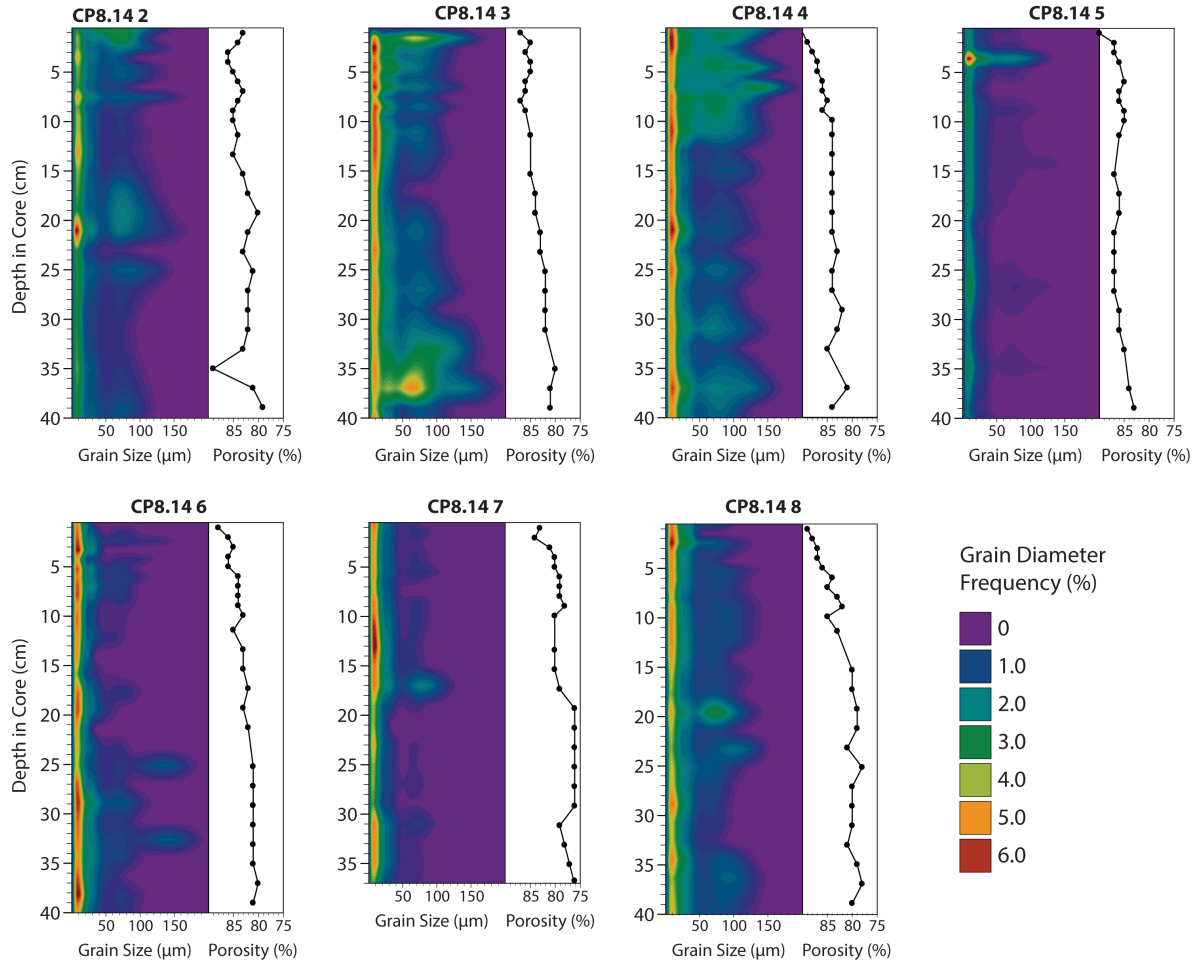

Figure 3.3 Depth profiles of grain diameter percent frequency and porosity for multicores collected on the SWLA clinothem system.

3.4.2.1 Facies 1: Physically Stratified Silts

X-radiographs show that this facies consists of continuous, planar, parallel silt laminae with thicknesses ranging from < 1mm to ~1cm within an apparently homogenous clay-rich matrix (Figure 3.5). Thin section observations reveal that the laminae have sharp basal contacts and are composed primarily of subangular to subrounded silt-sized quartz grains and clay-rich silt-sized round to subrounded intraclastic aggregate grains (Figure 3.6). Minor components include lithic grains, heavy minerals (opaque grains), woody fragments, and glauconite. The mineral component of the muddy matrix is organized into clay mineral-rich,

silt-sized aggregate grains. Sediment reworking in this facies is characteristic of physical processes, however some bioturbation, primarily mm- to cm-long vertical polychaete burrows, is observed within this facies that exhibits a bioturbation index of one (Figure 3.5).

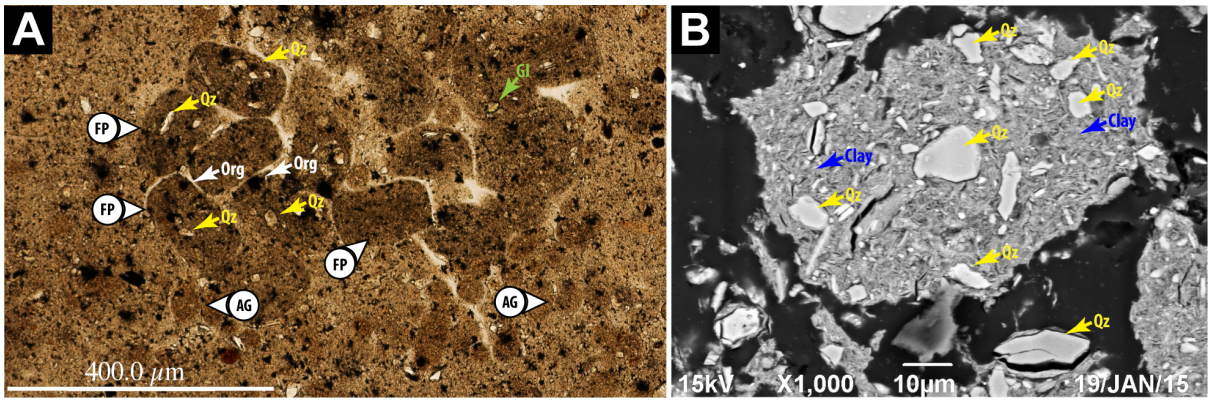

Figure 3.4 Thin section micrograph of pelleted, silt-sized grains within a clay mineral matrix (A). Fecal pellets (FP) are composed of densely packed clay minerals, quartz (Qz) and organic material (Org). Some glauconite (Gl) is also observed in association with the pellets. Aggregate grains (AG) are composed of densely packed clay minerals and organic matter. Backscatter SEM image of a fecal pellet (B).

3.4.2.2 Facies 2: Finely Interbedded Silts and Clays

X-radiograph and thin section observations show that this facies consists of ripple-cross-laminated silts and clays overlain by intercalated planar sub-parallel silt-rich and clay-rich laminae (Figure 3.7). Silt-rich laminae are internally graded and have sharp basal contacts. This facies contains a larger proportion of silt-sized grains than is present in Facies 1. The silt-sized fraction is composed primarily of intraclastic aggregate grains with minor amounts of subangular to subrounded, fine- to medium silt-sized quartz. Minor components include lithic grains, heavy minerals (opaque grains), organic debris/woody fragments, and glauconite. Clay mineral-rich laminae are composed primary of silt-sized aggregate grains (Figure 3.8). Sparse bioturbation, primarily mm- to cm-long vertical polychaete burrows, is observed within this facies that exhibits a bioturbation index of one (Figure 3.7).

3.4.2.3 Facies 3: Faintly Laminated, Normally-Graded Silts and Clays

X-radiograph and thin section observations show that this facies consists of mm-scale silt-rich laminae that are organized into normally-graded beds ranging in thickness from several mm to ~50 mm (Figure 3.9). Although primary sedimentary structures are similar to those observed in facies 2, facies 3 contains a significantly smaller proportion of silt-sized grains. The silt-sized fraction is composed primarily of clay-rich aggregate grains with minor a minor proportion of lithic grains, heavy minerals and organic debris/woody fragments (Figure 3.10). Rare planktonic foraminifera are also observed. The siliceous material that comprised a large portion of the silt-sized fraction in both facies 1 and 2 is notably absent from facies 3. Minor bioturbation, primarily mm- to cm-long vertical polychaete burrows, is observed within this facies that exhibits a bioturbation index of one (Figure 3.9).

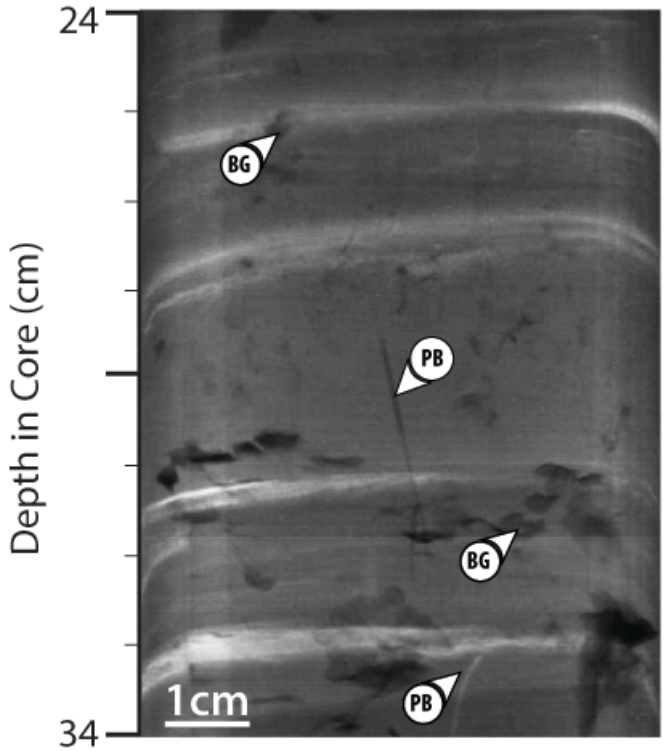

Figure 3.5 X-radiograph negative from Facies 1: physically stratified silts. Station CP8.14 2 displays physically stratified silts (light-coloured laminations) within an apparently homogenous muddy clay-mineral-rich matrix (dark beds). Silt layers display low-angle cross-lamination. Sparse bioturbation is observed within this interval; primarily polychaete burrows (PB). Biogenic gas pockets (BG) are observed.

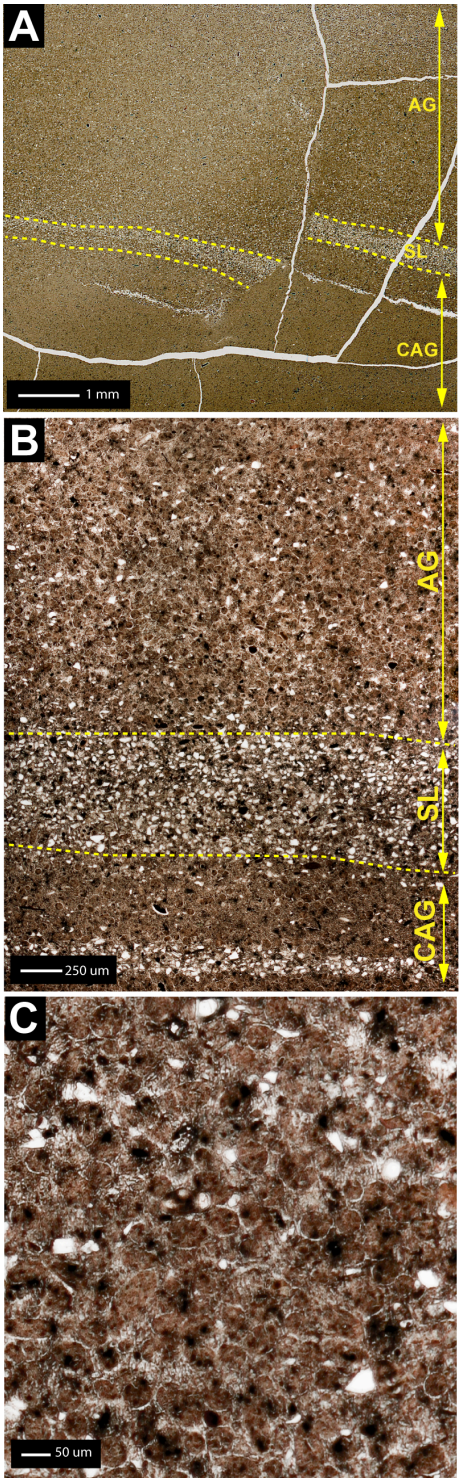

Figure 3.6 Thin section micrograph from Facies 1: physically stratified silts (A). This facies exhibits silt laminae (SL) intercalated with mm-thick units of aggregate grain-dominated laminae (AG), and clay- and aggregate grain-bearing laminae (CAG). Higher-resolution thin section micrograph (B), showing that the silt- and aggregate grain-rich laminae are sharply separated from each other. This higher magnification micrograph (C) shows coarse silt-sized aggregate grains with a minor proportion of poorly rounded, medium silt-sized quartz grains. Note how non-compacted aggregate grains show point contacts and exhibit packing similar to well-rounded, well-sorted mineral grains (see text for discussion).

3.4.2.4 Facies 4: Event Layers with Moderate to High Bioturbation

X-radiograph and thin section observations show that this facies typically consists of relatively thick (~0.20 m) partially homogenized, normally-graded muddy beds (Figure 3.11). Primary sedimentary structures, the most obvious of which are sharp bedding contacts are evident in X-radiographs (Figure 3.11), while grain size analyses reveal that the beds are normally graded (Figure 3.3). Muddy sediments are primarily composed of silt-sized aggregate grains and within a clay-rich matrix (Figure 3.12). Minor components include subangular to subrounded silt-sized quartz, silt-sized lithics, and organic debris/woody fragments. As with facies 3 and 4, rare planktonic foraminifera are also observed. Pervasive bioturbation is evident within this facies; mm- to dm-scale polychaete and burrow remnants are commonly observed. The bioturbation index within this facies is three (Figure 3.11).

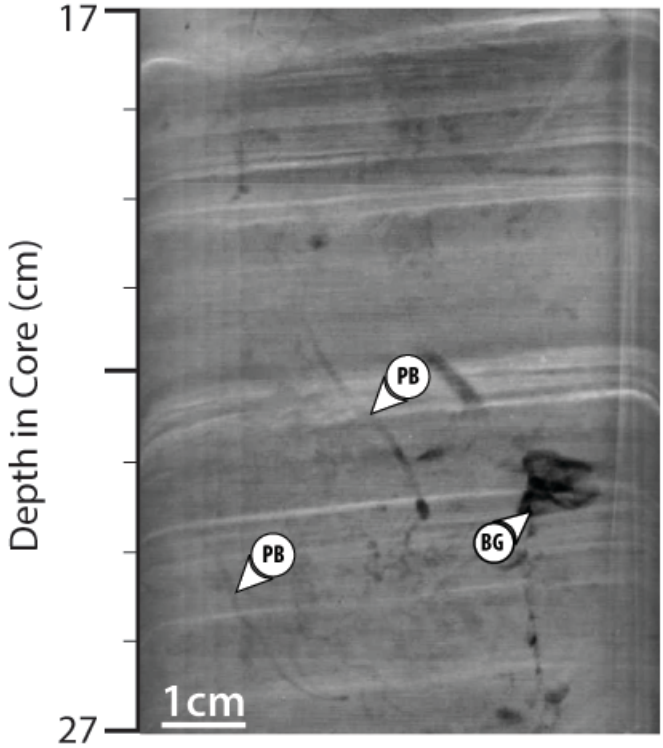

Figure 3.7 X-radiograph negative from Facies 2: finely interbedded clays and silts. Station CP8.14 3 displays silts (light-coloured laminations) interbedded with clay minerals (dark beds). Minor bioturbation is observed within this interval; primarily polychaete burrows (PB). Biogenic gas pockets (BG) are observed.

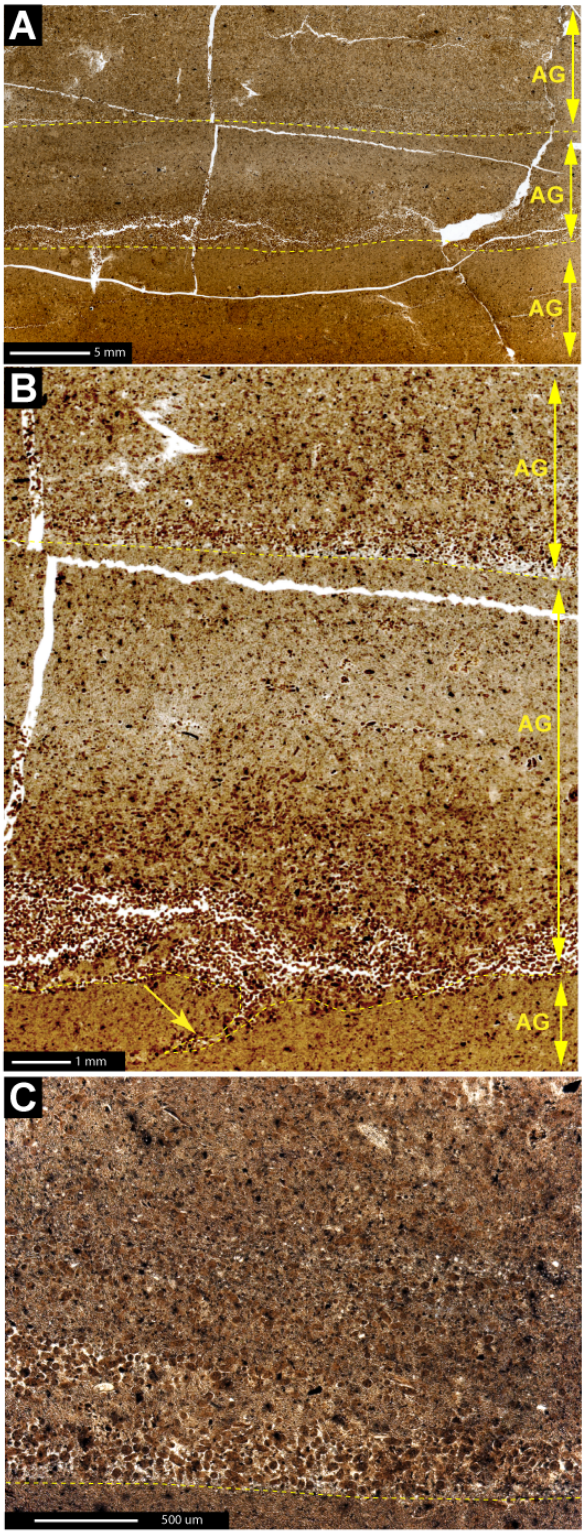

Figure 3.8 Thin section micrograph from Facies 2: finely interbedded clays and silts. This facies exhibits a stacked succession of thin beds with erosive bases (A). The basal portion of each bed is composed of an up-ward fining layer of mineral aggregate grains (AG). Bedding contacts of beds with aggregate grains show occasionally bioturbated bases (B; yellow arrow). A sharp decrease in aggregate grain density occurs vertically throughout the bed. Part (C) shows aggregate grains close to the base. These aggregate grains most likely were transported most likely as bedload.

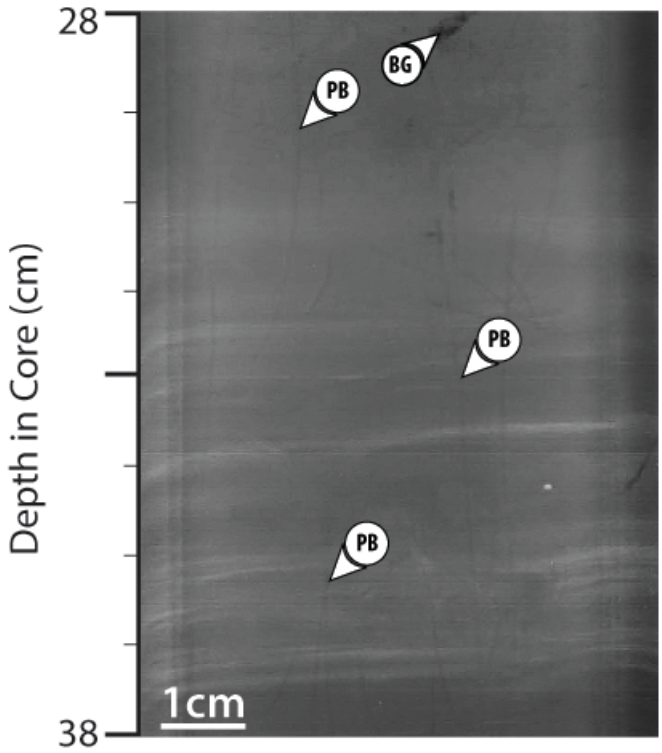

Figure 3.9 X-radiograph negative from Facies 3: faintly laminated, normally-graded silts and clays. Station CP8.14 6 displays thin silt laminae with some evidence of normal grading (light-colored laminations) within an apparently homogenous muddy, clay-mineral-rich matrix (dark beds). Moderate bioturbation is observed within this interval; primarily polychaete burrows (PB).

3.4.3 Across-Shelf Spatial Distribution of Facies

Whereas individual facies are recognized across the clinothem, their spatial distribution varies across the inner-shelf (Figure 3.13). The inner-topsets of the clinothem are dominated by facies 1 and 2, physically stratified silts and finely interbedded silts and clays. Facies 1 is primarily observed in the most proximal regions of the clinothem, whereas facies 2 becomes more prominent 3-4 km landward of the rollover point at a water depth of ~3-4 m. Moving across shelf towards the outer topsets a major facies change is observed as the interbedded siliceous silts and clays of facies 2 are gradually replaced by the faintly laminated, normally graded silts-sized clay aggregates that are characteristic of facies 3. Near the rollover point at ~6 m water depth, gas pockets are observed within the sediment. Both near the rollover and on the foresets another major facies change is observed because here, the relatively thick,

sharp-based, normally graded, moderately bioturbated “event-type” beds of facies 4 become the most dominant facies type observed on the clinothem.

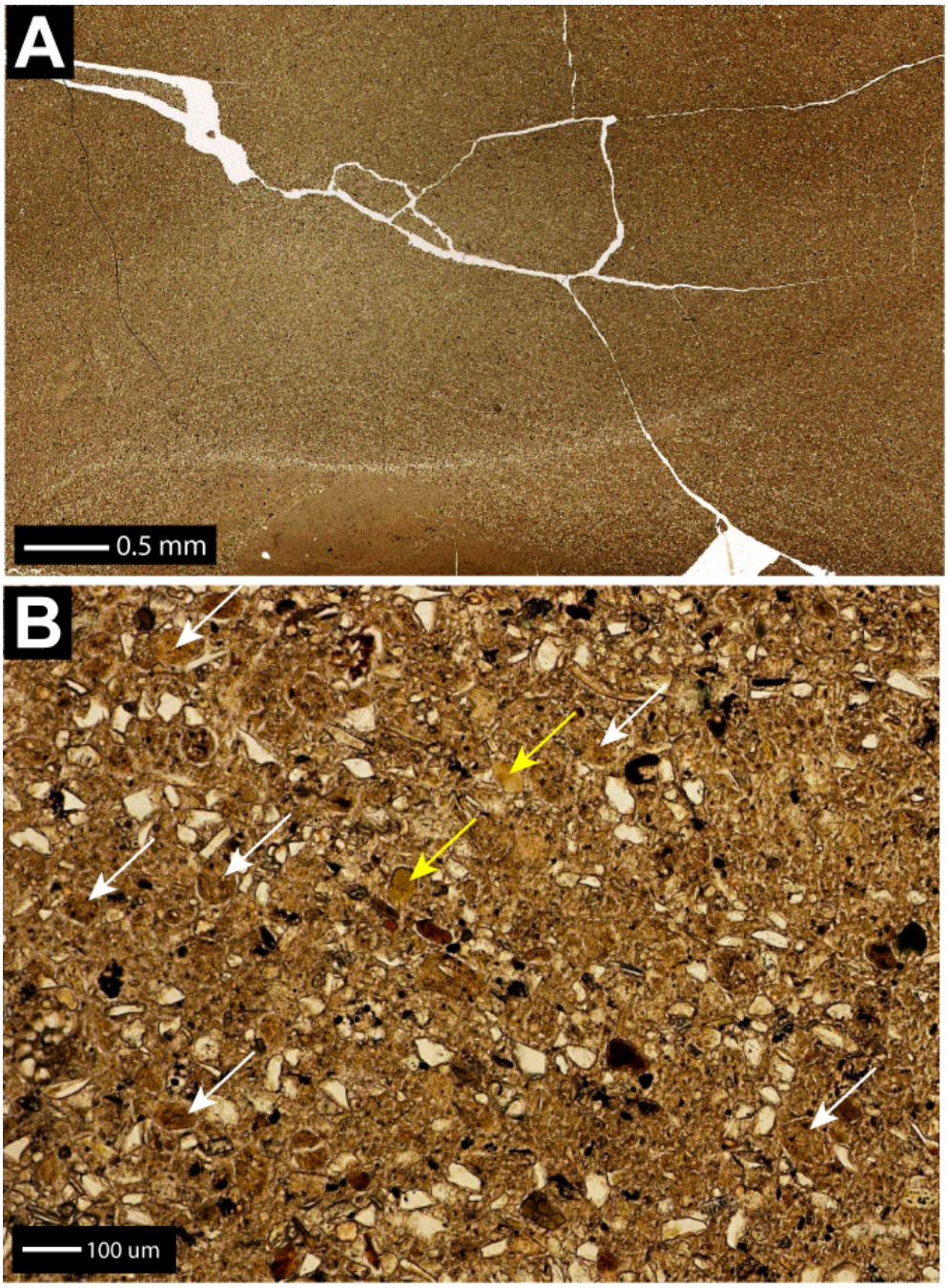

Figure 3.10 Thin section micrograph of Facies 3: faintly laminated, normally-graded silts and clays. This thin section scan shows wavy-discontinuous silt stringer in a well-bioturbated, clay-rich matrix. This thin section micrograph (B) shows a poorly-sorted grain assemblage composed of fine- to coarse-silt sized quartz grains, together with rare aggregate grains (white arrows). In these facies accessory minerals including glauconite (yellow arrows) and opaque minerals (iron oxides?) are present as well.

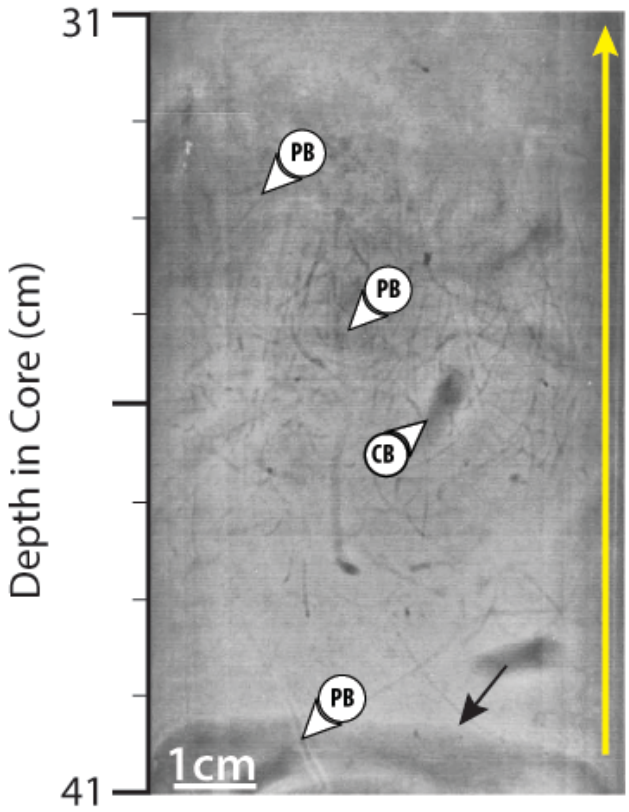

Figure 3.11 X-radiograph negative from Facies 4: event layers with moderate to high bioturbation. Station CP8.14 8 shows a relatively thick (~20cm), sharp-based (black arrow) partially homogenized, normally-graded muddy tempestite (yellow arrow). Evidence of intense bioturbation is observed, primarily polychaete (PB) and crustacean (CB) burrows. Burrows show complex cross-cutting relationships.

3.5 Discussion

3.5.1 Origin and Significance of Intraclastic Aggregate Grains

Sediments on the inner shelf are primarily composed of intraclastic clay-mineral aggregate grains with minor amounts of siliceous silt and other accessory minerals. Two distinct morphologies of intraclastic aggregate grains are observed (Figure 3.4). The first, described as having a "brick-like" morphology are likely benthic fecal pellets, produced by sediment-ingesting organisms (e.g., polychaetes) at the sediment water interface (Needham et al., 2006). This interpretation is supported by the fact that these intraclastic aggregates appear to be composed of the compacted material that is compositionally similar to the surrounding, uncompacted sediment (Figure 3.4). The second morphology of intraclastic aggregate grains is nearly spherical, and smaller than the aggregate grains interpreted as being fecal pellets.

There are two probable origins for this second morphology. They may be reworked benthic fecal pellets, or alternatively they may have formed during storm-reworking that repackaged cohesive clay-sized grains into the larger aggregate grains (e.g., Schieber et al., 2010).

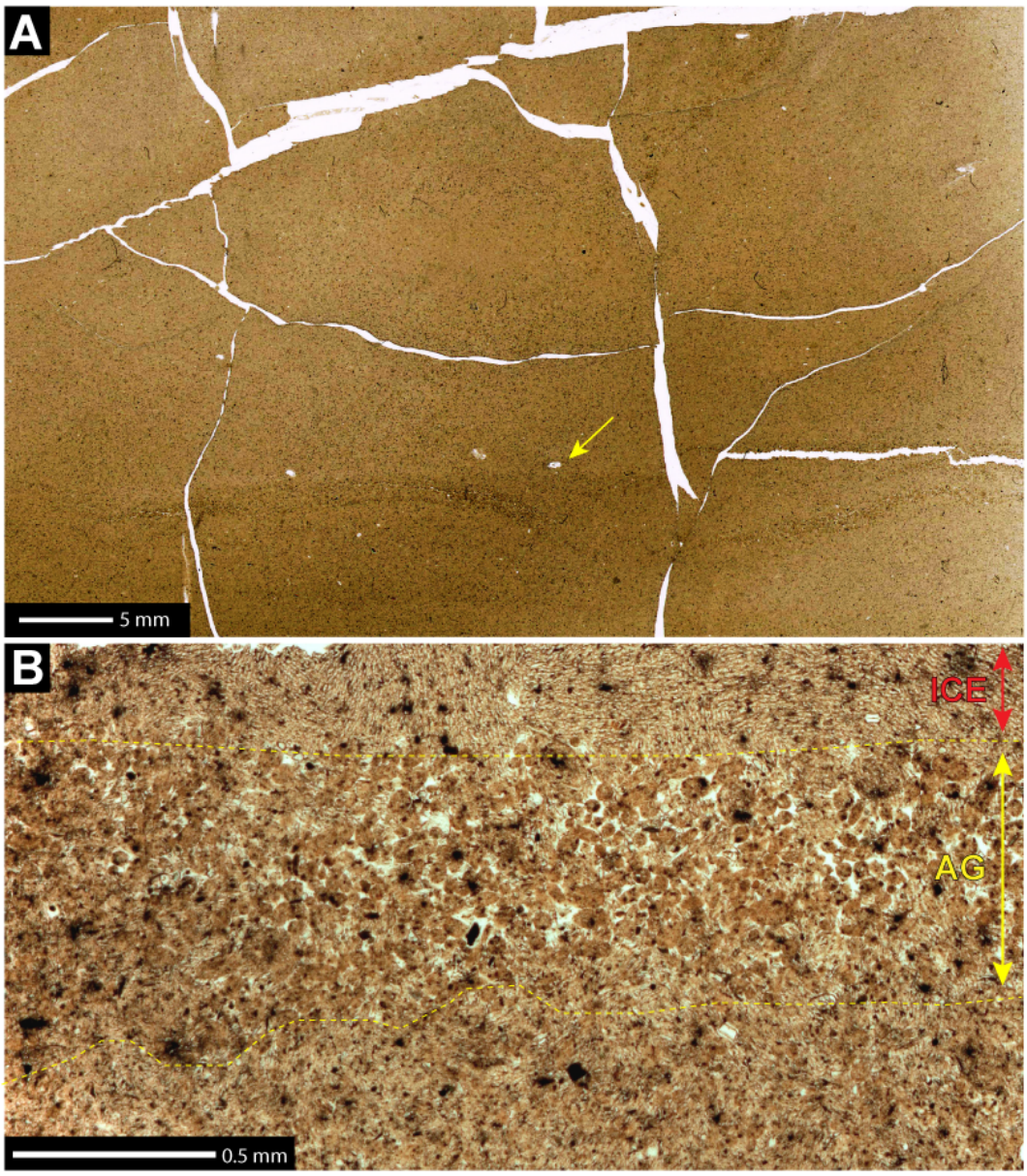

Figure 3.12 Thin section micrograph from Facies 4: event layers with moderate to high bioturbation (transmitted light). This low magnification thin section scan shows wavy-discontinuous lenses of aggregate grains that not conform to bases of beds or other erosional fabric (A). Occasionally skeletal fragments are visible (yellow arrow). This close-up image of a wavy discontinuous lens, showing a poorly sorted assemblage of aggregate grains that contain both round and subrounded grains (B). This image also contains sedimentary fabric that has been disrupted by the formation of ice crystals during the thin section preparation process (area indicated by the red arrow).

The significance of these intraclastic aggregate grains however, lies not in their origin, but rather in that they can be transported as part of the bedload and hydrodynamically sorted (Plint and Macquaker, 2013). Aggregate grains provide the grain size-and density contrasts, which are necessary for the development of observable microfabrics in the muddy sediments on the inner shelf where only a very small fraction of the silt-sized material is siliceous. It is also important to note that the effective grain-size of sediments on the SWLA Chenier Plain shelf is inconsistent with the disaggregated grain-size distributions.

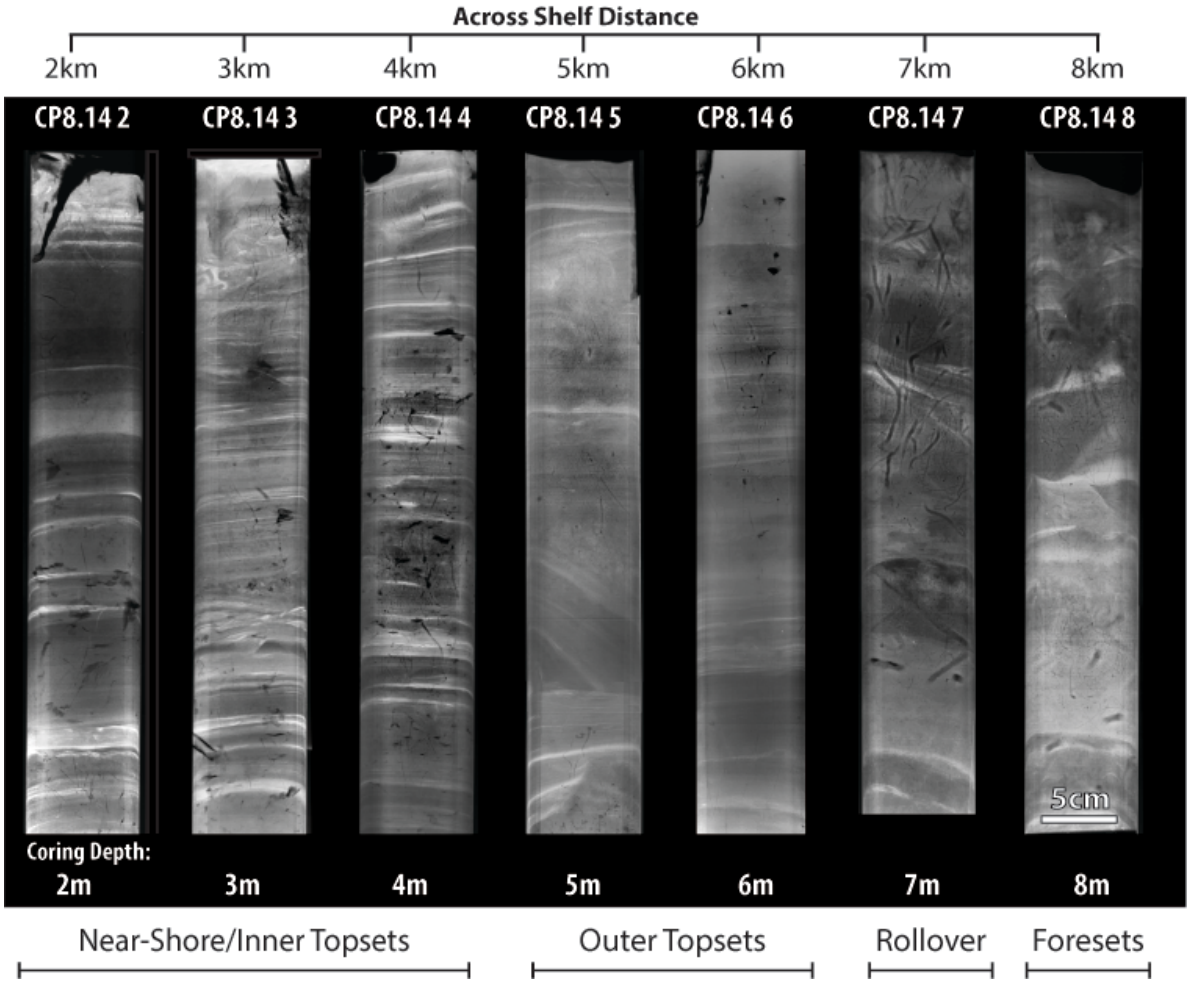

Figure 3.13 Across-shelf transects of sediment cores collected from the SWLA Chenier Plain showing facies variability. Cores correspond to sampling locations indicated in Figure 2. Sampling locations are spaced 1km apart, with sampling location CP8.14 2 located in ~2m of water, CP8.14 3 located in ~3m of water, etc.

3.5.2 Across-Shelf Sedimentary Fabric Development

The primary mechanisms by which sediment is transported across-shelf and deposited differ across the clinothem elements examined in this study (topset, rollover, and foresets). As a result, the sedimentary facies and microfabrics observed on each of the clinothem elements provides information that can be used to construct diagnostic recognition criteria for the specific type of muddy sediment gravity-flow that is responsible for their deposition.

3.5.2.1 Clinothem Topsets

Current-wave-enhanced-sediment-gravity flows are documented as being one of the key mechanisms by which muddy sediments are transported across the SWLA inner shelf (Kineke et al., 2006; Jaramillo et al., 2009; Sheremet et al., 2011). These flows have a distinct three-phase evolution that is expected to result in a tripartite internal stratigraphy reflective of both the turbulent and laminar components of the three temporally discrete phases of the flow (Figure 3.1) (Macquaker et al., 2010). The sedimentary facies and microstructures which are most characteristic of the topset region (i.e., facies 2), where water depths range from ~3-4 m, exhibit a motif that is broadly consistent with the flow evolution of a CWESGF. Here we observe: (1) ripple cross-laminated silts and clays overlying an erosion surface; (2) a poorly-developed wavy-parallel lamina set composed of intercalated silt- and clay-rich laminae overlain by; (3) a normally graded drape that was probably deposited as the flow waned (Figures 3.7 and 3.8).

3.5.2.2 Clinothem Rollover

Towards the outer region of the clinothem topsets (clinothem rollover) in water depths of ~3-5m, there is a transition into a facies 3. Facies 2 and 3 are not entirely dissimilar and are probably both the products of CWESGF-dominated sediment dispersal mechanisms. As

compared to facies 2, which is prevalent on the inner portion of the topsets, facies 3 exhibits a narrower range of grain-size distribution (Figure 3.3, CP8.14 5). The narrow range of the grain-size distribution near the clinothem rollover suggests that the larger, denser grains were not transported further offshore by CWESGFs, presumably because the wave-induced turbulence was insufficient to maintain siliceous silt and large intraclastic aggregate grains in suspension. Sedimentary facies near the clinothem rollover show overprinting by the development of biogenic gas within the sediment (Figure 3.13, CP8.14 5), consistent with the rapid deposition of fine-grained sediments and the rapid burial of organic matter with the inevitable production of biogenic gas.

3.5.2.3 Foresets – Episodic Sedimentation

The sedimentary fabric of the foresets (facies 4) is distinct from the topsets and at the clinothem rollover and probably represents the episodic input of sediment from the topset region by a combination of CWESGFs and tempestites (Denommee and Bentley, 2013). Tempestites on the SWLA inner shelf are likely triggered by large storm waves (e.g., waves generated during a strong tropical cyclone). The reappearance of silt-sized siliceous grains on the clinothem foresets (facies 4) suggests that these grains were transported offshore by a mechanism with more energy than a CWESGF (e.g., temptestites) that enabled siliceous silt and large intraclastic aggregate grains to remain in suspension.

3.5.3 CWESGF Fabric Development: the Importance of Wave Period

Although broadly consistent with the sedimentary fabric predicted by Macquaker et al. (2010) we observe subtle variations in the microfabrics deposited by CWESGFs on the topsets of the SWLA inner shelf clinothem. Specifically, we observe a thinner, more inhibited intercalated lamina set as compared that described from the Eel Shelf, Northern

California. On the SWLA inner shelf, the dominant wave periods (4-6 sec) during which CWESGFs are most likely to develop (Jaramillo et al., 2009) could potentially inhibit the deposition of the intercalated wavy-parallel lamina on the SWLA shelf relative to the Eel shelf where the dominant wave period is significantly longer (10-12 sec) (Bentley and Nittrouer, 2003; Traykovski et al., 2007). On the SWLA inner shelf, the inhibition of a well-developed intercalated layer can be attributed to rapid, short-term shifts from laminar to turbulent flow conditions that occur frequently within the study area in response to temporal variations in wave-energy caused by the short wave period (4-6 sec).

From computational simulations of wave resuspension in fluid mud, Ozdemir et al., (2011) demonstrate that temporal variations in wave energy on timescales of wave period to wave group period, cause short-term shifts from laminar flow conditions, to turbulent flow, and back to laminar. Such short-term oscillations could potentially add complexity to bedding patterns, and offer a potential mechanism to explain some of the fabric differences evident between the Eel Shelf (long period waves >10s), and the SWLA shelf (much shorter wave periods, <5 s, and shorter group periods).

3.5.4 Recognition of Diagnostic CWESGF Sedimentary Fabrics

Variations in the sedimentary fabric should reflect the interaction between the three contributing velocity terms that outline the forcing responsible for CWESGF development: u_g', u_w', and u_c' (Figure 3.1) as well as the wave period. Because of this, the facies and microstructures deposited by CWESGFs should display subtle, but diagnostic variations. An ideal CWESGF deposit will record the following flow events: (1) basal erosion; (2) turbulent traction transport; (3) laminar sediment gravity flow; and (4) suspension settling from waning flow (Macquaker et al., 2010). A modern example of the sedimentary microstructures produced by the evolution of an ideal CWESGF on the Eel Shelf, Northern California is

discussed by Macquaker et al. (2010). A more variable and complicated phasing of CWESGF conditions should leave a sedimentary record of formative conditions.

Variations in the relative contributions of the velocity terms (u_g', u_w', and u_c') responsible for CWESGF development can be illustrated using a prismatic ternary diagram (Figure 3.14) where current-, wave-, and gravity-dominated end members form the vertices of a triangle, and wave period forms the prism axis. In this framework, forcing processes can be represented quantitatively, based on wave period and the terms of Eq. 3, which define the relative contribution of each of the velocity terms u_g', u_w', and u_c'. This framework can then be used to explore relationships among hydrodynamics and CWESGF sedimentary fabrics.

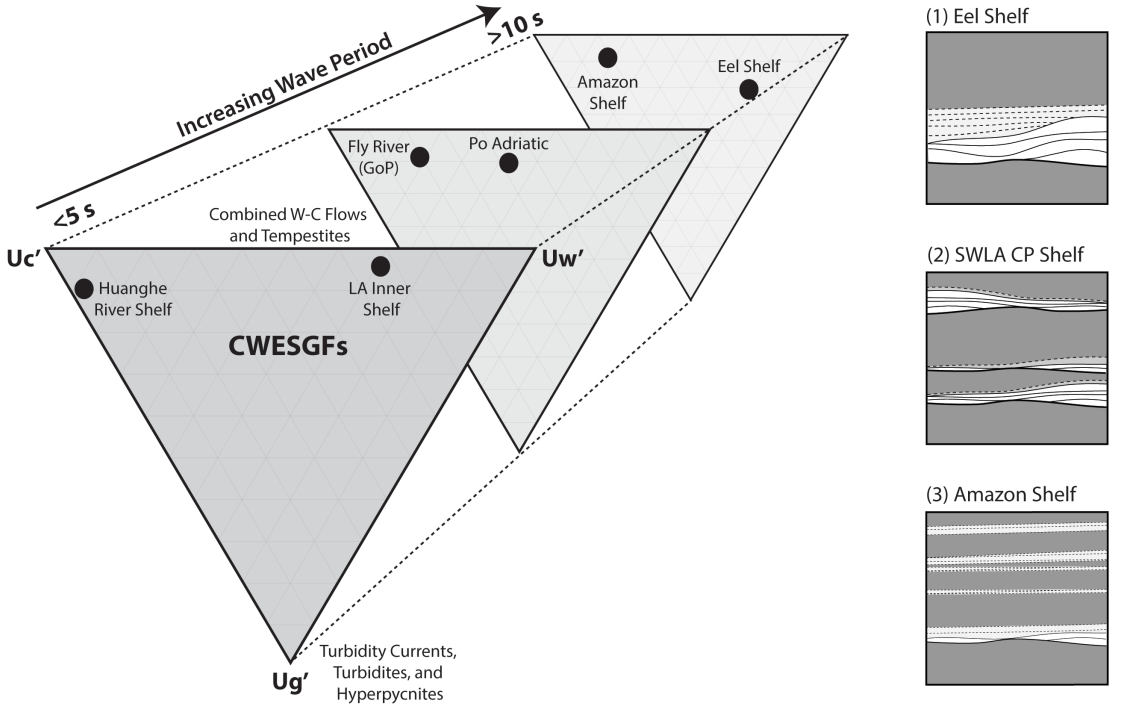

Figure 3.14 Diagram representing the potential spectrum of CWESGF fabrics. Locations where CWESGFs have been documented have been quantitatively plotted on this diagram by determining the relative contributions of each of the velocity terms contributing to the development of CWESGFs as well as the dominant wave period: SWLA (Wright et al., 2001); Eel Shelf (Wright et al., 2001); Huanghe River Delta (Wright et al., 2001); Po River Delta (Traykovski et al., 2007; Fain et al., 2005); Amazon River Delta (Curtin et al., 1986; Kuehl et al., 1988); and the Fly River Delta (Walsh et al., 2004; Martin et al., 2008) . Conceptualized diagrams of the sedimentary products of these environments are included for selected locations.

On the SWLA inner shelf where wave orbital velocity (u_w') is the dominant driving energy and the wave period is relatively short (<5s). Sedimentary facies and microfabrics are observed to be consistent with the flow evolution of the CWESGF: (1) the erosion of the underlying muddy substrate in response to currents which were initially strong enough to erode the underlying muddy substrate, followed by (2) the deposition of ripple a crossbeded unit during subsequent wave-mediated oscillatory motions in low-viscosity suspension (Figure 3.7); followed by (3) the deposition of subtle intercalated laminae during laminar flow occurring at higher suspended sediment concentrations; overlain by (4) normally graded sediments deposited during the waning phases of the flow.

Sediments deposited by CWESGFs where u_c' is the dominant driving energy and where there is little oscillatory motion, such as is the case on the Amazon shelf (e.g., Kuehl et al., 1988; Cacchione et al., 1995; Kineke and Sternberg, 1995; Kineke et al., 1996), or the Waiapu Shelf of New Zealand (Ma et al., 2008; Ma et al., 2010) are hypothesized to show less evidence of short-period laminar shifts. These flows probably produce a single genetic bed with little if any evidence of bidirectional flow (Figure 3.14).

This analytical approach (observed sedimentary fabric with measured hydrodynamic conditions represented in Figure 3.14) provides a quantitative framework by which relationships among CWESGF formative conditions and fabric recognition criteria may be further studied in the future. For example, in Figure 3.14, the clustering of all examples plotted (Eel, Po, Huanghe, SWLA, and Fly; see caption for data sources) close to the u_w' - u_c' axis highlights the relatively gentle downslope velocity component, compared to resuspension energy from waves and currents. It also provides a framework which can be used to compared sedimentary fabrics.

3.5.5 Preservation Potential of CWESGF Sedimentary Fabrics

Modern analogues for muddy sediment deposition such as the SWLA inner shelf are only relevant to the study of ancient sedimentary systems only if we can recognize their products in the rock record. This requires that the sediments can avoid bioturbation and preserve primary depositional fabric (Bentley and Nittrouer, 2003). The preservation potential for any muddy, marine sedimentary deposit is dependent on the rate of bioturbation and the burial rate, with episodic (event) sedimentation being especially important for preservation (Bentley et al., 2006). Numerical models developed by Bentley et al. (2006) show that the preservation potential of sedimentary fabrics with respect to overprinting by bioturbation rises substantially as sedimentation rates increase beyond 2cm/yr. Given that the sedimentation rates on the SWLA inner shelf commonly exceed 2cm/yr (Denommee and Bentley, 2013) there is a good chance that primary sedimentary fabrics generated by CWESGFs will be incorporated into the sedimentary record.

3.6 Conclusions

1. Observations indicate that the production of intraclastic aggregate grains either as benthic fecal pellets or through storm reworking of previously deposited sediments plays an important role in the development of the facies and microstratigraphy that is produced on the SWLA inner shelf. These aggregate grains comprise a significant fraction of the silt-size grains (i.e., potential bedload) on the shelf, where there is little detrital (siliceous) silt input. Most importantly, intraclastic aggregate grains provide the grain-size and density contrasts required for the development of observable CWESGFs microstratigraphy on the inner shelf.

2. We consider wave period to be important in influencing sedimentary fabric development because it constrains the time available for laminar flow conditions to evolve, especially

when waves are the dominant mechanism responsible for the initiation of a CWESGF, such as is the case on the SWLA inner shelf. The longer the wave period, the more fully developed the laminar sediment gravity flow component of the CWESGF fabric may be, associated with thicker, less complex bedding patterns.

3. The relative contribution of each of the velocity terms u_c, u_g, and u_w exerts a strong control on the sedimentary fabric development. The analytical approach presented here (observed fabric, and measured hydrodynamic conditions represented in Figure 3.14) provides a quantitative framework by which relationships among CWESGF formative conditions (i.e., u_c, u_g, and u_w) and fabric recognition criteria may be further studied in the future.

3.7 Acknowledgements

This work was supported through the Billy and Anne Harrison endowment awarded to SJB as well as student research grants (AAPG, SEPM, GSA, and GCAGS) awarded to KCD. The authors would like to thank the LSU Coastal Studies Institute field support unit, Dr. Jillian Maloney (UCSD), and Jeff Obelcz (LSU DOCS) for their help with sample collection. Wanda LeBlanc is thanked for her help sample preparation and analysis, and Rick Young is thanked for his help with thin section impregnation.

3.8 References

Allison, M.A., Kineke, G.C., Gordon, E.S., Goni, M.A., 2000. Development and reworking of a seasonal flood deposit on the inner continental shelf off the Atchafalaya River. Continental Shelf Research 20, 2267-2294.

Bentley, S.J., Nittrouer, C.A., 2003. Emplacement, modification, and preservation of event strata on a flood-dominated continental shelf: Eel shelf, Northern California. Continental Shelf Research 23, 1465-1493.

Bhattacharya, J.P., MacEachern, J.A., 2009. Hyperpycnal rivers and prodeltaic shelves in the Cretaceous Seaway of North America. Journal of Sedimentary Research 79, 184-209.

Cacchione, D. A., Drake, D. E., Kayen, R. W., Sternberg, R. W., Kineke, G. C., and Tate, G. B., 1995, Measurements in the bottom boundary-layer on the Amazon Subaqueous Delta. Marine Geology 125, 235-257.

Curtin, T. B., 1986, Physical observations in the plume region of the Amazon River during peak discharge—II. Water masses. Continental Shelf Research 6, 53-71.

Denommee, K.C., Bentley, S.J., 2013. Influence of mass-transport processes on clinoform mechanics on the Southwest Louisiana Shelf. GCAGS Transactions 63, 205-212.

Draut, A.E., Kineke, G.C., Huh, O.K., Grymes, J.M., Westphal, K.A., Moeller, C.C., 2005a. Coastal mudflat accretion under energetic conditions, Louisiana chenier-plain coast, USA. Marine Geology 214, 27-47.

Draut, A.E., Kineke, G.C., Velasco, D.W., Allison, M.A., Prime, R.J., 2005b. Influence of the Atchafalaya River on recent evolution of the chenier-plain inner continental shelf, northern Gulf of Mexico. Continental Shelf Research 25, 91-112.

Friedrichs, C.T., Wright, L.D., 2004. Gravity-driven sediment transport on the continental shelf: Implications for equilibrium profiles near river mouths. Coastal Engineering 51, 795-811.

Fain, A. M. V., Ogston, A. S., and Sternberg, R. W., 2007, Sediment transport event analysis on the western Adriatic continental shelf. Continental Shelf Research 27, 431-451.

Friedrichs, C.T., Scully, M.E., 2007. Modeling deposition by wave-supported gravity flows on the Po River prodelta: from seasonal floods to prograding clinoforms. Continental Shelf Research 27, 322-337.

Harazim, D., McIlroy, D., 2015. Mud-rich density-driven flows along an Early Ordovician storm-dominated shoreline: implications for shallow-marine facies models. Journal of Sedimentary Research 85, 509-528.

Huh, O.K., Walker, N.D., Moeller, C., 2001. Sedimentation along the eastern Chenier Plain coast: down drift impact of a delta complex shift. Journal of Coastal Research 17, 72-81.

Jaramillo, S., Sheremet, A., Allison, M.A., Reed, A.H., Holland, K.T., 2009. Wave-mud interactions over the muddy Atchafalaya subaqueous clinoform, Louisiana, United States: wave-supported sediment transport. Journal of Geophysical Research: Oceans 114, C04002.

Kineke, G. C., and Sternberg, R. W., 1995, Distribution of fluid muds on the Amazon continental-shelf. Marine Geology 125, 193-233.

Kineke, G.C., Sternberg, R.W., Trowbridge, J.H., Geyer, W.R., 1996. Fluid-mud processes on the Amazon continental shelf. Continental Shelf Research 16, 667-696.

Kineke, G.C., Higgins, E.E., Hart, K., Velasco, D., 2006. Fine-sediment transport associated with cold-front passages on the shallow shelf, Gulf of Mexico. Continental Shelf Research 26, 2073-2091.

Kuehl, S.A., Nittrouer, C.A., Demaster, D.J., 1988. Microfabric study of fine-grained sediments - observations from the Amazon subaqueous delta. Journal of Sedimentary Petrology 58, 12-23.

Kuehl, S.A., Hariu, T.M., Moore, W.S., 1989. Shelf sedimentation off the Ganges-Brahmaputra river system - evidence for sediment bypassing to the Bengal Fan. Geology 17, 1132-1135.

Kuehl, S.A., Levy, B.M., Moore, W.S., Allison, M.A., 1997. Subaqueous delta of the Ganges-Brahmaputra river system. Marine Geology 144, 81-96.

Ma, Y., Wright, L. D., and Friedrichs, C. T., 2008, Observations of sediment transport on the continental shelf off the mouth of the Waiapu River, New Zealand: Evidence for current-supported gravity flows. Continental Shelf Research 28, 516-532.

Ma, Y., Friedrichs, C. T., Harris, C. K., and Wright, L. D., 2010, Deposition by seasonal wave- and current-supported sediment gravity flows interacting with spatially varying bathymetry: Waiapu shelf, New Zealand. Marine Geology 275, 199-211.

Macquaker, J.H.S., Bentley, S.J., Bohacs, K.M., 2010. Wave-enhanced sediment-gravity flows and mud dispersal across continental shelves: reappraising sediment transport processes operating in ancient mudstone successions. Geology 38, 947-950.

Martin, D. P., Nittrouer, C. A., Ogston, A. S., and Crockett, J. S., 2008, Tidal and seasonal dynamics of a muddy inner shelf environment, Gulf of Papua. Journal of Geophysical Research. Earth Surface 113, F01S07.

Needham, S.J., Worden, R.H., and Cuadros, J., 2006. Sediment ingestion by worms and the production of bio-clays: A study of macrobiologically enhanced weathering and early diagenetic processes. Sedimentology 53, 1365-3091.

Nittrouer, C.A., Kuehl, S.A., Demaster, D.J., Kowsmann, R.O., 1986. The deltaic nature of Amazon shelf sedimentation. Geological Society of America Bulletin 97, 444-458.

Ozdemir, C.E., Hsu, T.-J., Balachandar, S., 2011. A numerical investigation of lutocline dynamics and saturation of fine sediment in the oscillatory boundary layer. Journal of Geophysical Research: Oceans, 116.

Parsons, J.D., Friedrichs, C.T., Traykovski, P.A., Mohrig, D., Imran, J., Syvitski, J.P.M., Parker, G., Puig, P., Buttles, J.L., García, M.H., 2009. The mechanics of marine sediment gravity flows, continental margin sedimentation. Blackwell Publishing Ltd., pp. 275-337.

Plint, A.G., Macquaker, J.H.S., 2013. Bedload transport of mud across a wide, storm-influenced ramp: Cenomanian-Turonian Kaskapau Formation, Western Canada foreland basin. Journal of Sedimentary Research 83, 1200-1201.

Plint, A. G., 2014, Mud dispersal across a Cretaceous prodelta: storm-generated, wave-enhanced sediment gravity flows inferred from mudstone microtexture and microfacies. Sedimentology 61, 609-647.

Rotondo, K., Bentley, S.J., 2003. Deposition and resuspension of fluid mud on the Western Louisiana inner shelf. Gulf Coast Association of Geological Societies Transactions 53, 722-731.

Schieber, J., Southard, J.B., and Schimmelmann, A., 2010, Lenticular shale fabrics resulting from intermittent erosion of muddy sediments – comparing observations from flume experiments to the rock record. Journal of Sedimentary Research 80, p. 119-128.

Schneider, C.A., Rasband, W.S., Eliceiri, K.W., 2012. NIH Image to ImageJ: 25 years of image analysis. Nat Meth 9, 671-675.

Sheremet, A., Jaramillo, S., Su, S.F., Allison, M.A., Holland, K.T., 2011. Wave-mud interaction over the muddy Atchafalaya subaqueous clinoform, Louisiana, United States: Wave processes. Journal of Geophysical Research-Oceans, 116.

Slingerland, R., Driscoll, N. W., Milliman, J. D., Miller, S. R., and Johnstone, E. A., 2008, Anatomy and growth of a Holocene clinothem in the Gulf of Papua: Journal of Geophysical Research: Earth Surface 113, pp.

Taylor, A.M., Goldring, R., 1993. Description and analysis of bioturbation and ichnofabric. Journal of the Geological Society 150, 141-148.

Traykovski, P., Geyer, W.R., Irish, J.D., Lynch, J.F., 2000. The role of wave-induced density-driven fluid mud flows for cross-shelf transport on the Eel River continental shelf. Continental Shelf Research 20, 2113-2140.

Traykovski, P., Wiberg, P. L., and Geyer, W. R., 2007, Observations and modeling of wave-supported sediment gravity flows on the Po prodelta and comparison to prior observations from the Eel shelf. Continental Shelf Research 27, 375-399.

Traykovski, P., Trowbridge, J., Kineke, G., 2015. Mechanisms of surface wave energy dissipation over a high-concentration sediment suspension. Journal of Geophysical Research: Oceans 120, 1638-1681.

Van Heerden, I.L.L., Wells, J.T., Roberts, H.H., 1981. Evolution and morphology of sedimentary environments, Atchafalaya Delta, Louisiana. AAPG Bulletin 65, 1689-1689.

Walker, N.D., Hammack, A.B., 2000. Impacts of winter storms on circulation and sediment transport: Atchafalaya-Vermilion Bay region, Louisiana, USA. Journal of Coastal Research 16, 996-1010.

Walsh, J. P., Nittrouer, C. A., Palinkas, C. M., Ogston, A. S., Sternberg, R. W., and Brunskill, G. J., 2004, Clinoform mechanics in the Gulf of Papua, New Guinea. Continental Shelf Research 24, 2487-2510.

Walsh, J.P., Nittrouer, C.A., 2009. Understanding fine-grained river-sediment dispersal on continental margins. Marine Geology 263, 34-45.

Wells, J.T., Kemp, G.P., 1981. Atchafalaya mud stream and recent mud flat progradation - Louisiana Chenier Plain. AAPG Bulletin 65, 1689-1690.

Wright, L.D., Friedrichs, C.T., Kim, S.C., Scully, M.E., 2001. Effects of ambient currents and waves on gravity-driven sediment transport on continental shelves. Marine Geology 175, 25-45.

Wright, L.D., Friedrichs, C.T., 2006. Gravity-driven sediment transport on continental shelves: a status report. Continental Shelf Research 26, 2092-2107.

CHAPTER 4: ANATOMY OF AN EARLY ORDOVICIAN STORM-DOMINATED, MUDDY CLINOTHEM: IMPLICATIONS FOR ACROSS-SHELF FACIES VARIABILTY

4.1 Introduction

4.1.1 Background

Fine-grained sedimentary rocks (i.e., mudstones) comprise the majority of sedimentary rock-types at the Earth's surface (e.g., Aplin and Macquaker, 2011), and their emergence as important hydrocarbon reservoirs has illuminated the need for a more complete understanding of the sediment transport processes and paleoenvironmental conditions associated with mudstone deposition (Passey et al., 2010). Over the past ~20 years, the conventional idea that all extensive successions of fine-grained rocks deposited in marine settings were exclusively deposited vertically from suspension in deep, quiescent water has been dispelled (e.g., Schieber, 1994; Macquaker and Bohacs, 2007; Bhattacharya and MacEachern, 2009; Macquaker et al., 2010; Aplin and Macquaker, 2011; Harazim and McIlroy, 2015). We know from studies of modern coastlines that extensive muddy prodeltaic deposits and inner-shelf mud-belts deposited subaqueously on high-energy shelves are relatively common geomorphic features. In fine-grained deltaic systems fundamental links exist between climate, weathering style, sediment dispersal and sediment colonization (Wheatcroft, 2000), and thus prevailing local oceanographic conditions are strongly coupled to differences in physical and chemical sediment attributes in these settings. It stands to reason therefore, that when fine-grained deltaic systems are preserved in the stratigraphic record, they have the potential to be excellent sedimentary archives capable of offering important insights into paleo-shelf conditions.

The distribution of sedimentary facies on the continental shelf is controlled by sediment input, local hydrodynamic conditions, and biologic reworking (e.g., Aigner and Reineck, 1982). Relative to their coarse-grained counterparts, studies of facies variability in

mudstones remain relatively rare (Bhattacharya and MacEachern, 2009). In spite of the common occurrence of muddy, high-energy deltaic deposits on modern continental shelves, geologists have rarely explicitly identified these deposits in the rock record (e.g., Schieber, 1999; Macquaker et al., 2010; Plint, 2014). This is in part because no catalog of easily recognized and distinguishing criteria exists to aid in the recognition of muddy deltaic deposits in the rock record; the products of mud dispersal, by the range of sedimentary processes that are known to operate in these settings, are relatively poorly known even in the modern. This problem is further compounded by the fact that the recognition of initial depositional processes, on the basis of identifying diagnostic laminae and bedding architectures, are frequently masked by the effects of post-depositional processes (e.g. bioturbation and compaction) and the effects of diagenesis, explicitly the dissolution of starting materials and precipitation of cements (e.g., Bentley et al., 2006; Aplin and Macquaker, 2011). In practice accurate paleoenvironmental interpretations and facies analysis of ancient muddy shelf environments requires a complete understanding of the continuum of processes capable of transporting, depositing and colonizing fine-grained sediments in offshore depocenters and an appreciation of how these products are subsequently modified by dissolution and cementation during burial.

4.1.2 Study Aims and Objectives

This study aims to investigate the origin of compositional, sedimentary fabric, and textural variations within the Early Ordovician deltaic mudstones of the Lower Paleozoic Power Steps Formation (Fm.) at Ochre Cove, Bell Island, Newfoundland in order to understand (1) how mechanisms of sediment dispersal vary with progradation; (2) how the component grain origins change as the delta evolves in response to progradation; (3) if there are any obvious changes in sediment provenance through the delta as the terrestrial signal is

increasingly diluted by sediment from other sources, and (4) how post-depositional changes, particularly bioturbation, overprint the diagnostic textural (depositional) attributes of the sedimentary fabric. The exposure at Ochre Cover, Bell Island, Newfoundland (Figure 4.2) offers a unique opportunity to study onshore-offshore mud transport and deposition across an Early Paleozoic muddy clinothem system. Millimeter- to cm-scale microfacies descriptions including compositional, textural, and biogenic sedimentary structures across multiple nested scales (outcrop > hand specimen > thin section) are employed to define facies and facies associations across the muddy clinothem. By integrating these observations we are able to set constraints on relative water depth, seafloor energy regime, and dominant sedimentary transport mechanisms – information essential for the construction of accurate paleoenvironmental and facies models. Detailed sedimentological descriptions are supplemented with petrographic descriptions and bulk rock and clay mineral compositional analyses (quantitative X-ray diffraction, QXRD), covering the clinothem topsets, foresets, and bottomsets are used to elucidate changes in bulk and clay mineralogy prior to and during clinothem building and ultimately how post-depositional processes variably overprint the facies in different regions of the clinothem.

4.2 Study Area and Geological Overview

The Lower Ordovician (Arenigian ~478-472 Ma) interval exposed at Ochre Cove, Bell Island, Newfoundland, Canada records the transition between the Bell Island and Wabana Groups (Figure 4.1). In Early Ordovician times, the study area is interpreted as being part of the Avalonian Terrane located on the western margin of Gondwana (Cocks and Torsvik, 2002). At the time of deposition, Avalonia was rifting away from Gondwana (Figure 4.1), and the Bell Island and Wabana Group strata were deposited in a graben between Precambrian strata to the NW and SE of Conception Bay, (Miller, 1983).

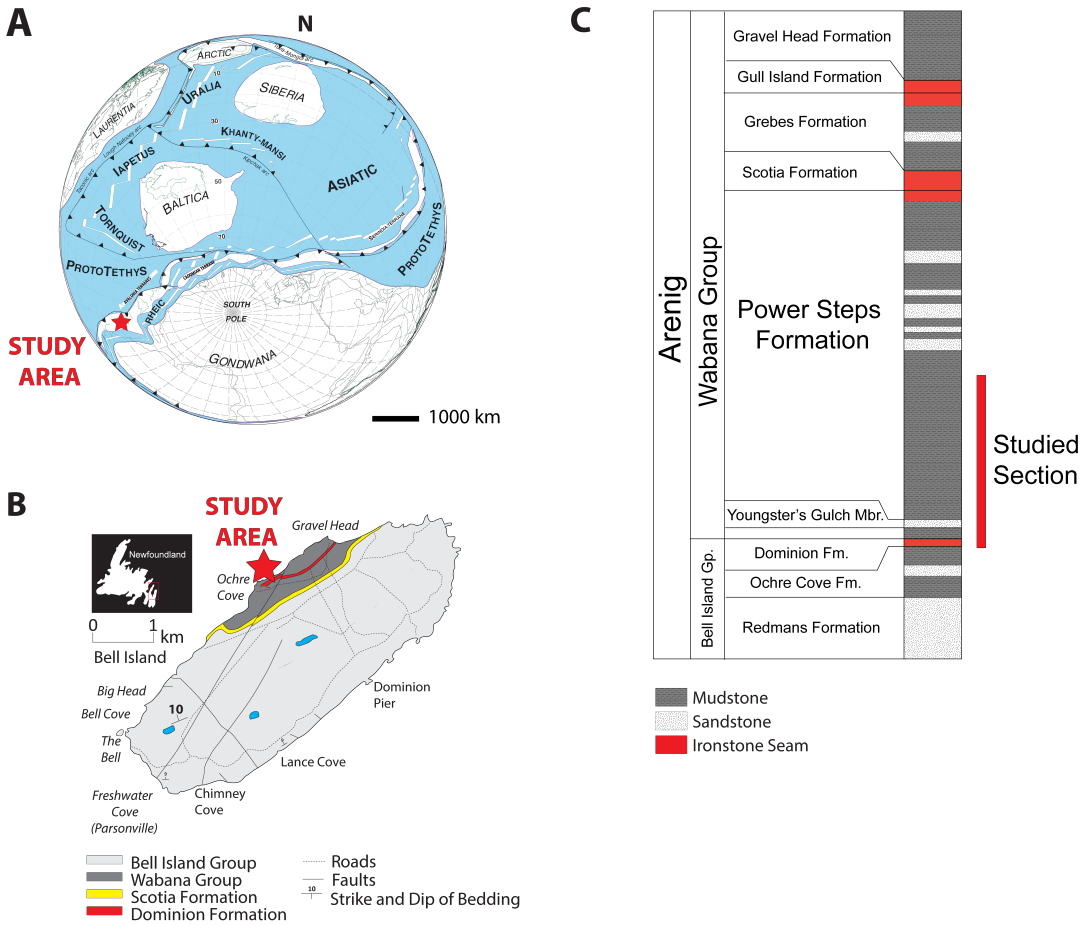

Figure 4.1. Paleogeographic reconstruction of the Early Ordovician margin of northern Gondwana indicating location of the Avalonian Terrane at ~65°S (modified from Stampfli et al., 2002); the approximate location of the study area within the Avalonian Terrane is indicated by a red star (A). Geological map of Bell Island, Newfoundland indicating the location of the study area at Ochre Cove (B). Stratigraphic chart indicating the location of the studied interval (C) within Wabana Group Strata (modified from Ranger et al., 1984).

At Ochre Cove, the exposed interval comprises 4m of well-defined Dominion Fm. strata, an oolitic, chamositic ironstone that is non-conformably overlain by the lowermost Wabana Group, which encompasses the Power Steps Formation and the Youngsters Gulch Member (Figure 4.1c). The Youngster's Gulch Member is composed of inter-bedded, clay-rich, silt-bearing mudstones and meter thick, pyritic mudstone. The Power Steps Fm. is composed of clay- and silt-rich mudstone that is inter-bedded with cm- to dm-thick medium- to coarse-grained sandstone (Ranger et al., 1984). The formation has previously been interpreted broadly as having been deposited in a tidally-dominated deltaic environment

(Ranger et al., 1984), with detrital components sourced from the Pre-Cambrian Harbour Main, Conception, and Cabot groups as well as fro the Holyrood plutonic series (e.g., Bruckner, 1969).

4.3 Materials and Methods

4.3.1 Characterization of Sedimentary Fabrics

In order to examine the sedimentary processes responsible for the dispersal of sediment and the deposition of the exposed clinothem at Ochre cove (Figure 4.2), outcrops of the Power Steps Fm. and Youngster's Gulch Mbr. were logged at a cm scale (Figure 4.3). Oriented block samples (hand specimens) of unweathered mudstone and sandstone were collected from the field, stabilized with epoxy resin, and slabbed in the laboratory. Additionally, petrographic thin sections (thickness ~25 μm) were prepared from select slabbed intervals (Figure 4.3) and scanned at high resolution using a flat bed film scanner attached to a PC. Detailed sedimentological and ichnological observations (with bioturbation indices from Taylor and Goldring (1993)) taken from outcrop, hand specimen, and petrographic thin sections were integrated in order to generate rock descriptions that record trends in grain size, bedding fabrics, mineralogical composition and the origin of framework components (grains versus cement) using the methodology of Lazar et al. (2015) and extending it to encompass sandstone facies in order to develop sedimentary facies for constraining both depositional environment and sediment transport mechanisms. Detailed study of sediment composition and sedimentary fabrics was undertaken using a JEOL JSM-6330F Cold Cathode Field Emission Scanning Electron Microscope (SEM) equipped with an Oxford Instruments Aztec Energy Dispersive X-ray System equipped with a silicon drift detector. Images were obtained primarily in backscattered mode utilizing a JEOL solid-state backscatter detector. Imaging conditions were 15 kV and 15mm working distance. Thin

sections were prepared for SEM imaging by cleaning lightly with methanol using low lint cloths and air dried, then coating with approximately 40nm of carbon using a Cressington 208 carbon evaporator.

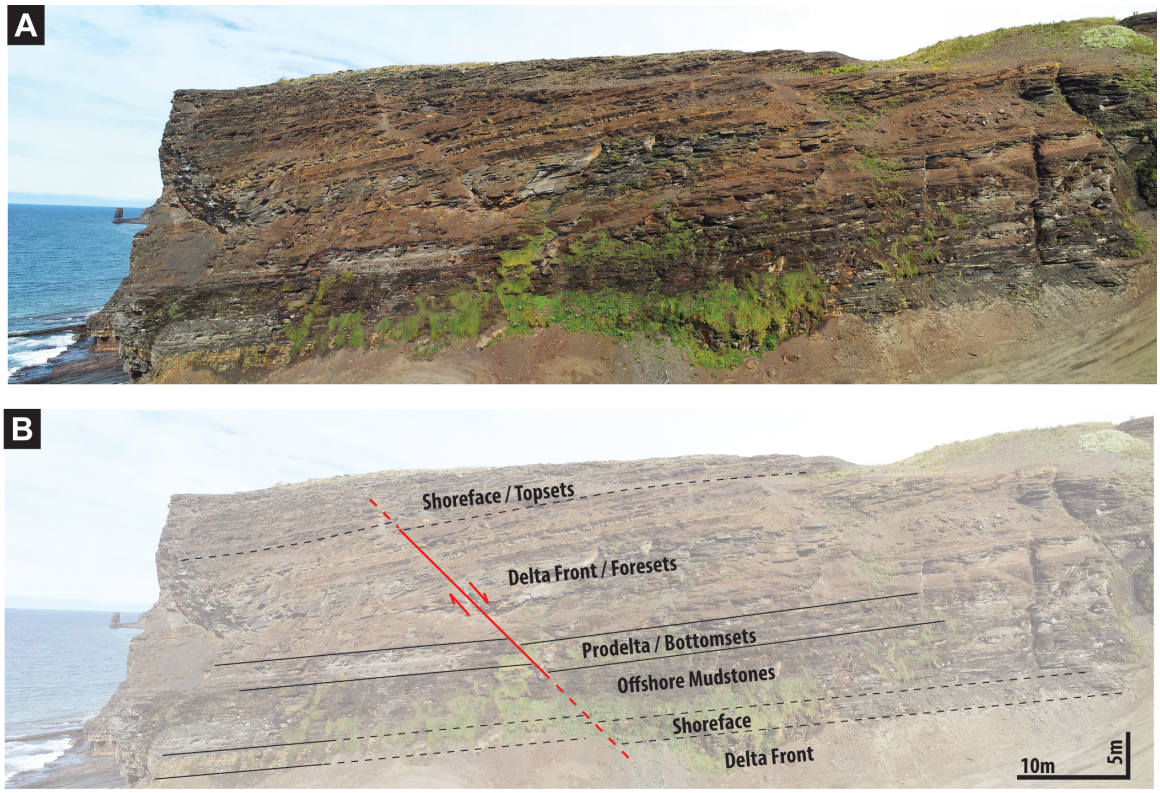

Figure 4.2. View of the clinothem exposure (Youngster's Gulch Mbr. and Power Steps Fm.) at Ochre Cove, Bell Island, Newfoundland (A). Annotated view of the clinothem exposure indicating the major facies associations, see text for discussion (B).

4.3.2 Compositional Analysis

Whole rock and clay mineral Quantitative X-Ray diffraction (QXRD) analyses were preformed in order to characterize differences in composition so that variations in provenance might be better constrained. Samples for whole rock QXRD were prepared by processing ~ 2g of crushed material in ethanol and micronizing in a McCrone mill for ~ 3 minutes. Samples were then dried at 60°C and disaggregated using a mortar and pestle. Randomly oriented sample material was loaded into aluminum sample holders following the methods of

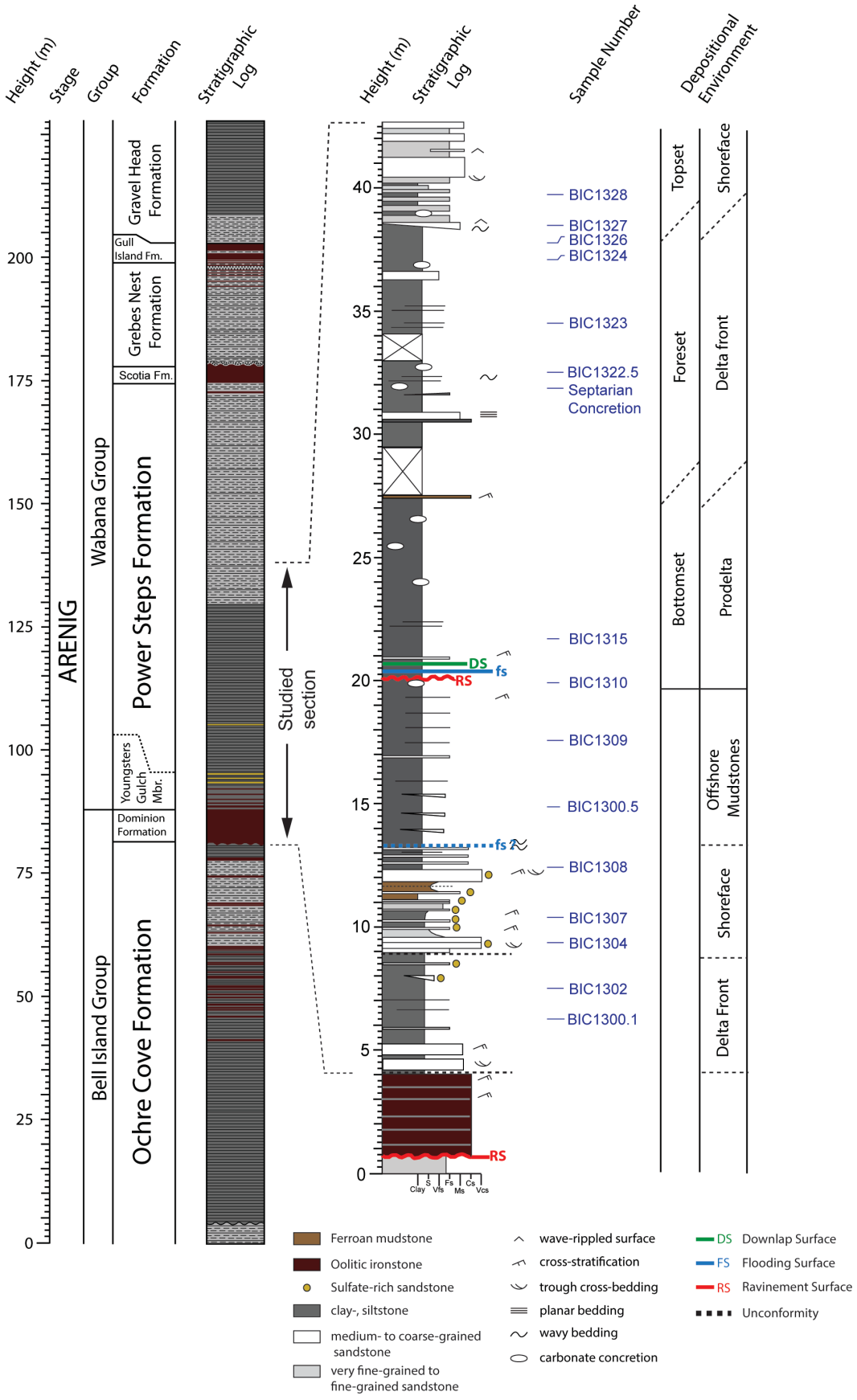

Figure 4.3. Generalized stratigraphic log of the clinothem exposure at Ochre Cove, Bell Island, Newfoundland indicating sampling locations and interpreted depositional environments (for discussion, see text).

Poppe et al. (2001). For clay mineral analysis, the size fraction equivalent to <2 μm spherical diameter of quartz was separated by dispersing a representative sample of whole rock power in a 0.1% sodium phosphate solution and extracting particles from the upper 5cm of suspension after settling for 3 hours and 10 minutes as determined by Stokes' Law. Oriented clay smears were prepared following the methods of Moore and Reynolds (1997).

XRD data were collected using a Panalytical Empyrean X-ray diffractometer with CuKα radiation (40 kV and 20 mA). For clay mineral analysis XRD runs were performed for each sample after each of the following four steps: (1) air-drying; (2) ethylene glycol salvation at 25°C for a minimum of 8 hours; (3) heating at 300°C for 1h; and (4) heating at 550°C for one hour. Clay minerals were identified by comparing peak positions and intensity of basal (001) reflections on the four XRD diagrams (Moore and Reynolds; Poppe et al., 2001). Semi-quantitative determination of bulk and clay mineral composition was facilitated by using MacDiff software (Petschick, 2001), with the uncertainty in XRD analysis estimated at ±5%. For clay mineral abundances are based on peak areas and normalized to Smectite + Illite + Kaolinite + Chlorite = 100%.

4.4 Results

4.4.1 Facies Descriptions

Eight sedimentary facies were defined in the studied succession by integrating grain size, sedimentary fabric, and mineralogical data derived variously from outcrop (Figure 4.3), hand specimen, thin section, SEM, and QXRD (Table 4.1) analyses. The stratigraphic distribution of the main mineralogical trends in the mudstones of the Power Steps Fm. follows the description of the individual sedimentary facies.

Table 4.1. Bulk and Clay Mineral QXRD Results

Sample Name	Height (m)	Bulk Mineralogical XRD Results				Clay Mineral XRD Results		
		Clay	Quartz	Plagioclase	Pyrite	Illite	Chlorite	Chlorite/ Illite
BIC 1328	39.35	49	43	8	0	39	61	0.63
BIC 1327	38.50	64	32	4	0	46	54	0.86
BIC 1324	37.10	58	37	5	0	51	49	1.05
BIC 1323	34.50	43	50	7	0	43	57	0.76
BIC 1322.5	32.5	63	34	3	0	45	55	0.80
BIC 1315	21.00	49	45	6	1	48	52	0.91
BIC 1309	17.60	34	56	8	2	46	54	0.86
BIC 1308	12.45	42	46	7	5	56	44	1.28
BIC 1307	10.35	38	54	7	2	23	77	0.29
BIC 1304	9.35	16	15	0	1	3	81	0.04
BIC 1302	7.50	43	50	5	2	13	87	0.15
BIC 1300.1	6.25	33	53	13	1	9	91	0.10

Facies 1: Medium-grained, cross-stratified wave-reworked sandstone

Facies 1 (F1) consists of thin bedded (5-10cm), sharp-based, normally-graded, ripple laminated (bi-directional planar cross-stratified and curved downlapping geometries), medium-grained quartz arenites with bioturbated tops (BI 1-2; 5-30%), interbedded with grey mudstones of Facies 7 (Figure 4.4). *Planolites* and *Teichichnus* (Figure 4.4b) burrows are recognized in the tops of these sandstones.

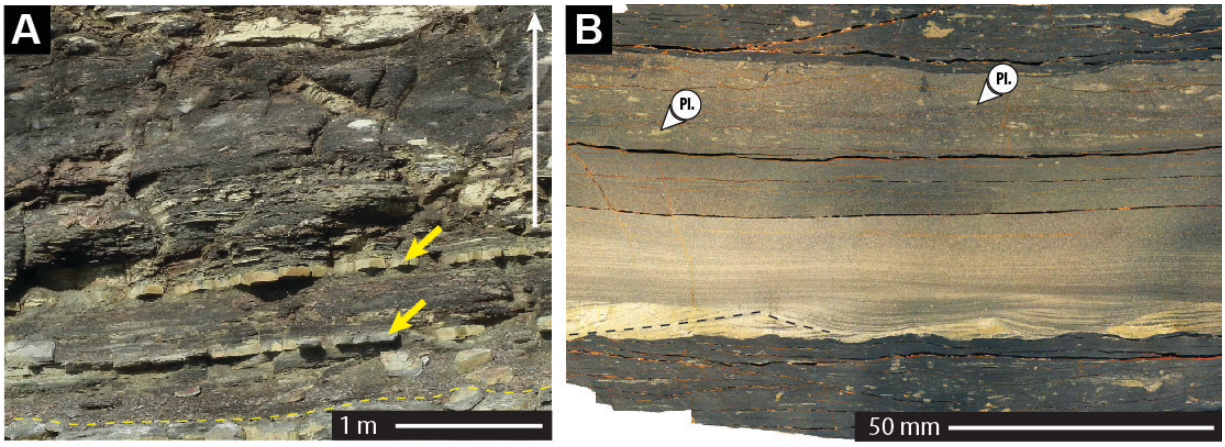

Figure 4.4 Facies 1: Medium-grained cross-stratified wave-reworked sandstone. A) Outcrop image showing thin-bedded sandstones (yellow arrows) interbedded with grey mudstone. B) Polished hand sample (sampling location BIC1302; Figure 4.3) showing low-angle cross-stratification (black dashed line) overlain by trough cross-bedding (*Pl; Planolites*).

Facies 2: Medium-grained, wave- and current- rippled-sandstone

Facies 2 (F2) is only present close to the top of the studied section, and consists of thin- bedded (5-10 cm) fine- to medium-grained, normally-graded sandstone beds with bioturbated tops, that are interbedded with mudstone beds of Facies 7 (Figure 4.5a). These thin-bedded sandstones have erosive bases, and commonly display wave- and combined-flow-ripples in their basal portions (Figure 4.5bc). These beds and bedsets are commonly laterally continuous on the scale of the exposure (Figure 4.5a and b). The sandstone of this facies comprise subangular to subrounded grains predominantly composed of fine sand-sized quartz in addition to some silt-sized detrital mica (muscovite and biotite). These units also contain detrital fine-sand-sized reworked pyrite grains. This reworked pyrite particularly forms continuous lags (on the scale of >30 cm) present at the base of individual beds that underlie migrating ripple laminae (Figure 4.5d). The bed tops are sparsely bioturbated (BI 1-2; 5-30%); with sand-filled, compacted *Planolites* being visible.

Facies 3: Normally-graded, fine-to coarse-grained sandstone with muddy tops and calcite-cemented concretions

Facies 3 (F3) consists of laterally continuous, m-thick, sharp-based, normally-graded, parallel-bedded, fine- to coarse-grained sandstones with muddy tops (Figure 4.6a and b). Individual beds are separated by erosion surfaces that overlie well-developed, elongated dm-thick, and m-long, concretions (Figure 4.6a). These concretions comprise silt-bearing calcite-cemented medium mudstones with septarian veins of calcite (Figure 4.6c) and are located in the muddy tops of the beds. The concretions comprise fine-silt silt-sized quartz, biotite, and muscovite grains and an associated matrix fraction composed of chlorite and illite in calcite and pyrite cements that occlude uncompacted intergranular porosity.

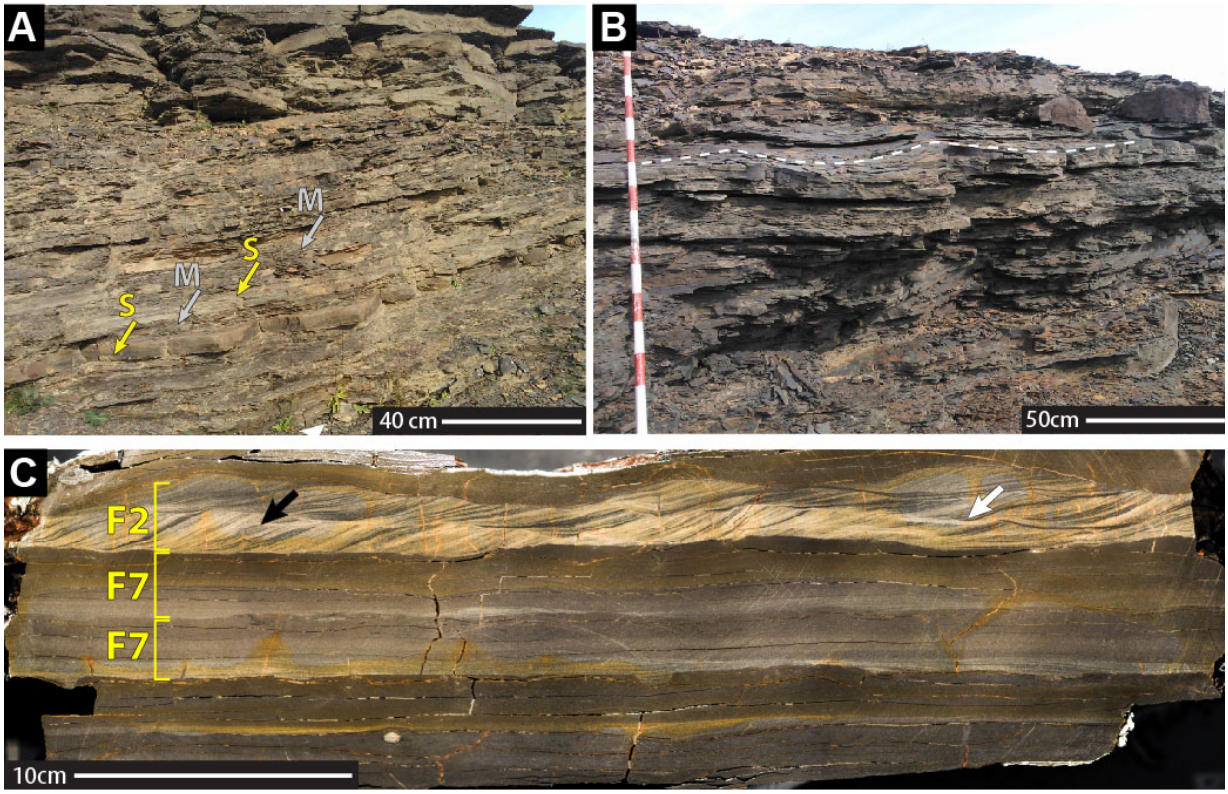

Figure 4.5 Facies 2: Medium-grained, wave- and current-rippled sandstone. A) Outcrop image from sampling location BIC1327 (Figure 4.3) showing dm-thick fine- to medium-grained wave- and current-rippled sandstone beds (S) interbedded with cm- to dm-scale mudstones (M) of Facies 7: Normally-graded, largely homogenous siliciclastic coarse mudstone. B) Outcrop image from sampling location BIC1327 showing continuous, wavy-bedded sandstone (white dashed line). C) Hand sample image from sampling location BIC1327 showing sandstones of Facies 2 (F2) overlying mudstones belonging to Facies 7 (F7). Centimeter-scale, prograding current ripples (black arrow) and combined flow ripples (white arrow) are commonly observed in F2.

Facies 4: Current-ripple laminated, normally-graded, siliciclastic coarse mudstone

Facies 4 (F4) consists of normally-graded, current-ripple laminated, siliciclastic coarse mudstones that form discontinuous beds that are up to dm thick (Figure 4.7a). The basal regions of individual beds commonly consist of cm-thick, discontinuous migrating current ripples with erosive bases and amplitudes of 3-5 mm (Figure 4.7). These ripple-laminae are sharply overlain by faintly parallel discontinuously laminated, silt-rich mudstones that make up the majority of individual beds. While no bioturbation is observed in the basal coarser-grained lamina sets, the overlying laminae have been partially disrupted by sparse burrow mottles (BI 0-2; 0-30%). Sand-filled *Planolites* and *Gyrolithes* are identifiable

(Figure 4.7b and c). Petrographic and QXRD analyses reveals that the framework grains mainly comprise subangular to subrounded, coarse-silt to fine-sand sized quartz in addition to altered lithic grains, biotite with some plagioclase and muscovite (see Table 4.1). Illite and chlorite form the matrix fraction (Figure 4.7e, f; Table 4.1).

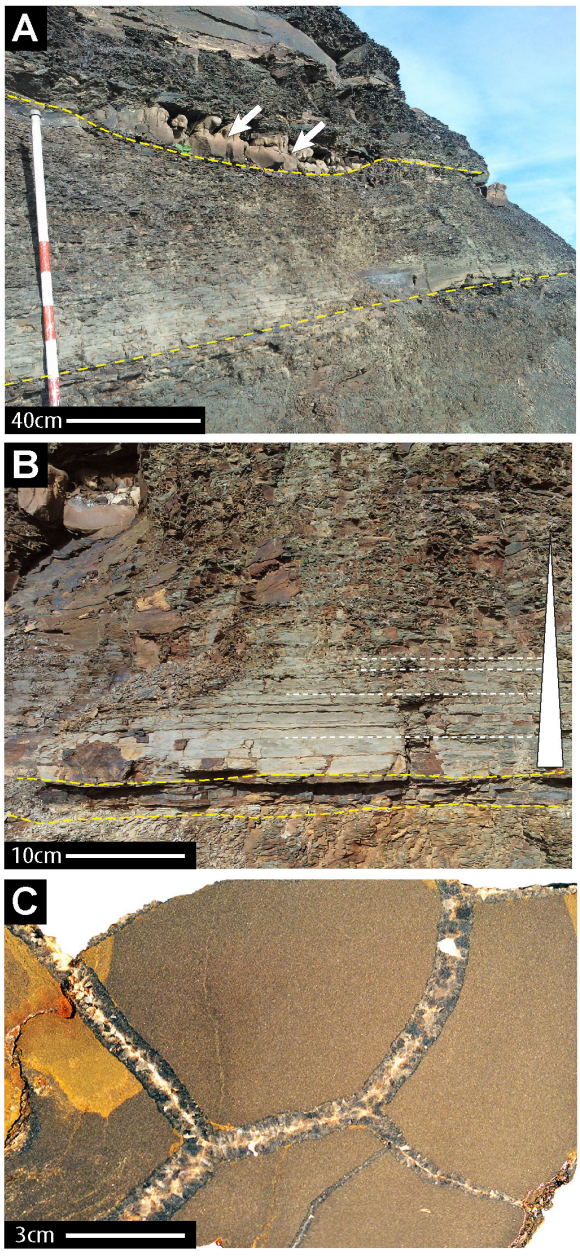

Figure 4.6 Facies 3: Normally-graded, fine- to coarse-grained sandstones with muddy tops and concretions. A) Laterally continuous, m-thick erosive-based laterally continuous medium- to coarse-grained sandstone bed. White arrows indicate dm-thick package of septarian ferrous-limestone concretions. B) Normally graded sandstone bed. The dashed yellow lines indicate erosive surfaces. C) Hand sample image of a septarian ferrous-limestone concretion (sampling location "septarian concretion"; Figure 4.3) with calcite-filled fractures.

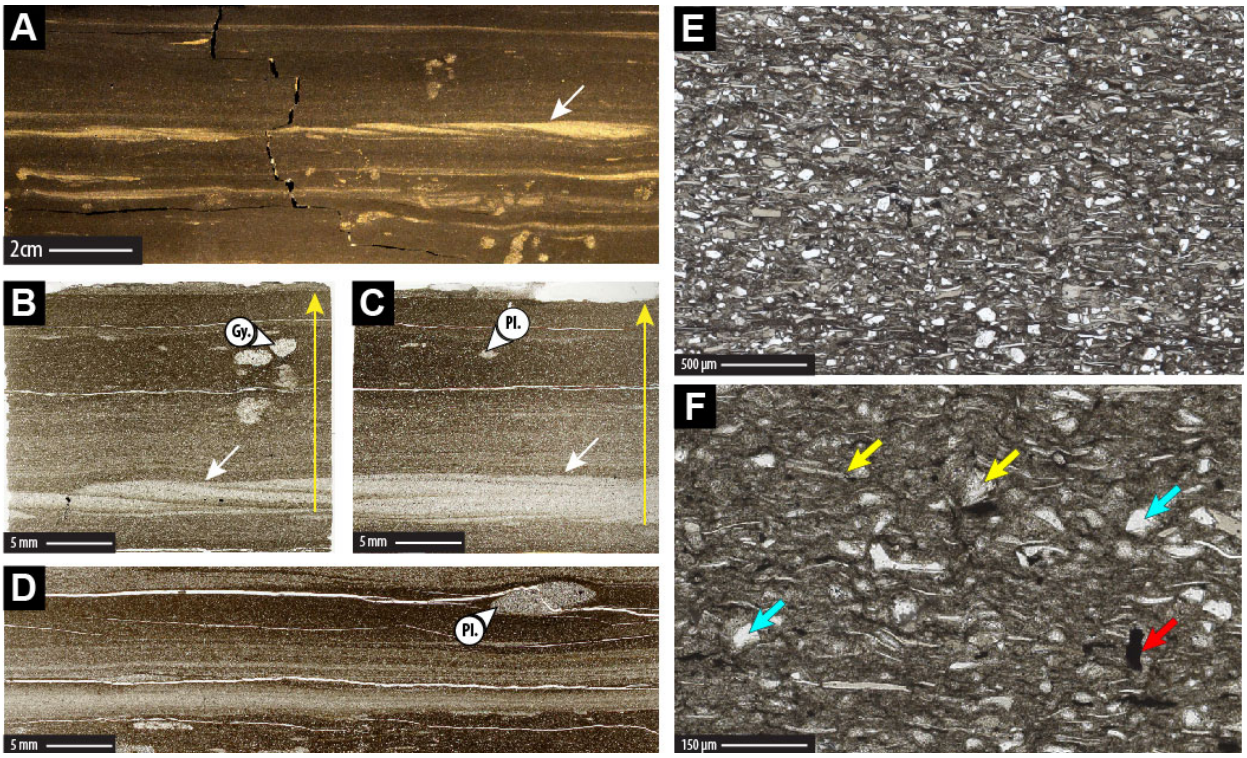

Figure 4.7 Facies 4: Current-ripple laminated, normally-graded, coarse mudstone. A) Hand-sample from sampling location BIC1300.1 (Figure 4.3) showing thin, discontinuous, wavy, normally-graded silt- and very fine-grained beds contained starved wave and combined-flow ripples (white arrows). B) Thin section scan from sampling location BIC1300.1 taken parallel to sediment transport direction and C) and D) perpendicular to sediment transport direction showing well-developed unidirectional aggrading current ripples (white arrows); *(Gy, Gyrolithes; Pl; Planolites)*. E) and F) Thin section micrographs from sampling location BIC1300.1 subangular to subrounded "floating" silt-sized quartz grains (blue arrows) with some biotite, muscovite, and plagioclase embedded in a chloritic matrix with some illite. Some mafic minerals altering to chlorite (yellow arrows) are observed, as well as opaque minerals, and kerogen (red arrows).

Facies 5: Wave-ripple laminated, normally-graded, siliciclastic coarse mudstones

Facies 5 (F5) consists of stacked successions of thin (5-10 cm), sharp-based, wave-ripple laminated, normally graded, siliciclastic coarse mudstone beds (Figure 4.8a). Beds of this facies are laterally discontinuous at a dm-scale (Figure 4.8b). The upper regions of these beds are commonly truncated. Internally these beds are normally-graded, and either exhibit discontinuous-wavy laminae, or are homogenous looking (Figure 4.8c). Sparse burrow mottles are visible (BI 0-2; 0-30%); sand-filled *Planolites* and escape structures are observed near the bed tops. Petrographic and QXRD analyses reveal that the framework grains mainly

comprise coarse-silt sized quartz, some altered (chloritized) lithic grains, in addition to biotite with minor muscovite and plagioclase. Illite and chlorite form the matrix fraction.

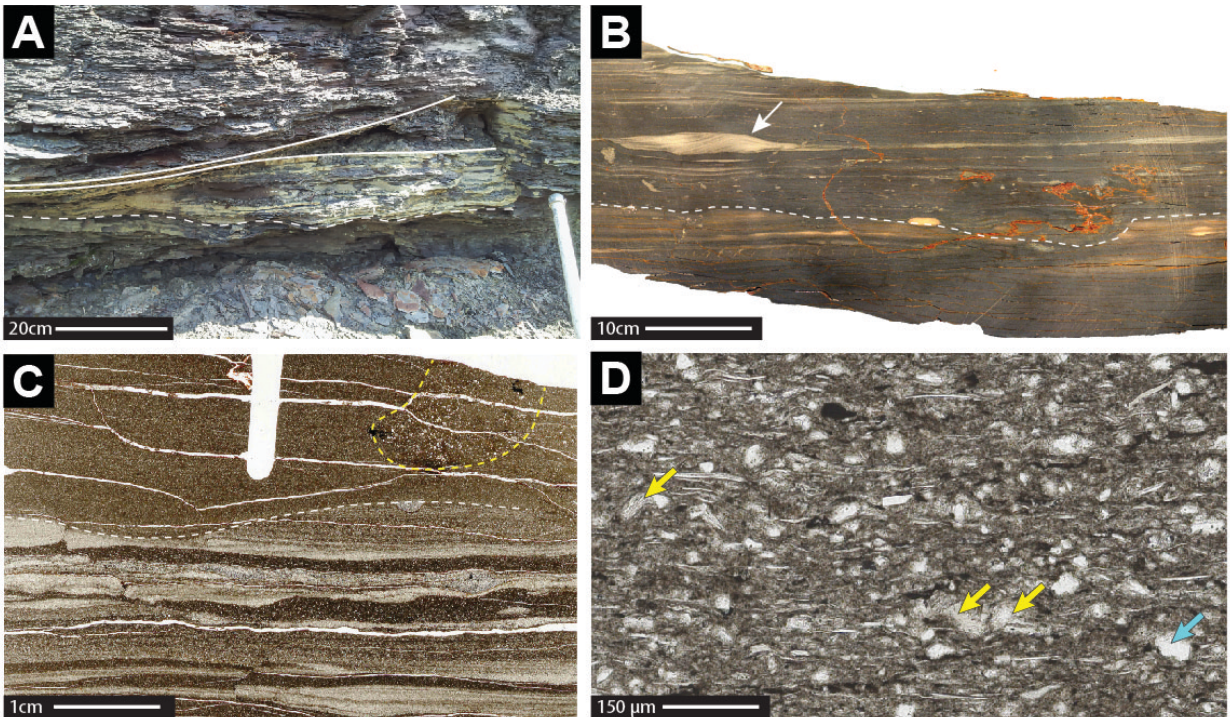

Figure 4.8 Facies 5: Reworked, wave-rippled, silt-rich mudstone. A) Outcrop image of sampling location BIC1307 (Figure 4.3) showing wavy cross lamination in clay- and silt- rich mudstones units (dashed white line) and concave (solid white lines) bedding geometries with erosive tops, (black arrow). B) Polished hand sample from sampling location BIC1307 (Figure 4.3) showing starved combined flow ripples (white arrow) and irregular erosional contacts (white dashed line). C) Thin section scan from sample BIC13007 showing thin bedded (<1cm), fining upwards beds with wavy-erosive bases. Sand-filled gutters are commonly observed. Bioturbation is sparse, and only biodeformational features (yellow dashed line) and compacted, sand-filled *Planolites (Pl.)* are observed. D) Thin section micrograph from sampling location BIC13007 showing subangular to subrounded "floating" silt-sized quartz grains (blue arrows) with some biotite, muscovite, and plagioclase embedded in a chloritic matrix with some illite. Some mafic minerals observed as altering to chlorite (yellow arrows).

Facies 6: Wave-ripple laminated, normally-graded, siliciclastic medium mudstones

Facies 6 (F6) consists of stacked succession of thin bedded (1-5mm), erosive-based, normally graded, siliciclastic medium mudstones. The beds are discontinuous laterally at a dm scale. Internally the laminae are curved and locally downlap onto underlying bedding planes (Figure 4.9). Sand-filled gutter casts, composed of fine sand are observed at the base of many beds. Locally, coarse-silt to medium-sand filled mm-sized burrow mottles are visible

(BI 1-2; 5-30%) that are attributed to *Planolites*. Petrographic and QXRD analyses reveal that the framework components are predominantly composed of quartz, altered (chloritized) lithic fragments, and biotite, in addition to some muscovite and plagioclase. Illite and chlorite form the matrix fraction.

Facies 7: Normally-graded, largely homogenous siliciclastic coarse mudstone

Facies 7 (F7) consists of coarse siliciclastic mudstones organized into cm-scale, normally-graded beds with curved erosional bases (Figure 4.10a). Individual beds are laterally continuous at a dm-scale. Visible burrows are rare (BI 0-1; 0-5%); although small, quartz sand-filled *Planolites* and some biodeformational structures are observed close to the top of beds (Figure 4.10b). Petrographic and QXRD analyses reveal that the framework fraction is composed of silt-sized quartz, altered (chloritized) lithic grains, and biotite with some muscovite and plagioclase (Figure 4.10c, d). The matrix comprises chlorite, illite, small opaque pyrite grains (Figure 4.10d) and dark, mm-sized wavy-elongated kerogen stringers (Figure 4.10d).

Facies 8: Homogenous, siliciclastic medium mudstone

Facies 8 (F8) consists of largely homogenous looking, siliciclastic medium mudstone beds (Figure 4.11a, b). Individual beds are continuous at dm-scale. Locally, faint undulatory-parallel laminae defined by subtle changes in the proportion of medium to coarse silt are visible. Identifiable burrows are rare; only small, infrequent biodeformational structures are observed (BI 0-1; 0-5%). The framework fraction is composed of medium- to coarse- silt-sized quartz, altered (chloritized) lithics, and biotite with some muscovite and plagioclase. The matrix comprises chlorite, illite, small opaque pyrite grains and dark, mm-sized wavy-elongated kerogen stringers (Figure 4.11c,d).

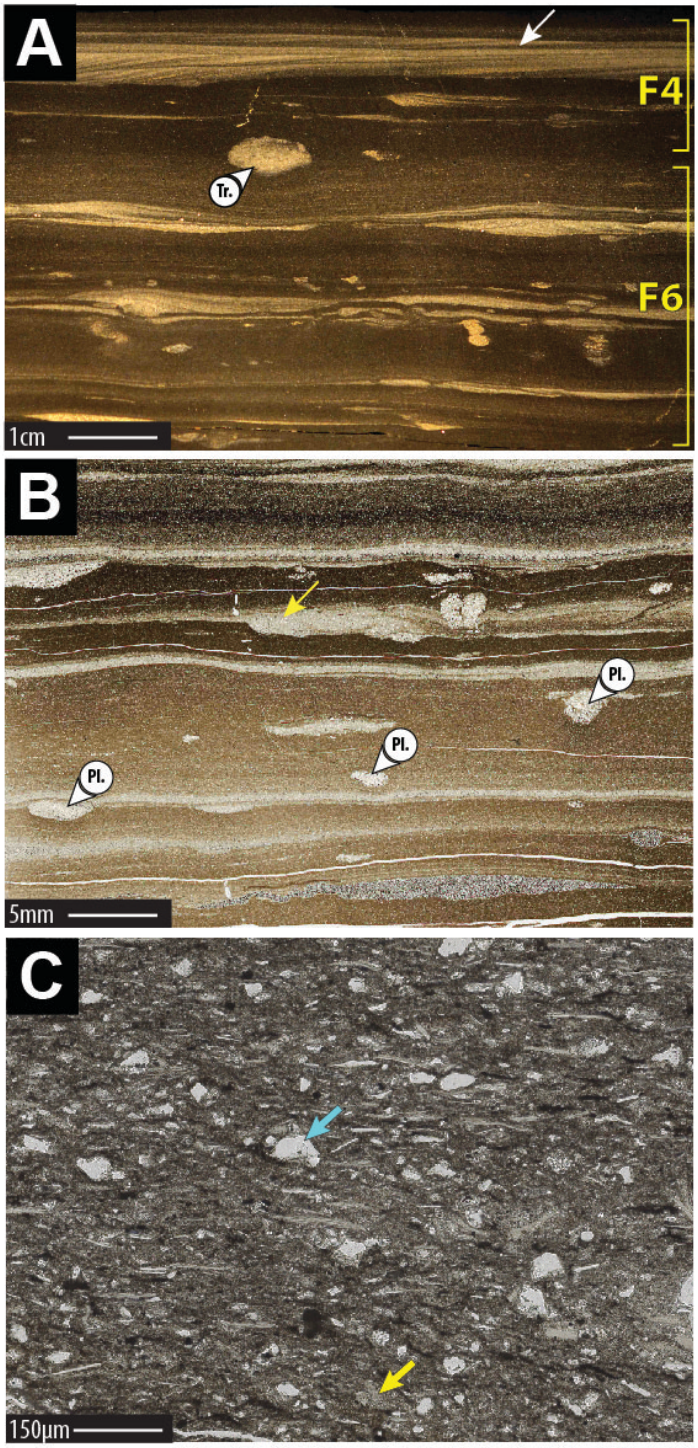

Figure 4.9 Facies 6: Wave ripple laminated, normally-graded, medium mudstone. A) Polished hand sample from sampling location BIC1300.1 (Figure 4.3) showing erosive-based wavy-discontinuous, fining-upwards beds. Sand-filled gutters are commonly observed; (*Tr; Trichophycus)* F6 is overlain by current-rippled, normally-graded silt-rich mudstones from F4. B) Polished thin section scan from sampling location BIC1300.1 (Figure 4.3); (*Pl; Planolites)*. C) Thin section micrograph from sampling location BIC1300.1 (plane polarized light) showing subangular to subrounded "floating" silt-sized quartz grains (blue arrows) with some biotite, muscovite, and plagioclase embedded in a chloritic matrix with some illite. Mafic minerals altering to chlorite (yellow arrows) are observed.

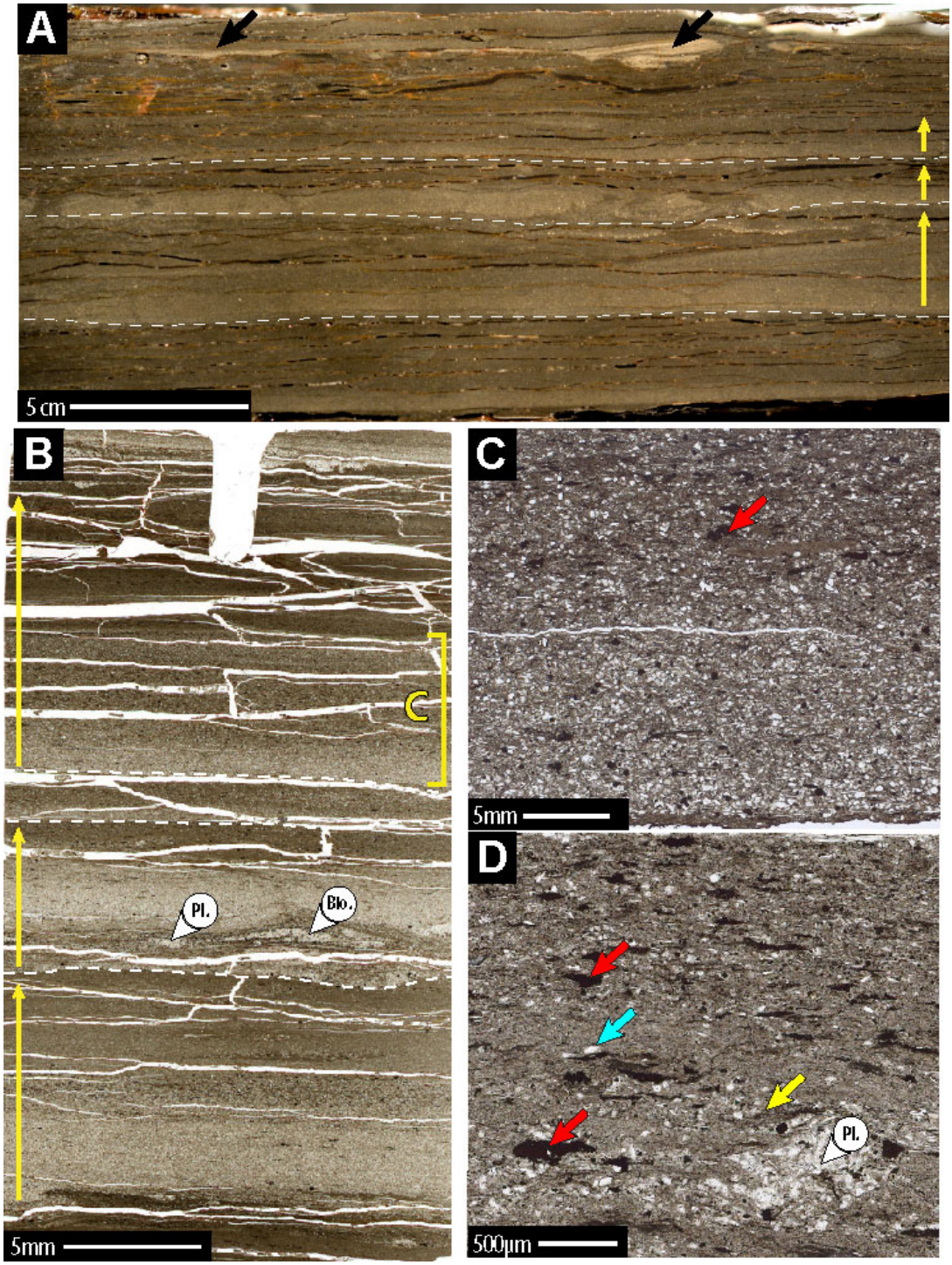

Figure 4.10 Facies 7: Normally-graded, largely homogenous coarse mudstone A) Polished hand sample from sampling location BIC1300.5 (Figure 4.3) showing erosive based (white dashed lines) normally graded beds (yellow arrows). B) Polished thin section scan from sampling location BIC1300.5 (Figure 4.3) showing three event beds (yellow arrows); (*Pl; Planolites, Bio; biodeformation)*. C) Thin section micrograph from sampling location BIC1300.5 (plane polarized light) showing a single normally graded event bed (unit "C" in B). D) "Floating" silt-sized quartz grains (blue arrows) with some biotite, muscovite, and plagioclase embedded in a chloritic matrix with some illite. Some mafic minerals altering to chlorite (yellow arrows) and kerogen stringers (red arrows) are observed.

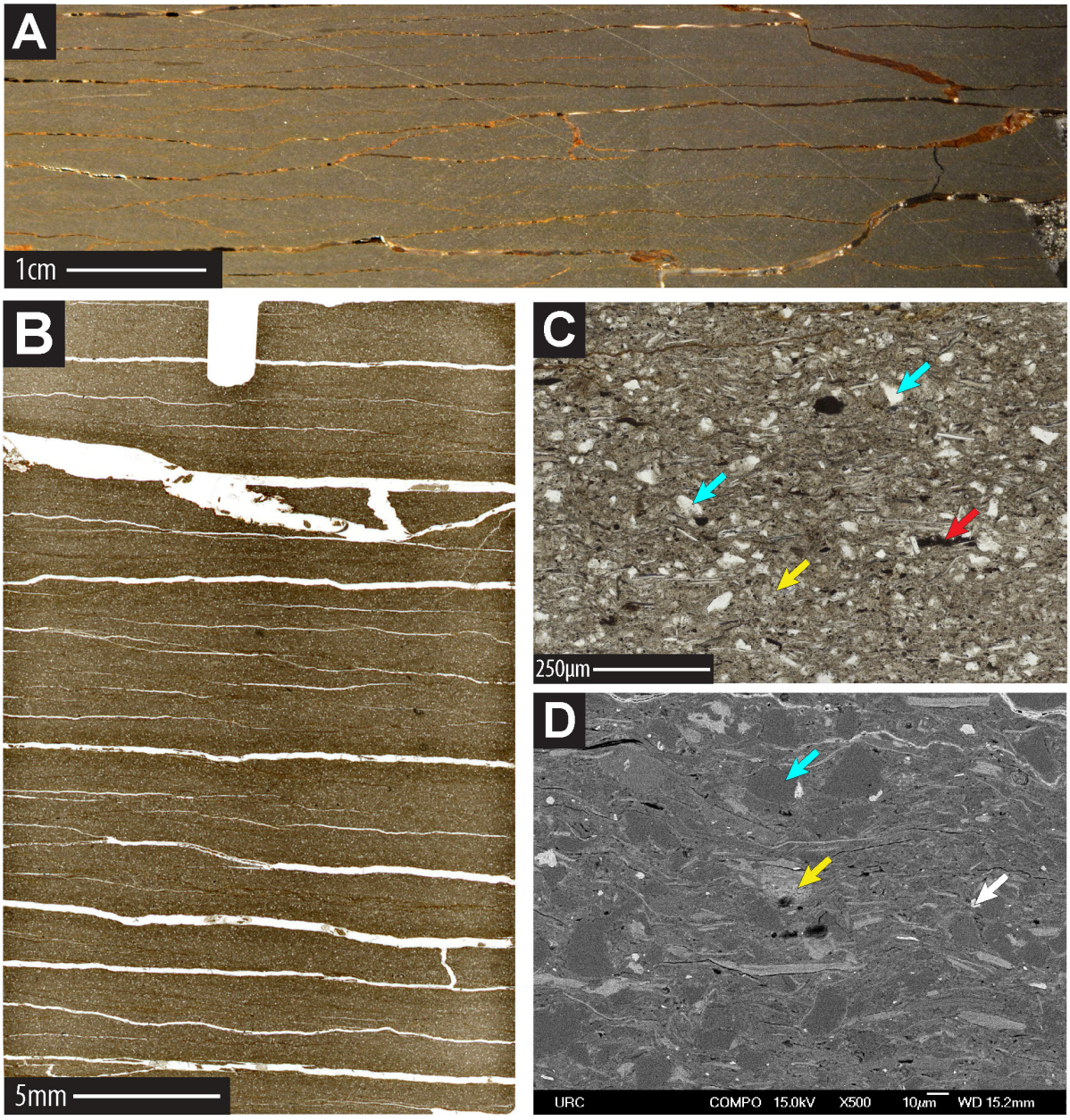

Figure 4.11 Facies 8: Homogenous, siliciclastic medium mudstone A) Polished hand sample from sampling location BIC1312 (Figure 4.3) showing apparently homogenous mudstones. B) Thin section scan from sampling location BIC1312 showing faintly laminated mudstones. Laminations are characterized by subtle changes in the amount of silt-sized quartz grains. C) Thin section micrograph from sampling location BIC1312 (plane polarized light) showing subangular to subrounded "floating" silt-sized quartz grains (blue arrows) with biotite, muscovite, altered (chloritized) lithic grains and plagioclase embedded in a chloritic matrix with some illite. Some mafic minerals are altering to chlorite (yellow arrows). D) Backscatter SEM image of sample BIC1312 showing silt-sized quartz grains (blue arrow), biotite, and minor amounts of altered lithic grains (yellow arrows) and biotite in a chlorite-illite matrix. SEM analysis reveals that in addition to the chloritization of altered lithic grains, a substantial fraction of the silt-sized chlorite grains appear to be detrital in origin. Detrital pyrite and pyrite cements are accessory components.

4.4.2 Stratigraphic Distributions of Component Minerals in the Mud-Dominated Facies

The results of QXRD analysis are presented in Table 4.1 and Figure 4.12. These data show substantial mineralogical variability through the studied succession. In general, total clay as a percentage of the total rock volume increases vertically through the succession. Quartz as a percentage of total rock volume, however, shows only slight variations in percentage of the total rock volume, decreasing from > 50% of rock volume at the base of section to ~30-40% of rock volume at the top. A notable deviation from this trend is observed at ~9m (Figure 4.12), where quartz contributes only ~14% of the rock volume. Plagioclase as a percentage of the total rock volumes follows the same trends as quartz, decreasing from >10% of the total rock volume at the base of the studied section to ~5% at the top. Overall the ratio of clay minerals to quartz in the succession increases vertically.

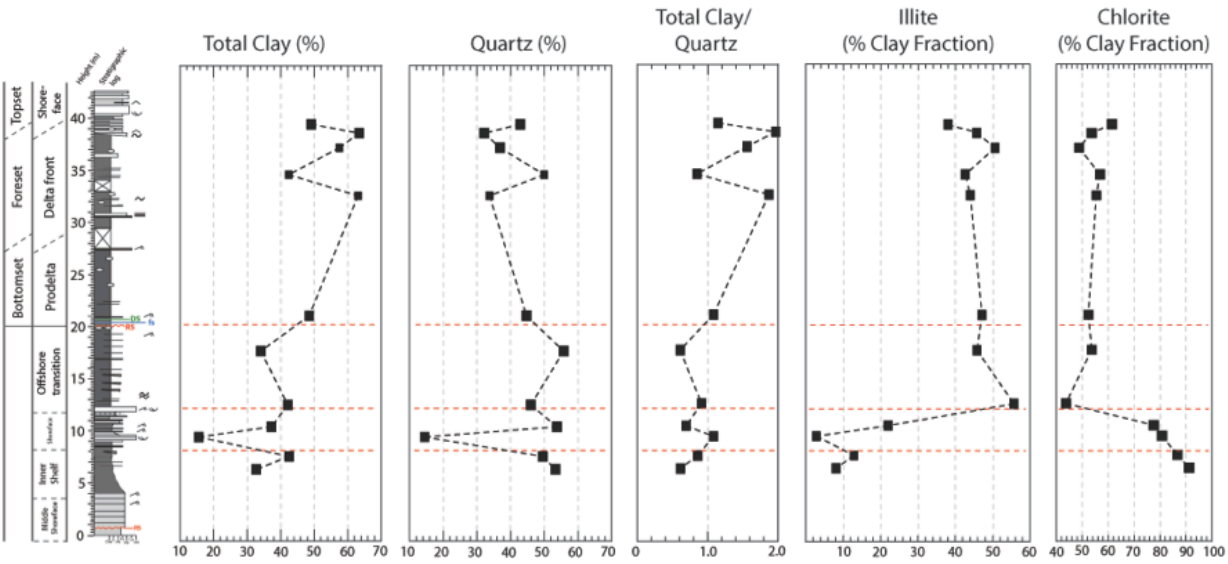

Figure 4.12. Figure showing the bulk and clay mineralogical composition of the studied interval at Ochre Cove. Note the increase in the ratio of clay minerals to quartz and the shift in the dominant clay mineral from chlorite to illite.

The composition of the clay minerals also varies within the succession. Chlorite as a percentage of the clay mineral volume decreases throughout the succession from >90% of the clay mineral assemblage at the base of the studied to a low of 43% at 12.5m stratigraphic

height (Figure 4.3) above which the percentage of chlorite remains relatively constant at ~55% of the clay mineral volume. Illite as a percentage of the clay mineral volume increases throughout the succession from <10% at the base of the studied section to a maximum of 57% at 12.5m stratigraphic height above which the percentage of illite remains relatively constant at ~45%. Pyrite is observed as an accessory component, comprising <5% of the total rock volume, in the lower 20m of the exposure, coinciding with the location of the "pyritic sandstones" described by Ranger et al. (1984) (Figure 4.3).

4.5 Discussion

4.5.1 Depositional Processes

The sedimentary facies observed in the studied section of the Power Steps formation generally display bed attributes, namely normal grading, erosional bases, and bioturbated tops, that indicates that they were likely the depositional products of episodic, storm-driven event sedimentation. Although storm conditions may exist only for a small portion of time within a depositional environment, their influence on sediment transport and deposition are disproportionately large because they are erosional and deposit thick beds (Plint, 2010). Most of the event beds within the Power Steps Fm. are sharp-based, which indicates that the currents ultimately responsible for deposition were initially of sufficient energy to erode the underlying strata. Together these attributes are consistent with the evolution of an idealized storm bed as described by Cheel (1991). The existence of ripple lamination in the basal portions of these storm beds suggests that the flow was initially traction dominated, while normal grading in the medial portions indicates subsequent deposition was by suspension settling from waning flow. The flow types capable of generating these types of deposits include density-driven currents, wave-induced oscillatory flows, and combined flows, a detailed discussion of these is provided in the following section. Density-driven currents,

wave-induced oscillatory flows, and combined flows indicate sediment deposition in a shelf setting. The predominant of wave structures across almost all facies suggests that the shelf was probably located in relatively shallow water. The ichnological characteristics observed across all facies including sparse bioturbation limited to the muddy tops of beds that were deposited during the waning stages of flow and escape structures suggest rapid, episodic sedimentation events that did not allow the seabed to be fully colonized (e.g., MacEachern et al., 2010).

4.5.1.1 Density-Driven Current Deposits

Fine- to coarse-grained sandstones (F3) and normally-graded, and current-rippled, silt-rich mudstones (F4), share sedimentary structures, grading relationships, and ichnological characteristics which suggest deposition from a flow that was originally erosion and traction-dominated, with no evidence for wave-generated oscillation, and evolved to suspension settling from a waning flow; suggesting that these facies are the depositional products of density-driven currents (i.e., sediment gravity flows). Density-driven current deposits tend to become thinner, more finely-grained and laterally discontinuous in an offshore direction (e.g., Aigner and Reineck, 1982) and as such, F3 and F4 are interpreted to be lateral equivalents of one another along an across-shelf transect; their origins are discussed in this context.

The presence of erosive-based, normally-graded, fine- to coarse-grained sandstones with no wave-generated structures (F3), suggests that sediment deposition occurred in response to events which initially produced bottom currents that were strong enough to partially erode the underlying beds; resulting in the formation of planar erosive contacts (Figure 4.6). In outcrop, coarse-grained, internal parallel lamina sets and normal grading are consistent with suspension settling from waning currents in a relatively proximal setting where significant volumes of sand-sized material were available (cf. Duke et al 1991). The

sedimentary features described in F3 strongly resemble those observed in modern storm-dominated shelf settings where large volumes of coarse-grained sediment are episodically discharged onto a narrow shelf (e.g., Eel shelf; Milliman and Syvitski 1992; Ogston et al., 2000).

The sedimentary features observed in current-rippled, normally-graded silt rich mudstones (F4), are interpreted as being the more distal equivalent of the F3 sandstones. Basal lamina sets in F4 (Figure 4.7) display unidirectional current-ripples composed of fine-silt to fine sand-sized grains that can be observed to downlap onto basal scour surfaces, while internal lamina sets display continuous, fining-upward planar laminations. No bioturbation is observed in the basal divisions of these beds, but sparse *Planolites* and *Gyrolithes*, can be observed towards the tops of beds. This succession of sedimentary and biogenic structures suggests current-dominated depositional processes that evolved from being erosion and traction-dominated, to suspension settling from a waning flow as the current subsides. The bioturbation observed near the tops of beds indicates that there is sufficient time between episodic sedimentation events for bed colonization by benthic organisms.

The bed evolution observed in F3 and F4 is broadly consistent with the bed stratigraphy deposited by a number of density-driven sediment gravity flow types including current-wave-enhanced sediment gravity flows (CWESGFs) (e.g., Macquaker et al., 2010; Denommee et al., *in prep.*), hyperpycnal flows (e.g., Mulder et al., 2013; Lamb and Mohrig, 2009), or turbidity currents. CWESGFs utilize the shear generated by near-bed currents and waves to initiate offshore sediment transport in muddy, low-gradient settings (Friedrichs and Wright, 2004) and deposit sedimentary fabrics that exhibit a diagnostic triplet motif that reflects: (1) turbulent traction transport sufficient to result in the erosion of underlying strata, overlain by (2) planar parallel laminae deposited during the laminar phase of flow, followed by (3) suspension setting as the flow wanes. This bed evolution is broadly consistent with the

sedimentary fabric evolution of F4 however, CWESGFs are unlikely to be observed in the Ordovician Power Steps Fm. CWESGFs require sufficient supply of (detritally-sourced) fluidized muds to transport sediment across shelf (Wright et al., 2001), this condition is not met in the Power Steps Fm. where the illite-dominated detrital clay-mineral fraction sourced from the Paleozoic hinterland is relatively small (Table 4.1). Although we cannot conclusively attribute the deposition of these density-driven current deposits to a specific mechanism it is likely, given the apparently steep gradient observed on the shelf (Figure 4.2), that they are the product of waning turbidity flows or hyperpycnal flows. The initiation of hyperpycnal turbidity currents requires a gradient of at least 0.7° (e.g., Wright et al., 2001; Bentley, 2003); this condition is easily met in the studied section.

4.5.1.2 Wave-Dominated Deposits

Medium-grained, cross-stratified wave-reworked sandstones (F1), re-worked, wave-rippled silt-rich mudstone (F5), wavy-discontinuous, normally-graded silt-rich mudstones with sand and clay (F6), and normally-graded, faintly-laminated silt-rich mudstone (F7), share sedimentary structures, grading relationships, and ichnological characteristics which suggest that they are the depositional product of storm-wave-generated oscillatory flow events. Superficially many of these beds appear analogous to turbidites, but they are distinguished from such deposits on the basis of the presence of diagnostic sedimentary structures including basal wave-ripple cross-lamination, trough cross-bedding, and undulating lower bounding surfaces. Storm-wave deposited sandstones tend to become thinner, less common and increasingly more finely grained, in an offshore direction (cf. Aigner and Reineck, 1982). As such, these vertically stacked facies are interpreted to be the lateral equivalents of one another along an across-shelf transect; their origins are discussed in this context.

The presence of laterally-continuous, medium-grained, cross-stratified and wave-reworked sandstones (F1) suggests that sediment deposition occurred in response to major storm events which appear to diminish in energy (e.g., towards a stratigraphically lower position) as indicated by a decrease in the thickness of sandstone beds and the mean grain-size of the beds as well as the increase in the intensity of bioturbation. The proximal-distal depositional trends, which were observed in F1 and F5, F6, and F7 of the studied section of the Power Steps Fm. at Ochre Cove can be summarized as dm-thick wave-dominated sandstones (F1), interbedded with dm-thick mudstones, grading into equally thick sandstone and mudstones interbeds, which then grade into thinner, more discrete and discontinuous sandstone beds within mudstone beds that increase in thickness as water depth increases laterally. The absence of thick sandstone beds within the more distal (stratigraphically lower) locations of the studied section indicates that the sand was not transported to the distal reaches of the clinothem, probably because the wave-induced turbulence was not sufficient to maintain the coarse-grained fraction in suspension due to deepening water and/or waning wave-orbital velocities in the bottom boundary layer.

4.5.1.3 Combined-Flow Deposits

Medium-grained, wave- and current- rippled-sandstones (F2) contain sedimentary structures, grading relationships, and ichnological characteristics that suggest that they are the depositional products of a combination of both unidirectional and oscillatory flow components (e.g., Myrow and Southard, 1991; Walker and Plint, 1992). Combined flow structures can be found in a number of marine environments including tidal flats, delta fronts, and the shallow shelf, among others (e.g., Grant and Madsen, 1979). Within the studied section combined flow structures are rare – having only been observed near sampling location BIC1327 (Figure 4.3). Within the Power Steps formation, sand-rich combined flow

ripples are exclusively observed in association with relatively thick fine-grained sediments belonging to F7, normally-graded, laminated silt-rich mudstones (Figure 4.5) which are interpreted as being the distal depositional product of oscillatory flow (see section 4.5.1.2). As the combined flow structures are relatively coarse-grained they would require more energy to be transported across the shelf, and as such they were probably deposited under more energetic conditions. It should be noted that a combined wave-current flow is more effective at sediment transport than the sum of its parts (e.g., Grant and Madsen, 1979).

4.5.2 Shelf Architecture and Depositional Environments

Paleodepositional environments within the Power Steps Fm. are defined on the basis of bounding surface geometry, diagnostic sedimentary fabrics, the relative aspect ratio of sandstone and mudstone beds, and relative change in sandstone and mudstone bed thickness down dip. Six distinct sedimentary packages are observed that are interpreted to represents four distinct shelf environments (Figure 4.2). The overall succession is interpreted as having been deposited as part of a prograding wave-dominated deltaic system; the hallmark of which is a coarsening upwards facies succession that documents the transition from offshore muds into shoreface sands (Bhattacharya, 2010), and is preserved in the studied section (Figure 4.3). Figure 4.13 presents a summary of the depositional environments and dominant sediment transport mechanisms discussed below.

Two sedimentary packages (4-9m and 39-42m stratigraphic height; Figure 4.3) within the studied section are interpreted as having been deposited in shallow shoreface settings. These sedimentary packages comprise sandstones of F1: medium-grained, cross-stratified, wave-rippled sandstones and F2: medium-grained, wave- and current-rippled sandstones interbedded with mudstones from F7: normally-graded, largely homogenous siliciclastic coarse mudstone. Also present are mudstones from F8: homogenous siliciclastic medium

mudstone; which was probably deposited during fair-weather conditions when river flooding was absent and represents background sedimentation. These three facies contain sedimentary structures that reflect deposition from rapidly decelerating unidirectional (i.e., F2) and oscillatory (i.e., F3 and F5) flows above fair weather wave base including wave and current ripples and m-scale cross-stratification (Figure 4.5b). The high sedimentation rates enhance the preservation of sedimentary structures. Bioturbation in the shoreface environment is sparse and in this case likely reflects the relatively high-energy setting and frequent reworking events.

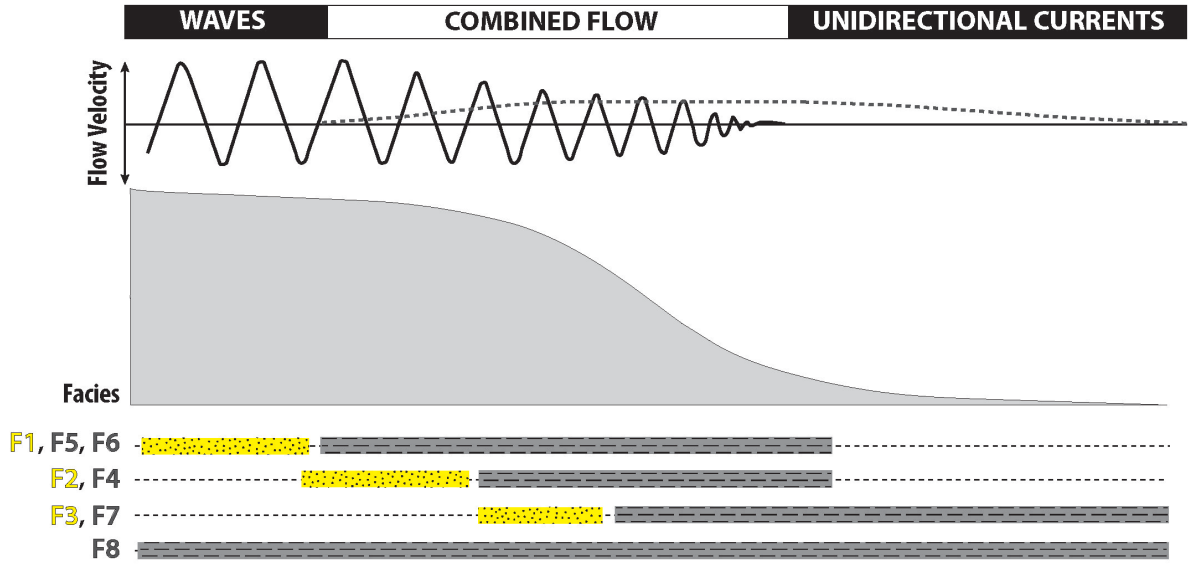

Figure 4.13 Schematic diagram illustrating the dominant processes responsible for sediment transport on the clinothem.

Two stratigraphic packages (4-9m and 27-39m stratigraphic height; Figure 4.3) within the studied section are interpreted as having been deposited in delta front (foreset) settings. These sedimentary packages comprise sandstones of F3: normally-graded, medium-grained sandstone with muddy tops and concretions, F4: current-ripple laminated, normally-graded, siliciclastic coarse mudstone, F5: wave-ripple laminated, normally-graded siliciclastic coarse mudstones, and F6: wave-rippled laminated, normally-graded siliciclastic medium mudstone.

One sedimentary package (20m-27m stratigraphic height; Figure 4.3) is interpreted as having been deposited in a prodelta (bottomset) setting. Here, sediments mostly belong to F7: normally-graded, largely homogenous medium mudstones. Traditional facies models have interpreted prodelta strata as being the depositional product of suspension settling however, it is being increasingly recognized that many prodelta mudstones contain density-driven current deposits.

The final sedimentary package (13-20m stratigraphic height; Figure 4.3) within the studied section is interpreted as having been deposited in an offshore setting and is composed primarily of mudstones belonging to F7: normally-graded, largely homogenous medium siliciclastic mudstone and F8: homogenous siliciclastic medium mudstone. In this setting erosional surfaces are mostly absent and there is less evidence for traction transport. Beds displaying normal grading were most likely the deposition product of suspension settling from waning flows in relatively deep water where flow velocities were insufficient to erode the underlying strata or support traction-dominated transport.

4.5.3 The Origin of Mud in the Power Steps Formation

In the studied section, most of the framework and matrix components likely represent detrital inputs sourced from Paleozoic hinterland. A small proportion of the sediment, although still a significant fraction of the clay-sized material observed in the mudstone facies, comprises the diagenetic alteration product of unstable mafic minerals (e.g., Figure 4.11) Petrographic and SEM analyses of the clay-rich units, as well as the cross-cutting relationships of cements indicate that mudstones were initially immature, most likely containing unstable olivine and pyroxenes sourced which preferentially alter to Fe-rich chlorite (chamosite) along with subangular silt-sized quartz grains, biotite and some

muscovite and plagioclase (e.g., Figure 4.11c; Table 4.1). The immature nature of the detrital input likely indicates that the sediment transport path was relatively short.

Significant vertical changes in the clay mineral assemblage are observed within the studied section (Figure 4.12). The shelf and shoreface environments in the lower portion of the studied section (4-13m stratigraphic height; Figure 4.2) have a clay mineral assemblage with a high chlorite to illite ratio, where chlorite can represent more than 70 wt.% of the clay-sized materials (Figure 4.12). This probably reflects relatively high inputs of detrital chlorite grains clay and unstable mafic detritus that is easily chloritized to the shelf during the times that these units were deposited.

Above 13m stratigraphic height, where a major flooding surface is observed, there is a coincident change observed in the chlorite: illite ratio (Figure 4.12). Because the shift in the chlorite to illite ratio is accompanied by an increase in overall clay content within the sedimentary strata (Figure 4.12) and an increase in the ratio of mudstone to sandstone beds (Figure 4.3) it is likely that the hydrodynamic sorting of grains with increasing water depth was an important control on shelf architecture. It is likely that this deepening event resulted in hydraulic sorting along the dispersal path that precluded the coarser-grained mafic grains that preferentially alter to Fe-rich chlorite from being transported and deposited on the distal regions of the shelf. It should be noted that the chlorite: illite ratio appears to be increasing in the shoreface/topset sediments at the top of the studied section. Previous studies of the underlying Tremadocian Bell Island Group strata belonging to the Beach and Redmans Fms. (e.g., Harazim and McIlroy, 2015; Miller and McIlroy, 2015) have suggested that autocyclic changes in the supply of silt- and sand-sized detrital sediments played a leading role in controlling both changes in mineralogy and stratigraphy. The same does not appear to be the case within the Power Steps Fm. where sedimentological and mineralogical trends can, for the most part, be satisfactorily explained in terms of relative sea level changes.

4.6 Conclusions

1. The facies architecture of Power Step Fm. exposure at Ochre Cove can be genetically linked to (1) pulsed (episodic) sediment input, (2) sediment dispersal pattern driven by storm waves and unidirectional currents, and (3) relative grain stability during burial and diagenesis. Autocyclic changes in the supply of silt- and sand-sized detrital sediments are not necessary to explain the observed sedimentological and mineralogical trends.

2. Detailed facies analysis reveals that storm-driven event flows were the primary mechanisms for fine-grained sediment in the Power Steps Formation exposed at Ochre Cove, Bell Island Newfoundland. Both unidirectional, oscillatory, and combined flow types contributed to the pulsed sedimentation that built much of the shelf. This interpretation contrasts with previous models of sediment dispersal that attributed the deposition of the interbedded sands and muds to tidal processes.

3. Sediment transport on the different architectural elements of the muddy shelf clinothem (i.e., the shoreface (topset), muddy delta front (foresets), prodelta (bottomsets), and offshore environments) is driven by different mechanisms that reflect local hydrodynamic conditions. Figure 4.13 presents a summary of these processes and their depositional products. On the most proximal regions of the shelf clinothem, wave-processes capable of transporting relatively coarse-grained sediment dominate. As you move further seaward, currents play an increasingly important role in sediment transport – and the combined energies of waves and currents are capable of transporting relatively coarse-grained sediments when wave-orbital velocities alone are insufficient. On the clinothem foresets and bottomsets, muddy facies which are the distal equivalents of the more proximal shoreface facies dominate the stratigraphy while on the most distal, offshore regions of the clinothem muddy sedimentary

facies interpreted as being the distal products of muddy sediment-gravity type flows dominate. This succession of facies can be used to interpret paleo-depositional environment, hydrodynamic conditions on the shelf, and relative water depth.

4. A portion of the present-day clay mineral fraction represents the alteration product of highly unstable mafic (lithic) grains that were delivered to the shelf as silt-sized particles where they formed a fraction of the framework components. These lithic fragments were diagenetically alerted to chlorite before significant compaction occurred. It is important to consider this fraction of the chlorite in the rocks separately from detrital chlorite when using clay mineralogy as a proxy for provenance.

4.7 Acknowledgements

This work was supported by the Billy and Anne Harrison endowment for sedimentary geology (SJB) and by student research grants from the American Association of Petroleum Geologists (AAPG), the Geological Society of America (GSA), and the Society for Sedimentary Geology (SEPM) awarded to KCD. Babatunde Olanipekun (Memorial University of Newfoundland) is thanked for his assistance with sample collection and field photography. Rick Young (Louisiana State University) is thanked for his assistance with hand specimen preparation and Wanda LeBlanc (Louisiana State University) is thanked for performing all QXRD analyses.

4.8 References

Aigner, T., and Reineck, H.-E., 1982, Proximality trends in modern storm sands from the helgoland bight (north sea) and their implications for basin analysis: Senckenbergiana maritima, v. 14, no. 5-6, p. 183-215.

Aplin, A. C., and Macquaker, J. H. S., 2011, Mudstone diversity: Origin and implications for source, seal, and reservoir properties in petroleum systems: Aapg Bulletin, v. 95, no. 12, p. 2031-2059.

Baas, J.H., Best, J.L., and Peakall, J., 2011, Depositional processes, bedform development and hybrid bed formation in rapidly decelerated cohesive (mud–sand) sediment flows: Sedimentology, v. 58, p. 1953-1987.

Bentley, S.J., Sheremet, A., and Jaeger, J.M., 2006, Event sedimentation, bioturbation, and preserved sedimentary fabric: Field and model comparisons in three contrastic marine settings: Continental Shelf Research, v. 26, p.2108-2124.

Bhattacharya, J. P., and MacEachern, J. A., 2009, Hyperpycnal rivers and prodeltaic shelves in the Cretaceous Seaway of North America: Journal of Sedimentary Research, v. 79, no. 3-4, p. 184-209.

Boggs, S., 2006, Principles of sedimentology and stratigraphy: Pearson Education: Inc., Upper Saddle River, New Jersey.

Bruckner, W. D., 1969, Geology of Eastern Part of Avalon Peninsula, Newfoundland - A Summary, M 12: North Atlantic: Geology and Continental Drift, p. 130-138.

Cattaneo, A., Correggiari, A., Langone, L., and Trincardi, F., 2003, The late-Holocene Gargano subaqueous delta, Adriatic shelf: Sediment pathways and supply fluctuations: Marine Geology, v. 193, no. 1–2, p. 61-91.

Cattaneo, A., Trincardi, F., Asioli, A., and Correggiari, A., 2007, The Western Adriatic shelf clinoform: energy-limited bottomset: Continental Shelf Research, v. 27, no. 3–4, p. 506-525.

Cheel, R.J., 1991, Grain fabric in hummocky cross-stratified storm bends: Genetic implications: Journal of Sedimentary Research, v. 61, no. 1, p., 102-110.

Clifton, H.E., 2006, A reexamination of facies models for clastic shorelines, in Posamentier, H.W., and Walker, R.G., eds., Facies Models Revisited: SEPM, Special Publication 84, p. 293-339.

Cocks, L. R. M., and Torsvik, T. H., 2002, Earth geography from 500 to 400 million years ago: a faunal and palaeomagnetic review: Journal of the Geological Society, v. 159, no. 6, p. 631-644.

Curtin, T. B., 1986, Physical observations in the plume region of the Amazon River during peak discharge—II. Water masses: Continental Shelf Research, v. 6, no. 1–2, p. 53-71.

Denommee, K.C., Bentley, S.J., Harazim, D., and Macquaker, J.H.S., *in prep*, Hydrodynamic controls on muddy sedimentary fabric development: Atchafalaya Chenier Plain subaqueous delta.

Denommee, K. C., 2015, Developping Recognition Criteria for Current-Wave-Enhanced Sediment Gravity Flows [PhD] Lousiana State University. 148 p.

Duke, W. L., Arnott, R., and Cheel, R. J., 1991, Shelf sandstones and hummocky cross-stratification: New insights on a stormy debate: Geology, v. 19, no. 6, p. 625-628.

Friedrichs, C.T., Wright, L.D., 2004. Gravity-driven sediment transport on the continental shelfimplications for equilibrium profiles near river mouths. Coastal Engineering 51, 795-811.

Ghadeer, S. G., and Macquaker, J. H. S., 2011, Sediment transport processes in an ancient mud-dominated succession: a comparison of processes operating in marine offshore settings and anoxic basinal environments: Journal of the Geological Society, v. 168, no. 5, p. 1121-1132.

Grant, W.D., and Madsen, O.S., 1986, the continental-shelf bottom boundary layer: Annual Review of Fluid Mechanics, v. 18, p. 265–305.

Harazim, D., and McIlroy, D., 2015, Mud-Rich Density-Driven Flows Along an Early Ordovician Storm-Dominated Shoreline: Implications for Shallow-Marine Facies Models: Journal of Sedimentary Research, v. 85, no. 5, p. 509-528.

Kuehl, S. A., Nittrouer, C. A., and Demaster, D. J., 1988, Microfabric Study of Fine-Grained Sediments - Observations from the Amazon Subaqueous Delta: Journal of Sedimentary Petrology, v. 58, no. 1, p. 12-23.

Lazar, O.R., Bohacs, K.M., Macquaker, J.H.S., Schieber, J., and Demko, T.M., 2015, Integrated approach for the nomenclature and description of the spectrum of fine-grained sedimentary rocks. Journal of Sedimentary Research, v. 85, p. 230-246.

Lamb, M. P., and Mohrig, D., 2009, Do hyperpycnal-flow deposits record river-flood dynamics?: Geology, v. 37, no. 12, p. 1067-1070.

MacEachern, J.A. , Pemberton, S.G., Gingras, M.K., and Bann, K.L., 2010, Ichnology and Facies Models, *in* Dalrymple, R.W., and James, N.P., eds., Facies Models, edition 3: Geological Association of Canada, St. John's Newfoundland, p. 19-58.

Macquaker, J. H. S., and Bohacs, K. M., 2007, Geology - on the accumulation of mud: Science, v. 318, no. 5857, p. 1734-1735.

Macquaker, J. H. S., Bentley, S. J., and Bohacs, K. M., 2010, Wave-enhanced sediment-gravity flows and mud dispersal across continental shelves: Reappraising sediment transport processes operating in ancient mudstone successions: Geology, v. 38, no. 10, p. 947-950.

Miller, H. G., 1983, A geophysical interpretation of the geology of Conception Bay, Newfoundland: Canadian Journal of Earth Sciences, v. 20, no. 9, p. 1421-1433.

Milliman, J. D., and Syvitski, J. P., 1992, Geomorphic/tectonic control of sediment discharge to the ocean: The importance of small mountainous rivers: The Journal of Geology, p. 525-544.

Moore, D. M., and Reynolds, R. C. J., 1997, X-Ray Diffraction and the Identification and Analysis of Clay Minerals, New York, Oxford University Press, 378 p.

Mulder, T., Syvitski, J. P., Migeon, S., Faugeres, J.-C., and Savoye, B., 2003, Marine hyperpycnal flows: Initiation, behavior and related deposits. A review: Marine and Petroleum Geology, v. 20, no. 6, p. 861-882.

Myrow, P.M. and Southard, J.B., 1991, Combined-flow model for vertical stratification sequences in shall marine storm-deposited beds, Journal of Sedimentary Petrology, v. 9, p. 202-210.

Neill, C. F., and Allison, M. A., 2005, Subaqueous deltaic formation on the Atchafalaya Shelf, Louisiana: Marine Geology, v. 214, no. 4, p. 411-430.

Ogston, A.S., Cacchione, D.A, Sternberg, R.W, and Kineke, G.C., 2000, Observations of storm and river flood-driven sediment transport on the northern California continental shelf, Continental Shelf Research, v. 20, no. 16, p. 2141-2162.

Passey, Q. R., Bohacs, K., Esch, W. L., Klimentidis, R., and Sinha, S., 2010, From Oil-Prone Source Rock to Gas-Producing Shale Reservoir - Geologic and Petrophysical Characterization of Unconventional Shale Gas Reservoirs, Society of Petroleum Engineers.

Patruno, S., Hampson, G. J., and Jackson, C. A. L., 2015, Quantitative characterisation of deltaic and subaqueous clinoforms: Earth-Science Reviews, v. 142, no. 0, p. 79-119.

Perillo, M.M., Best, J.L., and Garcia, M.H., 2014, A new phase diagram for combined-flow bedforms: Journal of Sedimentary Research, v. 84, p. 301-313.

Petschick, R., 2001, MacDiff, freeware scientific graphical analysis software for X-ray diffration profiles: Frankfurt, Germany.

Pettijohn, F., 1975, Sedimentary Rocks. Harper and Row Publishers: New York.

Plint, A.G., 2010, Chapter 8, Wave- and storm-dominated shoreline and shallow marine systems. In: Facies Models, 4th Edition, Dalrymple, R.W. and James, N.P., eds. Geological Association of Canada, p. 167-199.

Plint, G.A., Macquaker J.H.S. and Varban, B., 2012, Bedload transport of mud across a wide, storm-influenced ramp: Cenomanian–Turonian Kaskapau Formation, Western Canada Foreland Basin: Journal of Sedimentary Research, v. 82, p. 801-822.

Plint, A. G., 2014, Mud dispersal across a Cretaceous prodelta: Storm-generated, wave-enhanced sediment gravity flows inferred from mudstone microtexture and microfacies: Sedimentology, v. 61, no. 3, p. 609-647.

Poppe, L. J., Paskevich, V. F., Hathaway, J. C., and Blackwood, D. S., 2001, A Laboratory Manual for X-Ray Powder Diffraction, United States Geological Survey.

Potter, P. E., Maynard, J.B., and Depetris, P.J., 2005, Mud and Mudstones: Introduction and Overview: Springer, 297p.

Ranger, M.J., 1979, The stratigraphy and depositional environment of the Bell Island Group, the Wabana Group, and the Wabana iron ores, of Conception Bay, Newfoundland. Unpublished M.Sc. thesis, Memorial University of Newfoundland, 216 p.

Ranger, M. J., Pickerill, R. K., and Fillion, D., 1984, Lithostratigraphy of the Cambrian - Lower-Ordovician - Bell Island and Wabana Groups of Bell, Little-Bell, and Kellys Islands, Conception Bay, Eastern Newfoundland: Canadian Journal of Earth Sciences, v. 21, no. 11, p. 1245-1261.

Rotondo, K., and Bentley, S. J., 2003, Deposition and Resuspension of Fluid Mud on the Western Louisiana Inner Shelf:: Gulf Coast Association of Geological Societies Transactions, v. 53, p. 722-731.

Schieber, J., 1994, Evidence for High-Energy Events and Shallow-Water Deposition in the Chattanooga Shale, Devonian, Central Tennessee, USA: Sedimentary Geology, v. 93, no. 3-4, p. 193-208.

Schieber, J., 1999, Distribution and deposition of mudstone facies in the Upper Devonian Sonyea Group of New York: Journal of Sedimentary Research, v. 69, no. 4, p. 909-925.

Schieber, J., 2007, Oxydation of Detrital Pyrite as a Cause for Marcasite Formation in Marine Lag Deposits from the Devonian of the Eastern US. Deep Sea Research II, v. 54, p. 1312-1326.

Stampfli, G. M., von Raumer, J. F., and Borel, G. D., 2002, Paleozoic evolution of pre-variscan terranes: From gondwana to the variscan collision: Special Papers-Geological Society of America, p. 263-280.

Talling, P. J., Masson, D. G., Sumner, E. J., and Malgesini, G., 2012, Subaqueous sediment density flows: Depositional processes and deposit types: Sedimentology, v. 59, no. 7, p. 1937-2003.

Taylor, A.M., Goldring, R., 1993. Description and analysis of bioturbation and ichnofabric. Journal of the Geological Society 150, 141-148.

Walker, R.G., and Plint, A.G., 1992, Wave- and storm-dominated shallow marine systems, *in* Walker, R.G., and James, N.P., eds., Facies Models: Geological Association of Canada, p. 219-238.

Wheatcroft, R. A., 2000, Oceanic flood sedimentation: a new perspective: Continental Shelf Research, v. 20, no. 16, p. 2059-2066.

Wheatcroft, R.A. and Drake, D.E., 2003, Post-depositional alteration and preservation of sedimentary event layers on continental margins, I. The role of episodic sedimentation: Marine Geology, v. 199, p. 123-137.

Wright, L. D., Friedrichs, C. T., Kim, S. C., and Scully, M. E., 2001, Effects of ambient currents and waves on gravity-driven sediment transport on continental shelves: Marine Geology, v. 175, no. 1–4, p. 25-45.

CHAPTER 5: CONCLUSIONS

5.1 Significance of Research

Significant advances regarding the transport of mud in the marine realm over the last ~20 years have highlighted the importance of fluid muds (e.g., WESGFs and CWESGFs) as a mechanism for the offshore transport of muddy sediment on modern continental shelves. Although the across-shelf transport of fluid muds in ancient sedimentary successions is likely a common feature (e.g., Macquaker et al., 2010), the application of fluid mud hydrodynamic theory to the rock record has, to date, been limited (e.g., Ichaso and Dalrymple, 2009; Macquaker et al., 2010; Plint, 2014). The difficulties in applying learning from modern observations to the rock record arise for several reasons. Firstly, the range of environmental conditions conducive for fluid mud development is not yet fully catalogued in modern settings. Secondly, criteria for recognizing the sedimentary products of these flows have only recently begun to have been developed (e.g., Macquaker et al., 2010; this dissertation). Finally, evidence for fluid transport in mudstones (e.g., ripples, downlap surfaces, etc.) is difficult to observe, and requires investigation across several scales including careful thin section examination.

This dissertation investigated the processes responsible for the dispersal, deposition, and accumulation of muddy sediments in high-energy, shallow-marine settings with the goal of better understanding of how fluid muds influence across-shelf sediment transport and what their sedimentary products look like. Not only is having a better understanding of how fine-grained sediments are deposited and incorporated into the rock record of scientific interest, but this improved understanding is of significant economic value as it will lead to a better understanding of mudstone facies variability, which will in turn enhance our ability to better develop the resources hosted within these deposits.

Chapter 2: *Across-Shelf Clinothem Dynamics on the Southwest Louisiana Chenier Plain Inner Shelf.* This study examined the mechanisms of clinothem progradation on the low-gradient Southwest Louisiana Chenier Plain inner shelf, demonstrating that in addition to acting as a mechanism capable of dispersing sediments across low-gradient shelves,

CWESGFs play a key role in generating seabed conditions (high-porosity, rapidly-deposited, gas-charged sediments) that are conducive to mass-wasting. This demonstrates that CWESGFs affect the shelf environment in complex ways that have yet to be described in existing facies models or shelf-building numerical simulations. Although the study area is a relatively small system, the features observed here are similar to the much larger Mississippi River delta and so are likely to be found in other systems, both modern and ancient.

Chapter 3: *Hydrodynamic Controls on Muddy Sedimentary Fabric Development: Atchafalaya Chenier Plain Subaqueous Delta*. This study examines the sedimentary products of current-wave-enhanced sediment gravity flows (CWESGFs) on the muddy Southwest Louisiana Chenier Plain inner shelf where the combined effects of currents, gravity, and wave orbital velocity exert a strong control on sedimentary fabric development. The results of this study show that in addition to the relative contribution of each of the velocity terms u_c, u_g, and u_w, wave period exerts a strong control on CWESGF sedimentary fabric development. Additionally, the analytical approach presented here (observed fabric plotted together with measured hydrodynamic conditions represented in Figure 3.14) provides a semi-quantitative framework by which relationships among CWESGF formative conditions (i.e., u_c, u_g, u_w and wave period) and diagnostic sedimentary fabric recognition criteria may be further studied in the future (Figure 5.1).

Chapter 4: *Anatomy of an Early Ordovician Storm-Dominated Muddy Clinothem: Implications for Across-Shelf Facies Variability*. This study examined the mechanisms of sediment transport and clinothem progradation on a muddy, Ordovician shelf. It was determined, that contrary to previous interpretations which attributed sediment dispersal to tidal processes, that the muddy succession belonging to the Power Steps Formation was deposited primarily under the influence of episodic, storm-wave-driven flows. While no CWESGF sedimentary structures were identified in this interval, there is still significant

evidence for the offshore transport of muddy sediments in an energetic setting. As the Power Steps Formation is an Ordovician deposit, the origin of the muddy sediments is significantly different than the origin of the muddy sediments observed on the modern SWLA Chenier Plain. Fundamental differences between the two sediment types in terms of particle reactivity, density, maturity, effective grains size and clay mineral fraction may explain some of the variations we see in this succession as compared to modern analogues.

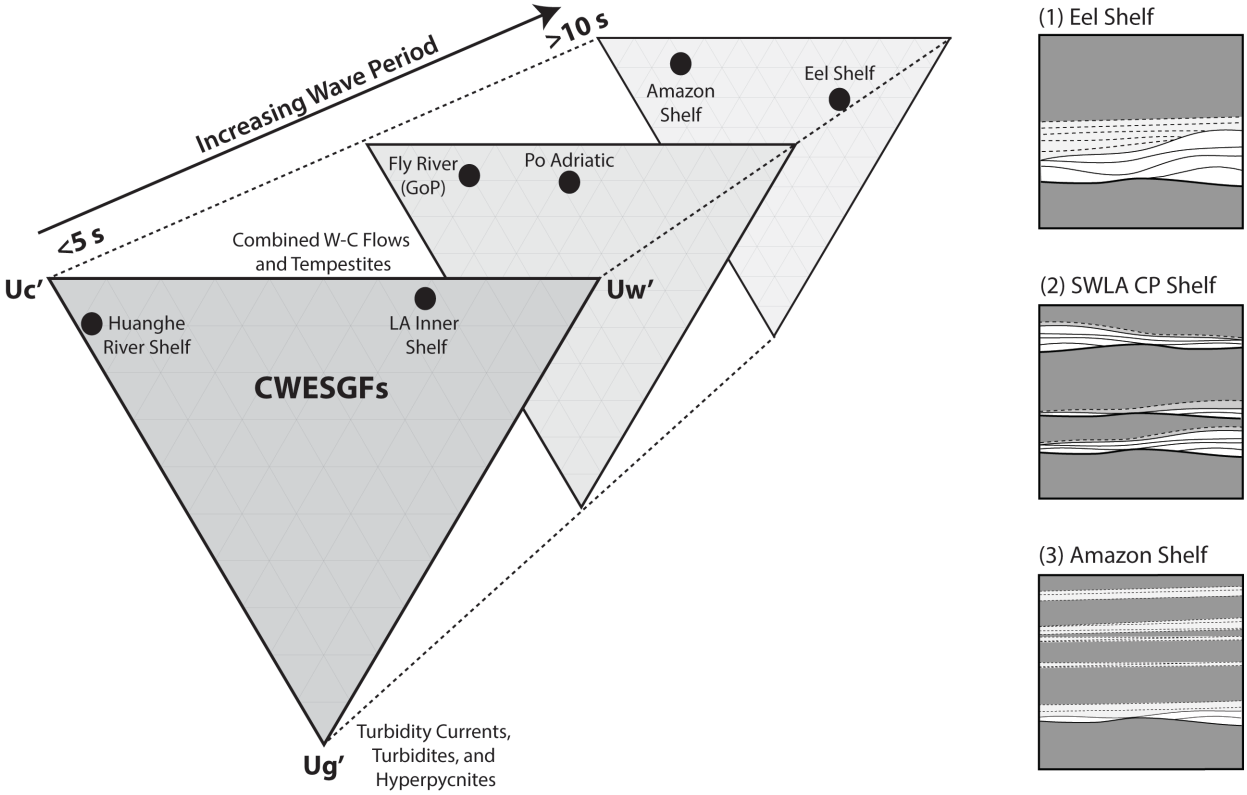

Figure 5.1 Diagram representing the potential spectrum of CWESGF fabrics. Locations where CWESGFs have been documented have been quantitatively plotted on this diagram by determining the relative contributions of each of the velocity terms contributing to the development of CWESGFs as well as the dominant wave period: SWLA (Wright et al., 2001); Eel Shelf (Wright et al., 2001); Huanghe River Delta (Wright et al., 2001); Po River Delta (Traykovski et al., 2007; Fain et al., 2005); Amazon River Delta (Curtin et al., 1986; Kuehl et al., 1988); and the Fly River Delta (Walsh et al., 2004; Martin et al., 2008) . Conceptualized diagrams of the sedimentary products of these environments are included for selected locations.

5.2 Avenues for Future Research

In order to further bridge the gap in our understanding of transport of mud in the marine realm and the strata produced over geologic timescales it is necessary to grow the catalogue of modern examples of sedimentary fabrics on low-gradient, high-energy muddy shelves – further populating the CWESGF sedimentary fabric ternary diagram (Figure 5.1). Additionally, in order to conclusively link these fabrics to their rock record counterparts it will be necessary to quantitatively evaluate how these fabrics are preserved, both in terms of their microstratigraphy, but also over larger stratal scales that are likely to result from interacting sedimentation, bioturbation and early diagenesis. Finally, applying these learnings to ancient sedimentary successions where they may be used to refine paleo-environmental models as well as to better understand the rock properties which develop as a direct function of sedimentary depositional mechanisms.

5.3 References

Ichaso, A. A., and Dalrymple, R. W., 2009, Tide- and wave-generated fluid mud deposits in the tilje formation (jurassic), offshore norway: Geology, v. 37, no. 6, p. 539-542.

Macquaker, J. H. S., Bentley, S. J., and Bohacs, K. M., 2010, Wave-enhanced sediment-gravity flows and mud dispersal across continental shelves: Reappraising sediment transport processes operating in ancient mudstone successions: Geology, v. 38, no. 10, p. 947-950.

Plint, A. G., 2014, Mud dispersal across a cretaceous prodelta: Storm-generated, wave-enhanced sediment gravity flows inferred from mudstone microtexture and microfacies: Sedimentology, v. 61, no. 3, p. 609-647.

APPENDIX A: MULTICORING LOCATIONS

Sampling Program: CP10.12

Coring Location	Latitude	Longitude
CP10.12 2	29 32.019N	92 26.595W
CP10.12 3	29 31.488N	92 26.711W
CP10.12 4	29 30.922N	92 26.854W
CP10.12 5	20 30.429N	92 26.968W
CP10.12 6	20 30.926N	92 26.845W
CP10.12 7	29 29.352N	92 27.217W
CP10.12 8	29 28.839N	92 27.339W
CP10.12 9	29 28.290N	92 27.454W

Sampling Program: CP8.14

Coring Location	Latitude	Longitude
CP8.14 2	29 32.036N	92 26.562W
CP8.14 3	29 31.462N	92 26.562W
CP8.14 4	29 30.918N	92 26.839W
CP8.14 5	29 30.432N	92 26.915W
CP8.14 6	29 29.885N	92 27.038W
CP8.14 7	29 29.353N	92 27.205W
CP8.14 8	29 28.812N	92 27.335W

APPENDIX B: RADIOCHEMISTRY RESULTS

Core: CP10.12 2

Depth Interval (cm)	$^{210}Pb_{Total}$ Activity (dpm/g)	$^{210}Pb_{XS}$ Activity (dpm/g)	$^{210}Pb_{XS}$ Error (dpm/g)	^{137}Cs Activity (dpm/g)	^{137}Cs Error (dpm/g)
0-1	5.13	3.24	0.24	0.14	0.04
1-2	4.93	3.26	0.21	0.28	0.04
2-3	6.09	4.44	0.28	0.22	0.04
3-4	20.82	13.92	0.79	0.49	0.14
4-5	5.86	3.89	0.23	0.16	0.04
5-6	6.44	5.00	0.25	0.27	0.04
6-7	6.25	4.67	0.25	0.26	0.04
7-8	6.38	5.08	0.27	0.26	0.05
8-9	5.89	4.61	0.26	0.23	0.04
9-10	6.15	4.49	0.25	0.25	0.05
10-12	6.35	4.66	0.21	0.22	0.03
12-14	5.94	4.23	0.21	0.26	0.04
14-16	6.27	5.10	0.27	0.29	0.04
16-18	6.26	4.87	0.24	0.16	0.04
18-20	6.00	4.42	0.23	0.26	0.04
20-22	7.02	5.66	0.28	0.20	0.05
22-24	7.43	5.74	0.26	0.23	0.04
24-26	6.09	4.30	0.23	0.25	0.05
26-28	7.65	6.04	0.30	0.22	0.05
28-30	6.72	5.41	0.27	0.28	0.05

Core: CP10.12 3

Depth Interval (cm)	$^{210}Pb_{Total}$ Activity (dpm/g)	$^{210}Pb_{XS}$ Activity (dpm/g)	$^{210}Pb_{XS}$ Error (dpm/g)	^{137}Cs Activity (dpm/g)	^{137}Cs Error (dpm/g)
0-1	6.78	4.94	0.32	0.25	0.06
1-2	4.72	3.03	0.22	0.20	0.04
2-3	5.23	3.53	0.22	0.00	0.00
3-4	6.22	4.57	0.29	0.29	0.05
4-5	5.46	3.89	0.25	0.18	0.04
5-6	5.65	4.11	0.25	0.20	0.04
6-7	5.38	3.94	0.25	0.14	0.04
7-8	5.00	3.58	0.24	0.23	0.05
8-9	5.27	3.80	0.24	0.23	0.04
9-10	6.08	4.60	0.28	0.26	0.05
10-12	5.32	4.19	0.27	0.23	0.04
12-14	5.99	4.59	0.24	0.15	0.04
14-16	5.60	4.09	0.25	0.20	0.04
16-18	5.82	4.71	0.25	0.18	0.04
18-20	6.21	4.74	0.29	0.21	0.04
20-22	5.30	4.07	0.24	0.21	0.04
22-24	5.88	4.56	0.28	0.20	0.04
24-26	6.26	4.69	0.25	0.27	0.04
26-28	5.63	4.02	0.24	0.11	0.04
28-30	--	--	--	--	--
30-32	5.71	4.07	0.24	0.11	0.04
32-34	6.05	4.55	0.27	0.19	0.04
34-36	6.13	4.51	0.25	0.21	0.05

Core: CP10.12 4

Depth Interval (cm)	$^{210}Pb_{Total}$ Activity (dpm/g)	$^{210}Pb_{XS}$ Activity (dpm/g)	$^{210}Pb_{XS}$ Error (dpm/g)	^{137}Cs Activity (dpm/g)	^{137}Cs Error (dpm/g)
0-1	6.19	4.42	0.36	0.27	0.08
1-2	7.43	5.74	0.40	0.24	0.07
2-3	6.71	5.04	0.34	0.22	0.07
3-4	7.04	5.82	0.35	0.27	0.06
4-5	7.15	5.55	0.36	0.26	0.07
5-6	6.33	4.91	0.31	0.20	0.06
6-7	7.06	5.73	0.29	0.22	0.05
7-8	6.40	4.77	0.23	0.31	0.04
8-9	6.71	5.56	0.27	0.20	0.04
9-10	6.66	4.94	0.25	0.29	0.05
10-12	6.27	4.54	0.23	0.19	0.04
12-14	--	--	--	--	--
14-16	7.09	5.29	0.25	0.18	0.04
16-18	7.41	5.68	0.26	0.22	0.04
18-20	6.68	5.08	0.26	0.31	0.05
20-22	7.14	5.57	0.28	0.28	0.04
22-24	6.77	5.17	0.26	0.29	0.05
24-26	6.31	4.80	0.23	0.21	0.04
26-28	--	--	--	--	--
28-30	5.97	4.34	0.22	0.26	0.04
30-32	--	--	--	--	--
32-34	--	--	--	--	--
34-36	6.44	4.76	0.25	0.26	0.05
36-38	--	--	--	--	--
38-40	6.26	5.03	0.27	0.15	0.04
40-42	6.21	4.63	0.24	0.22	0.04
42-44	--	--	--	--	--
44-46	6.05	4.36	0.23	0.28	0.04

Core: CP10.12 5

Depth Interval (cm)	$^{210}Pb_{Total}$ Activity (dpm/g)	$^{210}Pb_{XS}$ Activity (dpm/g)	$^{210}Pb_{XS}$ Error (dpm/g)	^{137}Cs Activity (dpm/g)	^{137}Cs Error (dpm/g)
0-1	7.09	4.76	0.43	0.22	0.08
1-2	5.77	4.11	0.32	0.17	0.06
2-3	6.45	4.44	0.36	0.22	0.08
3-4	7.39	5.62	0.40	0.19	0.07
4-5	6.44	4.50	0.33	0.25	0.07
5-6	5.40	3.90	0.34	0.19	0.06
6-7	6.48	4.54	0.27	0.24	0.06
7-8	6.46	4.48	0.30	0.12	0.06
8-9	6.19	4.79	0.32	0.23	0.06
9-10	7.39	5.89	0.36	0.20	0.07
10-12	6.79	5.30	0.31	0.22	0.05
12-14	6.52	4.47	0.29	0.34	0.07
14-16	6.34	4.64	0.30	0.21	0.06
16-18	6.75	4.79	0.26	0.31	0.06
18-20	7.13	5.67	0.33	0.30	0.06
20-22	--	--	--	--	--
22-24	7.55	6.00	0.31	0.31	0.05
24-26	--	--	--	--	--
26-28	7.03	5.08	0.31	0.19	0.06
28-30	7.67	6.09	0.31	0.26	0.05
30-32	--	--	--	--	--
32-34	6.69	4.84	0.30	0.22	0.06

Core: CP10.12 6

Depth Interval (cm)	$^{210}Pb_{Total}$ Activity (dpm/g)	$^{210}Pb_{XS}$ Activity (dpm/g)	$^{210}Pb_{XS}$ Error (dpm/g)	^{137}Cs Activity (dpm/g)	^{137}Cs Error (dpm/g)
0-1	5.98	4.22	0.42	0.24	0.08
1-2	5.34	4.32	0.37	0.17	0.06
2-3	6.12	4.52	0.38	0.05	0.05
3-4	5.13	3.54	0.32	0.00	0.00
4-5	5.82	4.57	0.37	0.33	0.06
5-6	6.19	4.99	0.30	0.31	0.04
6-7	5.46	4.06	0.28	0.26	0.04
7-8	5.57	4.18	0.26	0.30	0.04
8-9	5.67	4.30	0.33	0.04	0.04
9-10	5.13	3.75	0.27	0.02	0.03
10-12	5.63	4.25	0.27	0.24	0.04
12-14	6.14	4.88	0.31	0.00	0.00
14-16	5.86	4.88	0.30	0.00	0.00
16-18	6.15	4.83	0.28	0.19	0.04
18-20	5.72	4.25	0.27	0.32	0.05
20-22	6.02	4.67	0.31	0.20	0.05
22-24	6.05	5.15	0.39	0.21	0.05
24-26	--	--	--	--	--
26-28	5.79	4.36	0.31	0.24	0.05

Core: CP10.12 7

Depth Interval (cm)	$^{210}Pb_{Total}$ Activity (dpm/g)	$^{210}Pb_{XS}$ Activity (dpm/g)	$^{210}Pb_{XS}$ Error (dpm/g)	^{137}Cs Activity (dpm/g)	^{137}Cs Error (dpm/g)
0-1	6.86	5.30	0.31	0.15	0.04
1-2	--	--	--	--	--
2-3	6.18	4.46	0.25	0.31	0.05
3-4	6.30	4.92	0.27	0.30	0.05
4-5	7.27	5.62	0.32	0.40	0.07
5-6	7.23	5.56	0.30	0.36	0.06
6-7	6.95	5.12	0.26	0.18	0.05
7-8	6.83	5.13	0.27	0.23	0.05
8-9	6.56	4.79	0.24	0.26	0.04
9-10	--	--	--	--	--
10-12	6.01	4.82	0.26	0.32	0.05
12-14	6.49	4.75	0.27	0.31	0.06
14-16	--	--	--	--	--
16-18	7.29	5.69	0.28	0.23	0.05
18-20	6.57	5.32	0.27	0.21	0.04
20-22	--	--	--	--	--
22-24	6.88	5.51	0.30	0.19	0.05
24-26	6.80	5.21	0.25	0.25	0.04
26-28	7.42	5.87	0.29	0.22	0.05
28-30	7.30	6.06	0.29	0.28	0.04
30-32	--	--	--	--	--
32-34	6.60	5.26	0.27	0.32	0.04
34-36	--	--	--	--	--
36-38	6.11	4.81	0.26	0.28	0.05

Core: CP10.12 8

Depth Interval (cm)	$^{210}Pb_{Total}$ Activity (dpm/g)	$^{210}Pb_{XS}$ Activity (dpm/g)	$^{210}Pb_{XS}$ Error (dpm/g)	^{137}Cs Activity (dpm/g)	^{137}Cs Error (dpm/g)
0-1	4.20	2.96	0.26	0.00	0.00
1-2	4.49	3.47	0.29	0.00	0.00
2-3	4.53	3.24	0.23	0.13	0.05
3-4	4.46	3.23	0.25	0.12	0.05
4-5	4.12	2.88	0.21	0.16	0.04
5-6	4.34	3.42	0.23	0.09	0.04
6-7	4.37	3.30	0.20	0.15	0.03
7-8	4.47	3.15	0.19	0.15	0.03
8-9	4.33	3.35	0.21	0.00	0.00
9-10	4.03	2.80	0.17	0.11	0.03
10-12	4.14	3.21	0.20	0.13	0.03
12-14	4.38	3.51	0.23	0.16	0.04
14-16	4.30	3.38	0.21	0.10	0.03
16-18	4.41	3.16	0.20	0.14	0.04
18-20	3.89	2.71	0.18	0.12	0.04
20-22	3.69	2.54	0.17	0.13	0.03
22-24	3.78	2.62	0.18	0.18	0.04
24-26	4.02	3.15	0.22	0.19	0.04
26-28	3.68	2.74	0.20	0.08	0.04
28-30	3.26	1.95	0.18	0.00	0.00
30-32	2.98	1.81	0.18	0.00	0.00
32-34	4.04	2.87	0.19	0.16	0.04
34-36	3.36	2.09	0.16	0.12	0.04
36-38	3.32	2.21	0.19	0.13	0.04
38-40	4.07	2.75	0.18	0.09	0.04
40-42	3.50	2.47	0.20	0.10	0.04

Core: CP10.12 9

Depth Interval (cm)	$^{210}Pb_{Total}$ Activity (dpm/g)	$^{210}Pb_{XS}$ Activity (dpm/g)	$^{210}Pb_{XS}$ Error (dpm/g)	^{137}Cs Activity (dpm/g)	^{137}Cs Error (dpm/g)
0-1	5.37	3.43	0.29	0.00	0.00
1-2	5.75	4.32	0.31	0.15	0.07
2-3	6.03	4.30	0.25	0.30	0.06
3-4	6.49	4.62	0.29	0.23	0.06
4-5	6.11	4.23	0.28	0.36	0.07
5-6	5.82	4.34	0.21	0.22	0.04
6-7	5.12	3.19	0.23	0.16	0.05
7-8	5.68	3.98	0.24	0.18	0.04
8-9	5.77	4.14	0.23	0.34	0.05
9-10	6.22	4.61	0.26	0.31	0.06
10-12	6.66	4.92	0.27	0.24	0.05
12-14	6.39	4.71	0.23	0.23	0.05
14-16	--	--	--	--	--
16-18	6.39	5.14	0.30	0.23	0.05
18-20	5.90	4.57	0.26	0.17	0.04
20-22	--	--	--	--	--
22-24	5.60	3.85	0.22	0.18	0.04
24-26	--	--	--	--	--
26-28	--	--	--	--	--
28-30	5.67	4.07	0.23	0.29	0.05
30-32	5.89	4.22	0.27	0.17	0.05
32-34	5.23	3.48	0.21	0.10	0.04
34-36	5.62	4.25	0.24	0.24	0.05
36-38	5.26	4.15	0.23	0.37	0.05
38-40	5.41	3.78	0.24	0.24	0.04
40-42	5.19	3.37	0.21	0.28	0.05
42-44	--	--	--	--	--
44-46	4.85	3.12	0.19	0.21	0.04

APPENDIX C: GRAIN SIZE AND POROSITY DATA

Core: CP10.12 2

Depth Interval (cm)	Mean (μm)	Median (μm)	Mode (μm)	Standard Deviation (μm)	Porosity
0-1	20.75	11.25	9.37	22.14	0.81
1-2	--	--	--	--	0.79
2-3	19.05	10.09	9.37	22.88	0.83
3-4	17.24	10.62	9.37	16.72	0.79
4-5	18.00	10.40	9.37	19.05	0.80
5-6	23.69	11.93	10.29	29.24	0.82
6-7	14.61	8.75	8.54	16.58	0.84
7-8	14.78	9.04	9.37	16.59	0.85
8-9	15.83	9.16	9.37	18.24	0.83
9-10	25.51	10.40	9.37	38.45	0.83
10-12	24.28	10.71	9.37	33.45	0.82
12-14	16.09	9.07	8.54	18.90	0.82
14-16	14.17	8.48	8.54	16.14	0.83
16-18	16.39	8.60	8.54	20.23	0.84
18-20	16.10	9.07	8.54	18.20	0.82
20-22	12.12	7.47	7.78	13.34	0.85
22-24	13.07	7.79	7.78	15.17	0.84
24-26	13.63	7.95	8.54	15.89	0.81
26-28	17.35	9.00	8.54	21.96	0.84
28-30	13.40	8.38	8.54	14.26	0.84

Core: CP10.12 3

Depth Interval (cm)	Mean (μm)	Median (μm)	Mode (μm)	Standard Deviation (μm)	Porosity
0-1	--	--	--	--	0.86
1-2	21.06	11.56	9.37	22.07	0.82
2-3	19.59	12.08	10.29	18.91	0.80
3-4	14.03	8.54	8.54	15.34	0.85
4-5	12.80	8.70	9.37	12.41	0.84
5-6	15.25	9.24	9.37	16.84	0.83
6-7	19.31	9.16	8.54	26.90	0.83
7-8	14.39	8.30	8.54	16.97	0.83
8-9	14.85	8.36	8.54	18.24	0.84
9-10	17.77	9.67	9.37	20.95	0.84
10-12	18.57	9.38	8.54	22.95	0.84
12-14	20.53	9.74	8.54	25.03	0.83
14-16	20.02	9.28	8.54	25.57	0.83
16-18	24.46	11.23	8.54	28.85	0.82
18-20	30.09	11.30	8.54	37.77	0.83
20-22	32.60	13.15	8.54	40.07	0.82
22-24	24.34	11.15	9.37	31.58	0.84
24-26	19.81	9.25	8.54	25.75	0.82
26-28	31.29	13.69	9.37	37.32	0.80
28-30	31.14	13.68	9.37	38.92	--
30-32	28.29	13.88	9.37	32.37	0.79
32-34	21.48	11.09	9.37	26.00	0.81
34-36	27.73	11.14	9.37	38.86	0.83

Core: CP10.12 4

Depth Interval (cm)	Mean (μm)	Median (μm)	Mode (μm)	Standard Deviation (μm)	Porosity
0-1	--	--	--	--	--
1-2	12.18	8.03	8.54	12.49	0.89
2-3	11.06	7.67	8.54	10.65	0.88
3-4	11.61	7.87	8.54	11.39	0.87
4-5	11.58	7.61	7.78	11.60	0.87
5-6	20.47	9.04	8.54	32.74	0.86
6-7	16.84	9.34	9.37	20.13	0.85
7-8	17.02	9.01	8.54	20.38	0.84
8-9	18.68	9.81	9.37	22.74	0.85
9-10	13.77	8.84	9.37	14.15	0.86
10-12	14.82	9.68	9.37	14.70	0.84
12-14	15.67	9.84	9.37	15.99	0.84
14-16	17.93	11.09	10.29	18.67	0.84
16-18	12.59	8.40	9.37	12.49	0.85
18-20	12.33	8.26	8.54	12.05	0.85
20-22	13.38	9.01	9.37	12.87	0.85
22-24	14.37	9.42	9.37	14.07	0.84
24-26	11.31	7.22	8.54	11.80	0.82
26-28	12.27	8.20	9.37	12.00	0.84
28-30	11.90	7.91	8.54	11.82	0.84
30-32	11.41	7.71	8.54	11.14	0.84
32-34	--	--	--	--	--
34-36	12.99	7.99	8.54	14.01	0.84
36-38	15.84	9.33	9.37	17.71	0.85
38-40	12.33	7.77	8.54	13.01	0.84
40-42	11.44	7.39	7.78	11.76	0.84
42-44	12.15	7.63	8.54	12.77	0.85
44-46	13.86	8.34	8.54	14.89	0.85

Core: CP10.12 5

Depth Interval (cm)	Mean (μm)	Median (μm)	Mode (μm)	Standard Deviation (μm)	Porosity
0-1	--	--	--	--	0.90
1-2	10.91	7.86	8.54	9.93	0.88
2-3	11.61	8.09	8.54	11.16	0.88
3-4	13.65	8.42	8.54	15.48	0.87
4-5	11.48	7.64	8.54	11.78	0.86
5-6	16.15	9.24	9.37	20.25	0.86
6-7	25.77	11.72	10.29	34.69	0.87
7-8	17.40	9.59	9.37	21.48	0.86
8-9	12.60	8.60	9.37	12.77	0.86
9-10	23.41	11.08	10.29	32.03	0.87
10-12	15.39	9.45	9.37	16.96	0.85
12-14	23.22	11.33	9.37	28.77	0.86
14-16	18.08	10.61	10.29	20.68	0.86
16-18	15.83	9.27	9.37	18.71	0.84
18-20	16.91	10.19	10.29	19.14	0.84
20-22	--	--	--	--	--
22-24	15.74	9.00	9.37	19.31	0.84
24-26	19.71	9.30	9.37	28.96	--
26-28	24.68	11.78	9.37	30.18	0.81
28-30	15.16	8.78	9.37	18.36	0.84
30-32	--	--	--	--	--
32-34	24.30	11.62	10.29	32.77	0.83
34-36	13.22	8.73	9.37	13.83	--
36-38	16.31	9.82	9.37	18.54	--
38-40	--	--	--	--	--
40-42	12.51	8.09	8.54	13.74	--
42-44	12.78	8.20	8.54	14.15	--
44-46	13.10	8.38	9.37	14.88	--
46-48	15.19	8.69	8.54	18.63	--
48-50	13.91	8.18	8.54	16.81	--
50-52	14.12	7.90	8.54	18.98	--
52-54	16.82	8.52	8.54	24.31	--

Core: CP10.12 6

Depth Interval (cm)	Mean (μm)	Median (μm)	Mode (μm)	Standard Deviation (μm)	Porosity
0-1	11.02	8.04	8.54	9.69	0.89
1-2	9.34	7.21	8.54	7.66	0.86
2-3	9.62	7.27	8.54	8.16	0.85
3-4	7.95	6.00	7.08	6.78	0.83
4-5	8.70	6.17	7.08	8.18	0.83
5-6	9.71	6.14	7.08	11.00	0.82
6-7	14.50	7.53	7.78	20.65	0.82
7-8	11.61	6.87	7.78	14.01	0.81
8-9	12.38	7.34	7.78	14.67	0.82
9-10	11.15	6.95	7.78	12.56	0.81
10-12	13.15	7.34	7.78	16.39	0.80
12-14	10.39	6.36	7.08	11.72	0.80
14-16	11.36	6.81	7.08	12.88	0.80
16-18	10.89	6.79	7.08	12.08	0.80
18-20	10.73	6.89	7.78	11.59	0.80
20-22	11.36	7.20	7.78	12.37	0.81
22-24	11.42	7.48	8.54	11.79	0.81
24-26	13.43	7.95	8.54	15.73	0.80
26-28	11.95	7.52	8.54	13.05	0.81
28-30	10.25	6.52	7.08	11.30	0.80
30-32	11.01	6.72	7.08	12.53	0.80

Core: CP10.12 7

Depth Interval (cm)	Mean (μm)	Median (μm)	Mode (μm)	Standard Deviation (μm)	Porosity
0-1	11.13	7.50	8.54	10.82	0.85
1-2	11.01	7.72	8.54	10.00	0.85
2-3	10.75	7.82	8.54	9.46	0.83
3-4	9.89	7.10	8.54	8.97	0.83
4-5	10.50	7.47	8.54	9.54	0.82
5-6	13.91	8.09	8.54	16.99	0.80
6-7	11.95	7.79	8.54	12.55	0.81
7-8	13.17	8.48	9.37	14.08	0.83
8-9	13.16	9.01	9.37	12.77	0.81
9-10	12.19	8.12	8.54	12.27	0.78
10-12	11.16	6.95	7.78	12.52	0.79
12-14	10.42	6.63	7.08	11.26	--
14-16	11.47	7.00	7.78	13.03	--
16-18	10.83	6.30	7.08	13.36	0.79
18-20	12.44	7.04	7.78	15.50	0.80
20-22	14.34	7.77	7.78	17.82	--
22-24	12.27	7.34	7.78	14.68	0.82
24-26	11.82	7.66	8.54	12.79	0.82
26-28	11.89	7.80	8.54	12.40	0.81
28-30	14.05	9.23	9.37	14.51	0.82
30-32	13.14	8.09	8.54	14.73	--
32-34	11.31	7.74	8.54	11.02	0.81
34-36	13.50	7.30	7.78	19.52	--
36-38	12.29	7.48	7.78	14.53	0.81

Core: CP10.12 8

Depth Interval (cm)	Mean (μm)	Median (μm)	Mode (μm)	Standard Deviation (μm)	Porosity
0-1	11.90	8.46	9.37	10.70	0.88
1-2	13.04	9.11	9.37	11.94	0.87
2-3	12.35	8.76	9.37	11.10	0.84
3-4	12.45	8.96	9.37	10.94	0.84
4-5	11.14	8.22	9.37	9.56	0.84
5-6	13.71	8.94	9.37	13.83	0.82
6-7	11.62	8.44	9.37	10.16	0.82
7-8	11.65	8.41	9.37	10.39	0.84
8-9	11.86	8.40	9.37	10.78	0.84
9-10	12.23	8.60	9.37	11.16	0.83
10-12	13.40	9.53	10.29	11.85	0.82
12-14	13.21	9.18	9.37	12.08	0.81
14-16	13.12	9.04	9.37	12.15	0.80
16-18	13.70	9.19	9.37	12.98	0.80
18-20	16.47	9.99	9.37	17.83	0.78
20-22	18.27	10.45	9.37	20.39	0.80
22-24	15.48	9.91	10.29	16.35	0.83
24-26	14.92	9.76	10.29	14.93	0.83
26-28	15.95	9.78	9.37	17.14	0.81
28-30	17.86	9.99	9.37	20.47	0.79
30-32	12.60	8.13	8.54	12.87	0.82
32-34	10.56	7.30	8.54	9.98	0.81
34-36	11.61	7.84	8.54	11.15	0.81
36-38	10.76	7.68	8.54	9.80	0.80
38-40	11.15	7.15	7.78	11.28	0.79
40-42	13.34	8.62	9.37	13.38	0.79

Core: CP10.12 9

Depth Interval (cm)	Mean (μm)	Median (μm)	Mode (μm)	Standard Deviation (μm)	Porosity
0-1	13.01	9.29	9.37	11.35	0.89
1-2	13.74	9.55	9.37	12.45	0.87
2-3	12.60	8.93	9.37	11.18	0.85
3-4	13.24	9.12	9.37	12.12	0.84
4-5	12.58	9.00	9.37	10.97	0.83
5-6	18.95	11.63	10.29	19.58	0.79
6-7	18.81	11.60	10.29	20.50	0.77
7-8	18.93	10.51	9.37	21.99	0.79
8-9	15.51	9.09	9.37	17.62	0.82
9-10	13.30	8.45	8.54	14.10	0.82
10-12	16.89	10.20	9.37	18.43	0.81
12-14	18.65	10.20	9.37	22.55	0.80
14-16	17.48	10.93	10.29	18.03	0.78
16-18	14.61	9.18	9.37	15.27	0.80
18-20	14.94	8.95	9.37	17.03	0.81
20-22	13.24	8.49	9.37	14.23	0.82
22-24	13.14	8.64	9.37	13.29	0.82
24-26	13.60	9.07	9.37	13.86	0.81
26-28	--	--	--	--	--
28-30	--	--	--	--	--
30-32	12.05	7.90	8.54	12.43	0.81
32-34	11.15	7.56	8.54	11.11	0.79
34-36	11.79	7.16	7.78	13.84	0.78
36-38	13.71	7.73	8.54	17.64	0.78
38-40	24.12	9.38	8.54	38.49	0.79
40-42	23.01	12.32	8.54	25.24	0.73
42-44	--	--	--	--	--
44-46	16.72	9.73	9.37	17.93	0.71

Core: CP8.14 2

Depth Interval (cm)	Mean (μm)	Median (μm)	Mode (μm)	Standard Deviation (μm)	Porosity
0-1	0.50	29.70	13.49	33.31	0.83
1-2	1.50	24.03	10.92	27.82	0.84
2-3	2.50	23.28	10.28	29.84	0.86
3-4	3.50	14.81	8.53	17.43	0.86
4-5	4.50	20.18	9.75	26.36	0.85
5-6	5.50	20.30	9.88	26.29	0.84
6-7	6.50	14.63	8.51	17.24	0.83
7-8	7.50	21.11	9.70	29.52	0.84
8-9	8.50	15.26	8.14	20.06	0.85
9-10	9.50	13.88	8.71	16.67	0.85
10-12	11.00	14.50	8.71	18.57	0.84
12-14	13.00	13.25	8.38	16.70	0.85
14-16	15.00	16.06	8.88	21.32	0.83
16-18	17.00	20.07	9.07	26.41	0.82
18-20	19.00	23.75	9.39	31.35	0.80
20-22	21.00	17.69	7.72	27.17	0.82
22-24	23.00	10.55	6.47	13.58	0.83
24-26	25.00	22.05	9.19	30.31	0.81
26-28	27.00	15.45	7.87	21.50	0.82
28-30	29.00	13.24	7.08	18.02	0.82
30-32	31.00	11.81	6.83	15.36	0.82
32-34	33.00	11.72	6.89	15.39	0.83
34-36	35.00	13.66	7.57	17.97	0.89
36-38	37.00	15.02	7.70	20.68	0.81
38-40	39.00	18.05	8.01	24.47	0.79
40-42	41.00	16.80	8.62	20.65	0.81

Core: CP8.14 3

Depth Interval (cm)	Mean (μm)	Median (μm)	Mode (μm)	Standard Deviation (μm)	Porosity
0-1	34.16	12.93	8.54	41.55	0.87
1-2	30.84	12.89	8.54	36.20	0.85
2-3	18.37	9.04	8.54	24.04	0.86
3-4	18.67	9.61	9.37	23.52	0.85
4-5	18.70	10.07	9.37	22.23	0.85
5-6	16.88	9.04	9.37	21.54	0.86
6-7	19.16	9.84	9.37	24.82	0.86
7-8	14.49	7.97	8.54	19.02	0.87
8-9	17.74	9.75	10.29	22.63	0.86
9-10	13.86	8.26	9.37		--
10-12	17.20	9.83	10.29	20.47	0.85
12-14	15.49	8.88	9.37	20.14	--
14-16	13.68	8.38	9.37	17.09	0.85
16-18	10.12	7.20	8.54	10.08	0.84
18-20	13.75	7.61	8.54	18.00	0.84
20-22	17.17	8.77	8.54	22.22	0.83
22-24	15.70	8.85	9.37	19.76	0.83
24-26	16.80	8.53	9.37	22.66	0.82
26-28	19.69	9.69	9.37	26.02	0.82
28-30	15.61	8.75	9.37	19.08	0.82
30-32	21.50	9.14	8.54	30.26	0.82
32-34	27.51	11.23	9.37	35.87	--
34-36	25.58	11.28	9.37	31.67	0.80
36-38	32.56	15.86		37.78	0.81
38-40	16.47	8.20	8.54	22.75	0.81
40-42	15.49	8.88	9.37	20.14	--

Core: CP8.14 4

Depth Interval (cm)	Mean (μm)	Median (μm)	Mode (μm)	Standard Deviation (μm)	Porosity
0-1	25.92	10.32	9.37	35.98	0.90
1-2	22.59	10.09	9.37	29.90	0.89
2-3	19.30	9.93	9.37	24.32	0.88
3-4	22.68	9.85	8.54	29.67	0.87
4-5	28.61	10.61	8.54	38.57	0.87
5-6	21.29	8.91	8.54	29.39	0.86
6-7	31.00	10.13	8.54	44.27	0.86
7-8	24.73	10.42	8.54	32.63	0.85
8-9	22.74	9.98	8.54	29.39	0.86
9-10	--	--	--	--	0.84
10-12	21.91	10.15	9.37	29.37	0.84
12-14	13.32	7.36	8.54	19.40	0.84
14-16	17.12	8.16	8.54	25.50	0.84
16-18	12.73	7.94	9.37	17.05	0.84
18-20	14.93	7.94	8.54	21.17	0.84
20-22	17.31	9.81	10.29	22.66	0.84
22-24	13.01	7.58	8.54	17.01	0.83
24-26	18.40	9.18	9.37	25.08	0.84
26-28	14.26	7.95	8.54	19.48	0.84
28-30	17.11	8.44	8.54	23.22	0.82
30-32	20.70	9.40	8.54	28.18	0.83
32-34	15.21	8.44	9.37	20.09	0.85
34-36	19.55	9.28	9.37	27.37	--
36-38	23.91	11.32	10.29	32.06	0.81
38-40	18.73	9.47	9.37	24.66	0.84
40-42	15.55	8.51	9.37	20.11	0.83
42-44	14.92	8.17	9.37	21.47	0.85

Core: CP8.14 5

Depth Interval (cm)	Mean (μm)	Median (μm)	Mode (μm)	Standard Deviation (μm)	Porosity
0-1	--	--	--	0.9	0.9
1-2	13.91	8.8059	9.371	0.87	0.87
2-3	12.58	8.1957	9.371	0.87	0.87
3-4	16.21	9.4496	10.29	0.86	0.86
4-5	19.76	10.2977	10.29		
5-6	16.05	9.7368	10.29	0.85	0.85
6-7	13.21	8.4787	9.371	0.86	0.86
7-8	9.062	7.1623	8.537	0.86	0.86
8-9				0.85	0.85
9-10	14.94	8.4697	9.371	0.85	0.85
10-12	13.17	8.4765	9.371	0.86	0.86
12-14	--	--	--	--	--
14-16	15.49	8.8314	9.371	0.87	0.87
16-18	11.84	8.2362	9.371	0.86	0.86
18-20	11.81	8.3441	9.371	0.86	0.86
20-22	9.036	6.5038	7.777	0.87	0.87
22-24	10.03	7.9027	9.371	0.87	0.87
24-26	12.9	9.0378	10.29	0.87	0.87
26-28	15.51	9.1601	10.29	0.87	0.87
28-30	13.23	8.523	9.371	0.86	0.86
30-32	9.739	7.0396	8.537	0.86	0.86
32-34	11.15	7.4132	8.537	0.85	0.85
34-36	14.54	8.5725	9.371	0.86	--
36-38	9.475	7.1214	8.537	0.84	0.84
38-40	8.741	6.1856	7.777	0.83	0.83
40-42	15.16	8.6013	9.371	0.82	0.82

Core: CP8.14 6

Depth Interval (cm)	Mean (μm)	Median (μm)	Mode (μm)	Standard Deviation (μm)	Porosity
0-1	8.05	6.45	7.78	6.34	0.88
1-2	11.29	7.59	8.54	13.64	0.86
2-3	14.81	8.28	8.54	21.25	0.85
3-4	10.80	8.32	9.37	9.00	0.86
4-5	12.42	7.06	7.78	18.38	0.86
5-6	12.80	8.07	8.54	15.01	0.84
6-7	14.05	8.25	8.54	18.22	0.84
7-8	13.30	8.32	8.54	15.44	0.84
8-9	12.37	7.90	8.54	14.85	0.84
9-10	11.02	7.56	8.54	12.77	0.83
10-12	9.48	6.98	8.54	10.04	0.85
12-14	11.16	7.54	8.54	12.21	0.83
14-16	8.29	6.62	7.78	6.59	0.83
16-18	8.49	5.68	6.45	9.50	0.82
18-20	12.76	8.33	9.37	15.30	0.83
20-22	11.14	7.90	9.37	10.96	0.82
22-24	8.03	6.37	7.78	6.42	--
24-26	11.28	7.23	8.54	13.33	0.81
26-28	19.52	7.33	7.78	34.41	0.81
28-30	11.36	7.47	8.54	13.06	0.81
30-32	16.09	9.47	10.29	19.44	0.81
32-34	12.88	8.47	9.37	14.94	0.81
34-36	21.02	8.94	9.37	34.28	0.81
36-38	15.10	9.11	9.37	17.70	0.80
38-40	12.04	8.25	9.37	12.46	0.81
40-42	13.52	9.04	10.29	15.83	0.81
42-44	12.40	7.75	8.54	15.32	0.80

Core: CP8.14 7

Depth Interval (cm)	Mean (μm)	Median (μm)	Mode (μm)	Standard Deviation (μm)	Porosity
0-1	10.28	7.08	8.54	11.05	0.83
1-2	10.86	6.71	7.78	13.78	0.84
2-3	9.80	6.37	7.08	11.55	0.81
3-4	10.09	6.27	7.08	12.62	0.8
4-5	10.34	6.35	7.08	13.13	0.8
5-6	11.55	6.51	7.08	16.15	0.79
6-7	9.61	6.28	7.08	11.16	0.79
7-8	9.05	6.41	7.78	8.75	0.79
8-9	10.67	6.88	7.78	13.03	0.78
9-10	10.92	7.05	7.78	13.06	0.8
10-12	10.91	7.27	8.54	12.55	
12-14	11.48	8.16	9.37	11.75	0.8
14-16	11.23	7.43	8.54	12.65	0.8
16-18	17.80	8.68	8.54	24.18	0.79
18-20	9.59	5.95	7.08	12.14	0.76
20-22	7.03	5.31	6.45	6.08	0.76
22-24	8.83	5.92	7.08	10.29	0.76
24-26	8.78	5.75	7.08	10.44	0.76
26-28	9.10	5.41	6.45	12.06	0.76
28-30	8.23	5.29	6.45	9.97	0.76
30-32	12.01	7.31	8.54	15.29	0.79
32-34	10.58	7.33	8.54	11.20	0.78
34-36	11.12	7.44	8.54	12.44	0.77
36-38	9.33	5.74	7.08	11.59	0.76

Core: CP8.14 8

Depth Interval (cm)	Mean (μm)	Median (μm)	Mode (μm)	Standard Deviation (μm)	Porosity
0-1	15.18	9.26	9.37	17.46	0.89
1-2	12.03	9.09	10.29	10.23	0.88
2-3	17.10	9.77	9.37	20.71	0.87
3-4	15.04	8.72	9.37	18.89	0.87
4-5	13.41	8.61	9.37	14.77	0.86
5-6	17.16	9.17	9.37	23.03	0.84
6-7	16.39	9.28	9.37	20.98	0.85
7-8	15.28	8.29	8.54	20.40	0.83
8-9	16.02	8.53	9.37	22.32	0.82
9-10	16.84	8.75	9.37	23.62	0.85
10-12	--	--	--	--	0.83
12-14	16.44	8.45	8.54	22.90	0.92
14-16	14.05	8.09	8.54	17.35	0.8
16-18	15.77	8.31	8.54	21.60	0.8
18-20	15.73	8.03	8.54	20.73	0.79
20-22	22.10	9.43	8.54	28.73	0.79
22-24	14.73	8.13	8.54	18.83	0.81
24-26	21.46	8.61	8.54	31.39	0.78
26-28	17.57	9.35	9.37	21.97	0.8
28-30	15.28	8.96	9.37	18.27	0.8
30-32	14.20	9.28	10.29	15.71	0.8
32-34	13.61	8.28	9.37	16.21	0.81
34-36	12.76	8.47	9.37	13.84	0.79
36-38	17.08	9.27	9.37	22.56	0.78
38-40	20.62	9.75	9.37	28.08	0.8
40-42	--	--	--	--	--
42-44	17.76	9.86	10.29	22.57	0.82

APPENDIX D: MATLAB CODE

```
%%%%%%%%%%%%%%%%%%%%%%%%%%%%%%%%%%%%%%%%%%%%%%%%%%%%%%%%%%%%%%%%%%%%%%%%%%%%%%%
%Henkel.m
%
% This script solves for the amplitude of sinusoidal pressure change
% delta_p using the relation described in Henkel, 1970: The Role of Waves
% in Causing Submarine Landslides.
%
% Input Parameters
% L Wavelength (m)
% d Wave height (m)
% k     Cu/Gamma'z
% Gamma Density (g/ml)
% z Water Depth (m)
% y Longitude (m)
% HL    Half Length - Henkel's variable x (m)
% The inputs Y,Z are taken as three columns in the array "data()"
%
% Calculated Parameters
% Beta  Slope Angle
% A     sin(alpha)-(alpha)cos(alpha)
% B     sin(theta)-(theta)cos(theta)/sin^3(theta)
%
% Output Parameters
% P Amplitude of Sinusoidal Pressure Change
%%%%%%%%%%%%%%%%%%%%%%%%%%%%%%%%%%%%%%%%%%%%%%%%%%%%%%%%%%%%%%%%%%%%%%%%%%%%%%%

%% Define Constant Values
k=0.05;
gamma=1;
wave_period = 8; %Seconds - Typical of shelf...
deepwater_wave_height = 1.5; % Meters
H0=1.5;

%% Import YZ data from .csv file
% Calculate slope angle 'Beta' (rate of change of Y relative to Z)
data = importdata('XYZ_for_Henkle.txt');
data = data.data;
y = data(:,2);
z = data(:,3);

%% Calculate Wavelength
% Run wavelength function to calculate L for a given depth
L = zeros(size(z));
for i = 1:size(z)
    [l,e,c] = wavelength(wave_period, z(i), 0, 0, 0);
    L(i) = l;
end

%% Calculate Waveheight
% Run waveheight function to calculate d for a given depth z and wavelength
d = zeros(size(z));
for i = 1:size(z)
    d(i) = w_height(L(i), z(i), deepwater_wave_height);
end


%% Define x
% Half-length for calculations
```

```
x = L / 2;

%% Calculate Theta
% Unfortunately, Henkel defines things in such a way that it's very
% difficult to calculate "theta" from the equations given.  It's much
% easier to use an alternate formulation calculated from the fact that
% "theta", "x", and "d" describe a circular segment.
% See http://en.wikipedia.org/wiki/Circular_segment (Note that "d"
% here is Henkel's d. It's equivalent to "h" in the wikipedia article.)
beta = abs(gradient(z) ./ gradient(y));
d = beta .* x;
d(isnan(d)) = 0;

% Finishing theta calculation based on circular segment
r = d / 2 + L.^2 ./ (8 * d);
theta = 2 .* asin(L ./ (2 * r));

%% Calculate pressure difference required for failure
% Calculate alpha for values of z for which we have HL and L
alpha = (2*pi*x) ./ L;

% Calculate A & B
A=sin(alpha) - (alpha .* cos(alpha));
B=(sin(theta) - theta .* cos(theta) ) ./ sin(theta).^3;

% Finally, let's calculate the pressure differential
delta_p = (k * gamma * L * 4 * pi^2) .* (x ./ L).^3 ...
          .* (B - beta / (3 * k)) ./ A;

%% Calculate x/L
 xL=zeros(size(z));
for i= 1:size(z)
    xL(i)=z(i) ./ L(i);
end

%% Calculate delta_p / k gamma'L
yy = zeros(size(z));
for i = 1:size(z)
    yy = delta_p(i) ./ (k*gamma*L);
end


%%%%%%%%%%%%%%%%%%%%%%%%%%%%%%%%%%%%%%%%%%%%%%%%%%%%%%%%%%%%%%%%%%%%%%%%%%%%%%%
% SeedRahman.%
% This script solves for the amplitude of
% sinusoidal pressure change using the relation of Seed and Rahman (1978)
%
%% Input Parameters
%
% L         Wavelength (m)
% dbs       Depth below seabed (m)
% H         Wave height
% Gammaw    Unit weight of water, 9180 N/m^3
% Gamma     Unit weight of sediment
% T         Wave Period, (seconds)
% z         Water Depth, (m)
% U         Current Velocity, (m/s)
% g         Gravity (9.8 m/s^2)
% delta     Direction of current (rad) with respect to the cross-shore
```

```
%           direction
% alpha     Direction of waves (rad) with respect to the cross-shore
%           direction
% tol       Maximum tolerance allowed for L the default is 1e-6
% The inputs Y,Z are taken as three columns in the array "data()"
%
% Output Parameters
% Shear     Cyclic Shear Stress/Vertical Effective Stress
%%%%%%%%%%%%%%%%%%%%%%%%%%%%%%%%%%%%%%%%%%%%%%%%%%%%%%%%%%%%%%%%%%%%%%%%%%%%%%%

%% Define Constant Values
gamma_w=9.807;
gamma=10.000; % after Henkle 40lb/sq ft
T=6;
U=0.1;
delta=90*pi/180; %radian
alpha=10*pi/180; %radians
tol=1e-6;
dbs=0.25;
wave_period=6;
deepwater_wave_height=1.5;
g = 9.81;
H0 = 1.5;

%% Import YZ data from .csv file
% Calculate slope angle 'Beta' (rate of change of Y relative to Z)
% 1st derivative delta_y / delta_z
data = importdata('XYZ_for_Henkle.txt');
data = data.data;
y = data(:,2);
z = data(:,3);

%% Calculate Wavelength
% Run wavelength function to calculate L for a given depth
L = zeros(size(z));
for i = 1:size(z)
    [l,e,c] = wavelength(wave_period, z(i), 0, 0, 0);
    L(i) = l;
end



%% Calculate Waveheight
% Run waveheight function to calculate d for a given depth z and wavelength
H = zeros(size(z));
for i = 1:size(z)
    H(i) = w_height(L(i), z(i), H0);
end

%% Calculate Peak cyclic shear stress
fz = zeros(size(z));
for i = 1:size(z)
    fz(i)=(exp((-2 .* pi .* z(i)) ./ L(i)));
end

fd = zeros(size(z));
for i = 1:size(z)
    fd(i) = (0.5.*(1/cosh((2 * pi .* z(i))./ L(i))));
end
```

```
shear3= zeros(size(z));
for i=1:size(z)
    shear3(i)= (2 * pi * (gamma_w / gamma));
end

shear=zeros(size(z));
for i=1:size(z)
    shear(i)= fz(i) .* fd(i) .* shear3(i).* ((H(i) ./ L(i)));
end

%% Incorporate Vertical Effective Stress
beta=load('beta.txt');

angle=zeros(size(z));
for i=1:size(z)
    angle(i)= cos(beta(i)).^2;
end

waterdepth=zeros(size(z));
for i=1:size(z)
    waterdepth(i)= z(i) .* gamma_w;
end

vertstress=zeros(size(z));
for i=1:size(z)
    vertstress(i)= 1 * (g) .* angle(i) .* (gamma - gamma_w) .*
waterdepth(i) * 0.55;
end

verteffstress=zeros(size(z));
for i=1:size(z)
    verteffstress(i)= vertstress(i)-2;
end

%% Ratio of shear stress to vertical effective stress
ratio=zeros(size(z));
for i=1: size(z)
    ratio(i)= shear(i) ./ (vertstress(i) - 2);
end


%% Critical Shear Stress
critshear=zeros(size(z));
for i=1:size(z)
    critshear(i)=shear(i) .* verteffstress(i);
end


%%%%%%%%%%%%%%%%%%%%%%%%%%%%%%%%%%%%%%%%%%%%%%%%%%%%%%%%%%%%%%%%%%%%%%%%%%%%%%%
% function [L,e,c] = wavelength(T,d,alpha,U,delta,tol)
% Solves the dispersion relation for ocean surface waves
%
% USAGE:
%   [L,e,c] = wavelength(T,d,U,delta,alpha,tol)
%
% DESCRIPTION:
%   Simple program that solves the
%   dispersion relation for ocean
%   surface waves using the
```

```
%   Newton-Raphson method
%   It can also account for wave-current
%   interaction by solving a modified form
%   of the dispersion relation proposed be
%   Jonsson (1970)
%
% INPUT VARIABLES:
%   T = Wave Period, (seconds)
%   d = Water Depth, (m)
%   U = Current Velocity, (m/s)
%   delta = direction of current (rad) with
%       respect to the cross-shore direction
%   alpha = direction of waves (rad) with
%       respect to the cross-shore direction
%   tol = Maximum tolerance allowed for L
%       the default is 1e-6 (Generally 3 iterations)
%
% OUTPUT VARIABLES:
%   L = Wave length, (m)
%   e = Relative error of L
%   c = Iteratios
%
% NOTES:
%   For deep water - L = g*T^2/2/pi
%   For shallow water - L = T*sqrt(gd)
%
% REFERENCES
% Eckart, C. (1952) The Propagation of Gravity
%   Waves From Deep to Shallow Water, Natl. Bur. Standards,
%   Circular 521, Washington, DC, pp 165-173.
%
% Jonsson, I.G., Skougaard, C., and Wang, J.D. (1970)
%   Interaction between waves and currents, Preceedings
%   of the 12th Coastal Engineering Conference,
%   ASCE, 489-507
%
% nargin==0 runs a demo
%
%%%%%%%%%%%%%%%%%%%%%%%%%%%%%%%%%%%%%%%%%%%%%%%%%%%%%%%%%%%%%%%%%%%%%%%%%%%%%%%

g = 9.81; %gravity
if nargin==0
    T = res(7);
    d = 0:0.01:10;
    U = 0.5; %m/s
    delta = 90*pi/180; %rad
    alpha = 10*pi/180; %rad
end
if nargin<5
    delta = 0.5*pi; %90 deg
end
if nargin<6
    tol = 1e-6;
end
%This is useful only in some cases
% if any(size(T)~=size(d))
%     if nargin==2
%         [T,d] = meshgrid(T,d);
%     else
%         [T,d,alpha,U,delta] = ndgrid(T,d,alpha,U,delta);
%     end
```

```
% end
Lo = g*T.^2./2./pi; %deep water wave length
%First approximation is made with the
%eq. given by Eckart (1952) which gives ~10% error
L = Lo.*sqrt(tanh(4*pi.^2.*d./T.^2./g));
e = L; %Initialize error
c = 0; %counter
%Newton-Raphson method
if nargin==2
    while any(e>tol)
        c = c + 1;
        k = 2*pi./L;
        a = Lo.*tanh(k.*d) - L;
        b = -2*Lo.*(1-tanh(k.*d).^2)*pi./L.^2.*d-1;
        L2 = L - a./b;
        e = abs(L2-L);
        L = L2;
    end
else
    while any(e>tol)
        c = c + 1;
        k = 2*pi./L;
        a = Lo.*tanh(k.*d)./sqrt(1-U.*cos(delta-alpha).*T./L) - L;
        b = -1/2*(-4*Lo.*pi.*d.*L+4*Lo.*pi.*d.*U.*cos(delta-alpha).*T ...
            -Lo.*sinh(k.*d).*U.*cos(delta-alpha).*T.*L.*cosh(k.*d) ...
            -2*L.^3.*(-(-L+U.*cos(delta-
alpha).*T)./L).^(1/2).*cosh(k.*d).^2 ...
            +2*L.^2.*(-(-L+U.*cos(delta-
alpha).*T)./L).^(1/2).*cosh(k.*d).^2 ...
            .*U.*cos(delta-alpha).*T)./(-L+U.*cos(delta-alpha).*T)./L.^2
...
            ./(-(-L+U.*cos(delta-alpha).*T)./L).^(1/2)./cosh(k.*d).^2;
        L2 = L - a/b;
        e = abs(L2-L);
        L = L2;
    end
end


%%%%%%%%%%%%%%%%%%%%%%%%%%%%%%%%%%%%%%%%%%%%%%%%%%%%%%%%%%%%%%%%%%%%%%%%%%%%
%function [H] = w_height( T,d,H0 )
%   Calculates wave height based on period, water depth, and deep water
%   wave height, using dispersion relationship for wavelenght in function
%  "wavelength"
%%%%%%%%%%%%%%%%%%%%%%%%%%%%%%%%%%%%%%%%%%%%%%%%%%%%%%%%%%%%%%%%%%%%%%%%%%%%

cd=9.81*T/(2*pi);%deep water phase velocity, p. 153 in Kinsman
cgd=cd/2; %deep water group velocity, p. 153 in Kinsman
L=wavelength(T,d);
c=L/T;
k=2*pi./L;
cg=(c/2).*(1+((2.*k.*d)./sinh(2.*k.*d))); %intermediate water group
velocity, 3.4:22.2 in Kinsman, p. 153
H=H0.*(cgd./cg).^.5; %intermediate water wave height for refraction
coefficient=1, 3.5:1.3 in Kinsman p. 153

end
```

APPENDIX E: QXRD DATA

Sample Name	Mineral (%)					Clay Fraction (%)	
	Quartz	Plagioclase	Pyrite	Siderite	Clay	Illite	Chlorite
BIC 1300.1	53.25	12.94	0.76	--	33.05	5.24	93.55
BIC 1302	49.63	5.28	2.26	--	42.83	10.72	88.31
BIC 1304	14.56	--	0.93	68.62	15.89	30.33	65.56
BIC 1307	53.69	7.18	1.60	--	37.53	17.10	80.86
BIC 1308	46.00	6.66	4.93	--	42.40	51.10	47.03
BIC 1315	44.71	5.83	0.65	--	48.81	32.45	64.37
BIC1322.5	33.77	2.87	--	--	63.36	--	--
BIC 1323	49.95	7.11	0.23	--	42.71	31.89	66.28
BIC 1324	36.92	5.30	--	--	57.78	31.17	67.01
BIC 1327	32.22	4.08	--	--	63.71	32.23	66.41

VITA

Kathryn Christine Denommee was born in Calgary, Alberta and was raised in Ottawa, Ontario. After completing high school in 2003, she enrolled at the University of Waterloo in Waterloo, Ontario, where she earned an Honours Bachelor of Science in Earth Science, hydrogeology specialization (co-operative program). Kathryn was employed by Conestoga Rovers and Associates as a hydrogeologist in Waterloo, Ontario before moving to St. John's, Newfoundland in September of 2008 to pursue her Master of Science degree in Geology at Memorial University of Newfoundland. Here, under the supervision of Dr. Sam Bentley, she developed the most complete record of hurricane landfall frequency in the Caribbean Basin to date. Kathryn joined Dr. Bentley when he moved to LSU in 2011 to complete her PhD. While at LSU Kathryn interned for both the ExxonMobil Exploration Company and the ExxonMobil Upstream Research Company and upon completion of her PhD program will join the ExxonMobil Upstream Research Company in Houston, Texas as a research geoscientist in the reservoir quality prediction group.